UNIVERSITÀ DEGLI STUDI DI PADOVA

UNIVERSITÀ DEGLI STUDI DI PADOVA

INSTITUTO SUPERIOR TECNICO-UNIVERSIDADE TECNICA DE LISBOA

Centro Interdipartimentale *"Centro Ricerche Fusione"* Università di Padova

JOINT RESEARCH DOCTORATE IN FUSION SCIENCE AND ENGINEERING

Performance limiting MHD phenomena in fusion devices: physics and active control

Coordinator: Chiar.mo Prof. Piero Martin

Supervisors: Prof. Leonardo Giudicotti

Dr. Tommaso Bolzonella

Doctoral Student: Matteo Baruzzo

Padova, 31 Gennaio 2011

Abstract

In this thesis different aspects of MagnetoHydroDynamic phenomena that limit plasma performance and confinement in toroidal pinch devices will be addressed. The thesis contains original work carried out in two different devices: the Joint European Torus (JET) tokamak, and the RFX-mod Reversed Field Pinch (RFP), which are both the largest magnetic confinement devices in operation for their configuration.
In the JET device focus was put on Neoclassical Tearing Modes (NTMs), which are resistive instabilities that tear magnetic field lines and reconnect them forming magnetic field islands. With the aim of studying the NTM physics, two radial localization techniques for magnetic islands have been developed, and their outputs have been compared with q profiles obtained with a Motional Stark Effect diagnostic. One of the studied localization techniques has been also used in a non conventional way to reconstruct the NTM m number spectrum, and to extract new information on the tearing-kink structure of the mode. The impact of NTMs on JET advanced tokamak discharges has been documented, with the ultimate aim of quantifying the loss in plasma confinement induced by the mode as a function of the island radial localization.
Other chirping modes were encountered in JET, which are thought to be driven by energetic particles and dubbed q=2 fishbones. Their experimental signature and impact on the plasma discharge have been studied.
In the RFX-mod device the addressed topic was the study and control of Resistive Wall Modes (RWMs) in RFP configuration. The RWM is a branch of the ideal kink mode that grows on the time scale of current diffusion in the wall.
First of all a RWM growth rate database in RFX-mod was created, and it was subsequently used as a standard growth rate reference in the analysis of the couplings between different m and n harmonics.
Advanced feedback control topics were addressed as well, such as the development and benchmark of a dynamical RWM control simulator, and the RWM stabilization in control experiments using various sets of active saddle coils.

Prefazione

In questa tesi saranno affrontati i diversi aspetti dei fenomeni magnetoidrodinamici che limitano le prestazioni ed il confinamento degli esperimenti toroidali di tipo pinch.
La tesi contiene il lavoro originale portato avanti in due diverse macchine, che sono entrambe i più grandi esperimenti a confinamento magnetico in operazione per rispettive configurazioni: il tokamak Joint European Torus (JET) ed il Reversed Field Pinch (RFP) RFX-mod.
Nel tokamak JET l'attività di ricerca si è concentrata sui Neoclassical Tearing Modes (NTM), che sono delle instabilità resistive che rompono le linee di campo magnetico e le riconnettono, formando delle isole di campo magnetico. Allo scopo di studiare la fisica dei NTM, sono state sviluppate due tecniche per la localizzazione radiale delle isole magnetiche, ed i risultati prodotti sono stati confrontati con i profili radiali di q ottenuti per mezzo della diagnostica Motional Stark Effect. Una delle tecniche di localizzazione studiate è stata anche usata in modo non convenzionale per ricostruire lo spettro del numero d'onda m poloidale dei NTM, e per ricavare informazioni sulla struttura kink-tearing di queste instabilità. E' stato pure documentato l'impatto dei NTM sulle scariche advanced tokamak, allo scopo di quantificare il peggioramento nel confinamento del plasma che queste inducono, in funzione della localizzazione radiale dell'isola magnetica da loro generata.
Durante l'attività su JET sono state incontrate anche delle altre instabilità, che si ritiene siano eccitate dalla popolazione di particelle veloci nel plasma, e che sono soprannominate fishbone $q = 2$. Sono state caratterizzate le loro evidenze sperimentali ed il loro impatto sugli impulsi di plasma.
Nel RFP RFX-mod il lavoro è stato concentrato sullo studio e controllo dei Resistive Wall Modes (RWM), che sono una branca dei modi kink ideali che cresce selle scale dei tempi della diffusione delle correnti all'interno delle strutture conduttrici attorno al plasma.
Inizialmente è stato creato un database contenente i tassi di crescita di tutte le instabilità di tipo RWM rilevate in RFX-mod, ed il database è stato in seguito usato come riferimento nell'analizzare gli accoppiamenti tra le diverse armoniche m ed n dei RWM.
Sono stati affrontati anche problemi di controllo in feedback avanzato, come lo sviluppo ed il benchmark di un simulatore dinamico del controllo attivo RWM, e la sperimentazione del controllo RWM usando diversi gruppi di bobine attive.

Contents

CHAPTER 1

Introduction

Nuclear Fusion in magnetically confined plasmas is not only a chance to study interesting complex systems and a challenging issue in the fields of electrical, mechanical and materials engineering, but it is above all a key to obtain a viable and clean energy source for the future.
The study of Magnetohydrodynamic instabilities and the development and test of techniques for their control, is involved in all of the three issues previously listed, beginning from the last one: the confined plasma, plus the three-dimensional conducting structures and the active magnetic coils, that are often part of modern fusion experiments, compose a complex system whose equilibria must be robustly stable against any sort of macroscopic perturbation. This is a necessary condition for the operation of a fusion device as a reliable source of energy.
The stability problem involves different interlinked areas: the physics of plasma modes, meaning their driving energy sources and physical mechanisms that can stabilize them, but also the response of eddy currents that develop in the vacuum vessel of the device reacting to the instability growth, and the magnetic fields produced by plasma active control systems.
The *fil rouge* that links the different parts of this thesis is the fact that all of the studied instabilities have a dangerous effect on the plasma performance, and must be understood and avoided or controlled. In the avoidance and control process the different aspects previously mentioned come into play, along with the importance of considering all of these effects as interlinked and non separable in their three-dimensional details.
The thesis is meant to give a summary of the work carried out during the PhD to a reader who has already a general knowledge in the field of magnetic confinement, but has not to be a specialist of the MagnetoHydroDynamic (MHD) field. It will therefore begin with an introduction to the MHD framework, and with a summary of theoretical and experimental background of the encountered phenomena, which will be given in Chapter 2.
In the following chapters the scientific work, that has been carried out in almost equal part in two different devices, will be presented:
the first device is the Joint European Torus (JET), which is the largest operating tokamak in the world, capable of a plasma current up to 4.5MA in divertor con-

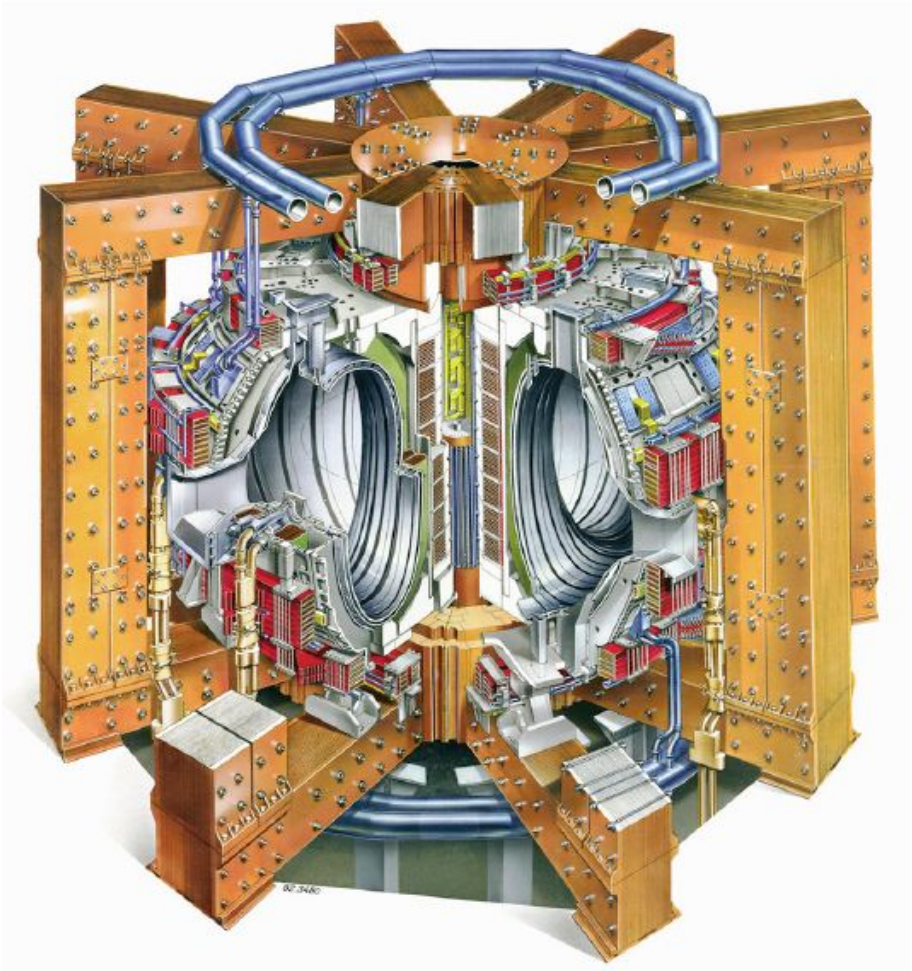

Figure 1.1: *JET tokamak, cut view.*

figuration, a total auxiliary heating power around 30MW, and with a volume of $\approx 80m^3$. In this device the work was concentrated on high β instabilities, where for β the ratio of average kinetic pressure over magnetic field pressure is intended. The most studied instabilities were Neoclassical Tearing Modes (NTMs) that have been studied and localized radially, as will be shown in Chapter 3.
The localization technique has also been used in a non conventional way to reconstruct the NTM poloidal mode number m spectrum, and to extract information on the tearing-kink structure of the mode, this work will be shown in Chapter 4.
The Impact of NTMs on JET advanced tokamak discharges has been documented as well, with the ultimate aim of using the described localization techniques to quantify the loss in plasma confinement induced by the mode as a function of mode localization, as will be shown in Chapter 5.
On JET device also q=2 fishbones have been encountered, meaning for q the magnetic *safety factor*, which measures the magnetic field line winding. The impact of these modes on Steady State operational scenario will be shown in Chapter 6, their relevance being in the triggering of other harmful MHD instabilities, such as high β continuous modes and disruptive ideal kink modes.

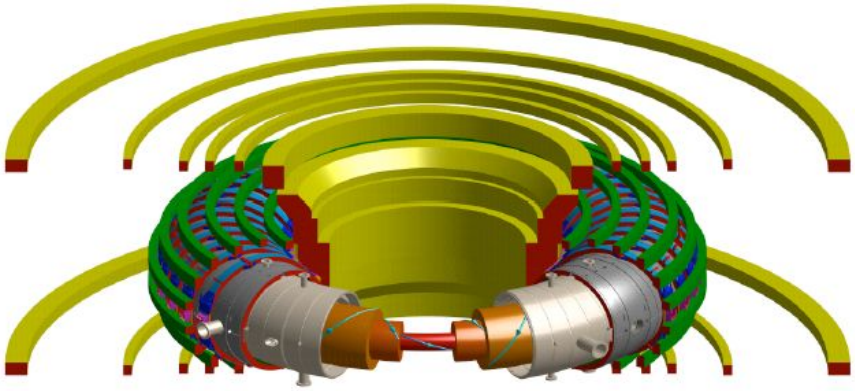

Figure 1.2: *RFX reversed field pinch, cut view.*

The second device is RFX-mod, which is the largest reversed field pinch (RFP) device in the world, with a major radius of 2m, a minor radius of 0.459m, and a plasma current up to 2MA. RFX-mod is equipped with the most advanced MHD control system ever built in a fusion device, which is composed by 192 active saddle coils that are independently fed and cover the whole surface of the torus. This makes it one of the best devices to study MHD instabilities and develop innovative active control strategies.
The work carried out on RFX-mod was focused on Resistive Wall Modes (RWM) study, these instabilities grow exponentially on the timescale of the magnetic field penetration in the device conductive structures, and, if not controlled, lead to the termination of the discharge.
During the PhD a RWM growth rate database in RFX-mod was created, which will be presented in Chapter 7. The database served as a standard reference to recognize growth rate modifications due to 3D couplings between different m and n RWM harmonics, with n the toroidal mode number. This is equivalent to determine the RWM 3D structure, as shown in Chapter 8.
The issue of the stability prediction for a system composed by an unstable plasma, conductive boundaries and active control coils will be introduced in Chapter 9, where the creation and benchmark of a dynamical RWM control simulator will be shown. Finally in Chapter 10 the results of RWM control experiments using a smaller set of active coils will be exposed.

To conclude this introduction let's see how a multimodal approach can be used for two different devices and different instabilities to get to the same conclusion: in the first case the issue is the radial characterization of the m=2 n=1 NTM eigenfunction in JET from the radial profile of electron temperature oscillations produced by the mode. The oscillation radial profile induced by a rotating magnetic island should be characterized by a π jump localized at the island radius, since the island field has an antisymmetric curvature with respect to the island center. On the other hand the radial profile of the oscillation exhibits several π jumps that can not be connected to a simple poloidal structure. After a careful analysis, the mode eigenfunction was proven to be composed by two dominant poloidal components, one tearing m=2 component resonant on q=2 surface, and a more external m=3 component, as shown in Figure 1.3. The explanation was

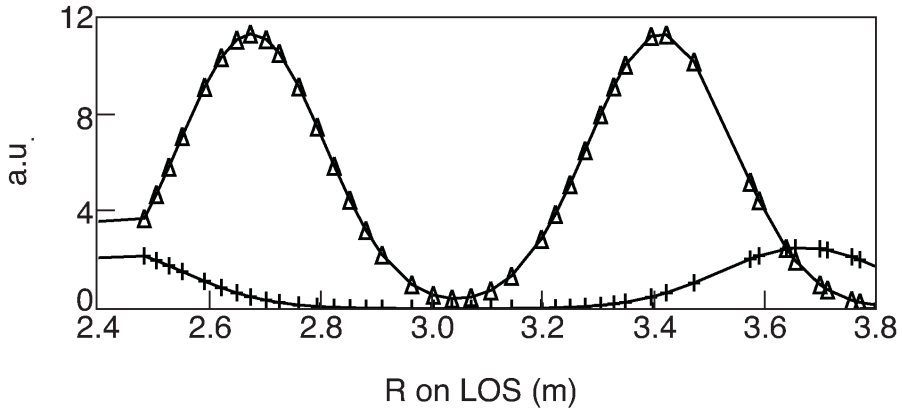

Figure 1.3: *Temperature oscillation radial profile for JET pulse 77590 at t=8s, for multiple m components. The amplitude profile for m=2 component is shown as triangles, while for the m=3 component as plus signs.*

studied in reference [1], and it is developed in Chapter 4.

In the second case the problem of the coupling between different poloidal components of the main unstable RWM in RFX-mod was faced. As shown in Figure 1.4, the active control of the m=1,n=-6 radial field component alone at the plasma boundary was sufficient to stabilize completely all of the plotted m components. This is the first hint that all of these measured components are indeed part of the same plasma instability, the demonstration was elaborated in reference [2], and it will be explained in Chapter 8.

In both cases a single harmonic approximation was not sufficient to describe the observed phenomena, while given the complexity of nowadays fusion devices a higher dimensional approach is indeed needed to explain and model correctly the experimental data.

This example was given to render the philosophy used while facing problems encountered during the presented work. The analysis approach was based on very general procedures and techniques which were each time developed and adapted to fit the particular problems encountered in different devices.

This approach permitted to unify the work carried in the two configurations, and to strengthen the physics link among instabilities in tokamaks and reversed field pinches.

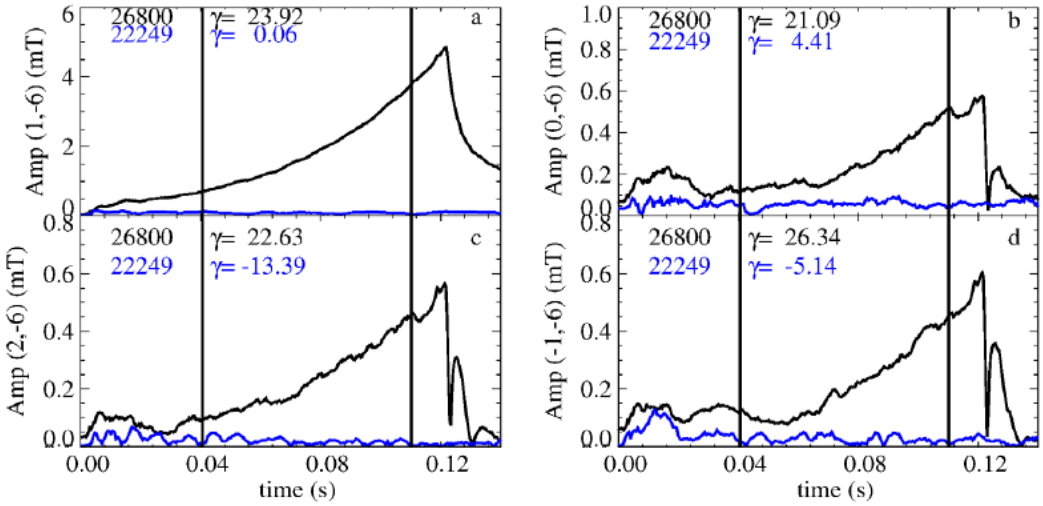

Figure 1.4: *Comparison between two experiments on RFX-mod with different control on the harmonics of the most unstable RWM,* $(m = 1, n = -6)$*. In the black case the full RWM spectrum* $(m = 0, 1, -1, 2; n = 4, 5, 6)$*, including* $(1, -6)$ *poloidal harmonics are not controlled. In the blue case the* $(m = 1, n = -6)$ *mode is controlled but the rest of RWM spectrum is not controlled. Vertical lines delimit the growth rate* (γ) *calculation interval.*

CHAPTER 2

Plasma confinement and MHD limiting instabilities

2.1 MHD limiting instabilities

Magnetohydrodynamic instabilities are among the most serious factors that limit fusion devices operation in all of magnetic confinement configurations, including tokamaks and Reversed Field Pinches (RFPs). The definition of MagnetoHydro-Dynamic (MHD) phenomena encloses all of the phenomena that can be described in the framework of MHD theory, which considers the plasma as a single, globally neutral fluid, that is composed of charged particles at the microscopic level, and therefore can conduct electrical currents and react to magnetic fields [3, 4].
MHD equations, which are the union of fluid dynamics equations and Maxwell's equations of electromagnetism, are the following:
the continuity equation:

$$\frac{\partial \rho}{\partial t} + \nabla \cdot (\rho \boldsymbol{v}) = 0 \tag{2.1}$$

the MHD force equation, which is the equivalent of Reynold's equation for magnetized fluids, and describes the motion of the fluid in response to magnetic and kinetic forces:

$$\rho \left(\frac{\partial}{\partial t} + \boldsymbol{v} \cdot \nabla \right) \boldsymbol{v} = -\nabla p + \boldsymbol{J} \times \boldsymbol{B} \tag{2.2}$$

the Ampère's law:

$$\boldsymbol{J} = \frac{1}{\mu_0} \nabla \times \boldsymbol{B} \tag{2.3}$$

and the Ohm's Law:

$$\boldsymbol{E} + \boldsymbol{v} \times \boldsymbol{B} = \eta \boldsymbol{J} \tag{2.4}$$

in the equations $\boldsymbol{E}$ is the electric field, $\boldsymbol{B}$ is the magnetic field and $\boldsymbol{J}$ is the current density. ρ is the fluid density, p is the kinetic pressure, η is the fluid resistivity, and $\boldsymbol{v}$ is the fluid velocity.

To achieve system's closure the most frequently used solution is to assume adiabatic fluid behaviour:

$$\left(\frac{\partial}{\partial t} + \boldsymbol{v}\cdot\nabla\right) p + \gamma_k p \nabla\cdot\boldsymbol{v} = 0 \tag{2.5}$$

with γ_k characteristic exponent of adiabatic transformations for a monoatomic gas. In case of Ideal MHD the $\eta\boldsymbol{J}$ term in equation 2.4 can be neglected, and, using Faraday's law, equation 2.3 becomes:

$$\frac{\partial \boldsymbol{B}}{\partial t} = \nabla\times(\boldsymbol{v}\times\boldsymbol{B}) \tag{2.6}$$

which is also called MHD kinematic equation.
MHD equations can expanded in the time fluctuations and reduced to their zero order, the stationary one, to describe MHD equilibria. The subscript $_0$ will be from now on referred to the stationary component, while the subscript $_1$ will be referred to the time-dependent component.
These equilibria are characteristic of the specific kind of device, and can be determined completely fixing boundary conditions, as the magnetic fields at the plasma edge. In the toroidal pinch devices, the equilibrium profiles of magnetic fields and currents can be obtained solving Grad-Shafranov equation [4].
Ideal MHD is able to describe part of the possible instabilities of the system, also called ideal modes, while it is not suitable to study finite resistivity effects and magnetic reconnection phenomena, which are tightly linked to the instabilities called tearing modes.
Rewriting ideal MHD equations ($\eta = 0$) as a function of average values plus fluctuating terms, and taking the first order in fluctuating quantities, the study of stability of MHD equilibria begins. All of MHD equations can be expressed as a function of $\boldsymbol{\xi}$, which is a vector describing the displacement of magnetic flux surfaces from their unperturbed position. Clearly $\boldsymbol{\xi}$ will satisfy the following equation:

$$\frac{\partial \boldsymbol{\xi}}{\partial t} = \boldsymbol{v} \tag{2.7}$$

where $\boldsymbol{v}$ is the fluctuating part of the plasma macroscopic velocity.
We can substitute 2.7 inside 2.2 equation, and use the other equations obtaining:

$$\rho_0 \frac{\partial^2 \boldsymbol{\xi}}{\partial t^2} = \boldsymbol{F}(\boldsymbol{\xi}) \tag{2.8}$$

where $\boldsymbol{F}(\boldsymbol{\xi})$ is the MHD force operator [3]

$$\begin{aligned}\boldsymbol{F}(\boldsymbol{\xi}) = {} & \nabla(\gamma_k p_0 \nabla\cdot\boldsymbol{\xi} + \boldsymbol{\xi}\cdot\nabla p_0) \\ & + \frac{1}{\mu_0}\left[\nabla\times\nabla\times(\boldsymbol{\xi}\times\boldsymbol{B_0})\times\boldsymbol{B_0} + (\nabla\times\boldsymbol{B_0})\times(\nabla\times\boldsymbol{\xi}\times\boldsymbol{B_0})\right].\end{aligned} \tag{2.9}$$

The stability of the system can be studied using the minimum energy principle. In fact the energy variation of the system δW after any arbitrary displacement $\boldsymbol{\xi}$ can be evaluated with the following equation, which expresses the work carried out by the system in the displacement of magnetic field lines:

$$\delta W = -\frac{1}{2}\int \boldsymbol{\xi}\cdot\boldsymbol{F}(\boldsymbol{\xi}) d\boldsymbol{r}. \tag{2.10}$$

If the quantity δW is positive, then the system will stay in its minimum energy equilibrium state, being therefore stable, while if δW is negative the system will loose energy moving with $\boldsymbol{\xi}$, being therefore unstable.
δW is an integral quantity that has to be calculated for each arbitrary $\boldsymbol{\xi}$, and if a negative δW is found for any of the possible $\boldsymbol{\xi}$, the system is unstable. For this reason instability can be proved for single cases, but stability should be proved in principle for an infinite number of displacements.
One way of overcoming this problem is the normal mode method, which starts expressing the displacement in the following way:

$$\boldsymbol{\xi}(\boldsymbol{r}, t) = \boldsymbol{\xi}(\boldsymbol{r}) e^{-i\lambda t} \tag{2.11}$$

which can be substituted inside equation 2.8 to get:

$$-\lambda^2 \boldsymbol{\xi} = \frac{1}{\rho_0} \boldsymbol{F}(\boldsymbol{\xi}). \tag{2.12}$$

The equation (2.12), together with suitable boundary conditions on $\boldsymbol{\xi}$, is an eigenvalue equation for $\boldsymbol{F}/\rho_0$ with eigenvalues λ^2, λ being generally a complex number. It can be demonstrated that $\boldsymbol{F}/\rho_0$ is a self-adjoint operator, and therefore λ^2 spectrum is real. For this reason the solutions space as a function of λ^2 is divided in two zones: $\lambda^2 > 0$ which has stationary solutions and $\lambda^2 < 0$ which has exponentially growing or decaying solutions [3].
In the $\lambda^2 < 0$ case the quantity $\Im(\lambda) = \gamma$ is called growth rate, and if it is negative any initial fluctuation will be damped, in the other case the mode will grow exponentially unstable. $\Re(\lambda) = \omega$ is instead the frequency of a time dependent oscillation of the mode, whose amplitude time behaviour is determined by γ.
$\boldsymbol{F}/\rho_0$ being an Hermitian operator means that $\boldsymbol{\xi}$ can be expressed as a sum of eigenvectors of equation 2.12, and therefore the stability of a complete set of eigenvectors implies the stability for every arbitrary $\boldsymbol{\xi}$.
The spatial dependence of $\boldsymbol{\xi}$ can be worked out further using the double periodicity of the torus on its angles ϑ (poloidal) and ϕ (toroidal), expressing the full displacement as a sum of Fourier components in the two angles:

$$\boldsymbol{\xi}(\boldsymbol{r}) = \sum_{m=0}^{\infty} \sum_{n=0}^{\infty} \boldsymbol{\xi}_{m,n}(r) e^{i(m\vartheta - n\phi)} \tag{2.13}$$

and the problem can be reduced to the calculation of $\delta W(\xi_{m,n})$ for each (m, n) component, where $\xi_{m,n}$ is the radial component of $\boldsymbol{\xi}_{m,n}$. The toroidal and poloidal components of $\boldsymbol{\xi}_{m,n}$ in fact can be expressed as function of the radial component [3]. For now on let's drop the $_{m,n}$ subscript, since the same stability calculation procedure can be carried out for each (m, n) component.
These simplifications lead to the mono-dimensional problem of the study of $\delta W(\xi(r))$.
Again the plasma is unstable if $\delta W(\xi(r))$ is negative for any of the (m, n) pairs, this means that the internal energy of the system can be reduced enhancing plasma's kinetic energy.

2.1.1 Classification of instabilities

The energy lost by the plasma equilibrium with the displacement can be linked to different quantities: the plasma pressure, generating *pressure-driven* instabilities, or the current density flowing into the plasma, giving rise to *current-driven* instabilities.
Another classification of MHD modes follows their resonance position: a mode is resonant in the plasma if among all of the magnetic surfaces inside the plasma one exists where the condition $\boldsymbol{k} \cdot \boldsymbol{B_0} = 0$ is valid, with $\boldsymbol{k} = (m/r)u_\vartheta + (n/R)u_\phi$ wave vector of the perturbation. If this happens the instability winds up around the torus with the same periodicity of magnetic field lines, being deleterious for mode's stability because the stabilizing effect of magnetic tension term in equation 2.9 is missing.
The magnetic shear concept is strictly related to the resonance concept: it describes the variation of the magnetic field winding angle moving radially from one magnetic surface to the next one, and is expressed as:

$$s(V) = 2\frac{V}{q}\frac{dq}{dV} \tag{2.14}$$

where V is the volume included in each magnetic surface, and

$$q = \frac{rB_\phi(r)}{RB_\vartheta(r)} \tag{2.15}$$

is called safety factor.
A strong magnetic shear is generally good for stability because it means that the magnetic tension term is small with respect to the other terms in equation 2.9 only in a very thin radial layer around the resonance surface.
Modes that can be described inside the ideal MHD framework are called ideal modes, while modes that can be described only using the full resistive MHD set of equations are called resistive modes. With finite plasma resistivity, ideal MHD breaks down around rational surfaces with safety factor $q = m/n$, and in some cases this causes locally breaking and tearing of magnetic flux surfaces, with the creation of the so called tearing modes. Tearing modes are the most dangerous class of resistive instabilities, and therefore more focus on them will be put in Section 2.2.
Another parameter linked to pressure-driven modes stability is the ratio of the plasma kinetic pressure over the magnetic pressure β:

$$\beta = \frac{< p >}{\frac{B^2(a)}{2\mu_0}} \tag{2.16}$$

where $< p >$ is the plasma kinetic pressure averaged over the poloidal section. Also used in this context are the toroidal and poloidal components of β, defined as $\beta_t = \frac{<p>}{\frac{B_t^2(0)}{2\mu_0}}$ and $\beta_p = \frac{<p>}{\frac{B_p^2(a)}{2\mu_0}}$, with B_t toroidal magnetic field and B_p poloidal magnetic field.
In tokamak physics β is often replaced by the slightly different parameter $\beta_N = 100\beta_t a B_t/I$, since it accounts for the balance between destabilizing magnetic curvature on the low field side (LFS) of the torus and stabilizing curvature on the

high field side (HFS). In the equation a is the minor radius, and I is the total plasma current in MA [5].
MHD instabilities are ultimately limiting fusion devices operational space, either because their onset is dangerous for the configuration equilibrium and can lead to disruptions, or because their appearance is enhancing plasma transport or plasma current diffusion, acting directly on their own physical drive.
Usually MHD modes rotate toroidally with respect to the plasma wall for various effects, the most simple one being the toroidal rotation of the plasma fluid itself. On the other hand a deleterious condition for the safety of the discharge happens when the magnetic mode does not rotate toroidally with the bulk plasma anymore (as it should happen in ideal MHD [3]), forming a *wall locked mode*. Wall locking usually implies an enhanced plasma-wall interaction, it spoils discharge confinement, and it worsens mode's stability as well.
Current driven modes are dangerous in tokamaks, since they induce a disruptive locked mode when the current rise rate during plasma ramp-up exceeds a certain value. They are dangerous in RFPs as well, two examples are Resistive Wall Modes, that can destroy plasma equilibrium and ultimately terminate the discharge [6], and kink tearing modes, that can lock to a certain position of the machine first wall, enhancing dramatically plasma wall interaction, and causing dangerous wall overheating.
On the other hand pressure driven modes are the most dangerous modes in tokamaks, an ultimate disruptive limit to β_N being set by ideal kink modes and Resistive Wall Modes. Anyway in most nowadays tokamaks, before this limit being hit, a softer β_N limit is set by Neoclassical Tearing Modes, which act reducing plasma confinement and therefore reducing also plasma thermal content and β_N.
In the work contained in this thesis most of the listed instabilities have been studied experimentally.
A more detailed study of these instabilities will be approached in this chapter, giving also an overview of the current research work covering these topics. The original work carried out in each topic will be shown in the following chapters.

2.2 Tearing Modes

Tearing instabilities in Tokamaks and RFPs are sustained by the radial gradient of the equilibrium toroidal current density. The growth of the instability is generally slower than ideal instabilities, because it is intrinsically linked to the timescale of magnetic reconnection process. Ideal MHD equation are not suitable to describe tearing modes in the whole plasma volume, breaking down at resonance surfaces in the plasma, where the $\boldsymbol{v} \times \boldsymbol{B}$ term in equation 2.4 goes to zero, and the $\eta \boldsymbol{J}$ term is therefore determining the time derivative of the magnetic field.
The way of studying this problem is to solve linearized MHD equations using the ideal Ohm's law from the outer side of resonant radius to plasma surface, and from the inner side of resonant radius to plasma center, while using the resistive Ohm's law in a thin layer centered on the resonant surface [4]. This calculation is usually

carried out in terms of the perturbed flux function ψ:

$$B_{r1} = -\frac{1}{r}\frac{\partial \psi}{\partial \vartheta} \tag{2.17}$$

$$B_{\vartheta 1} = \frac{\partial \psi}{\partial r}. \tag{2.18}$$

The linearized Ampère's law, taking a perturbation of the form $e^{i(m\vartheta - n\phi)}$, and substituting equation 2.18, can be cast as:

$$\frac{1}{r}\frac{d}{dr}r\frac{d\psi}{dr} - \frac{m^2}{r^2}\psi - \frac{dj_\phi/dr}{\frac{B_\vartheta}{\mu_0}(1-\frac{nq}{m})}\psi = 0 \tag{2.19}$$

it can be multiplied by ψ and integrated over the volume to give:

$$\int_{r2}^{r1}\left[B_{\vartheta 1}^2 + B_{r1}^2 + \frac{dj_\phi/dr}{B_\vartheta(1-\frac{nq}{m})}\psi^2\right] r dr = \left(r\psi\frac{d\psi}{dr}\right)_{r1}^{r2}. \tag{2.20}$$

Equation 2.20 gives the energy change due to the tearing mode outside the resistive layer. The first two terms represent the stabilizing effect of field line bending, the third one represents the energy associated to the equilibrium current gradient, while the boundary term is the Poynting flux. Since the approach is linear, only the ratio between the flux function ψ and its radial derivative $\psi' = \frac{\partial \psi}{\partial r}$ has physical meaning. The difference of this quantity between the two sides of the resistive layer is:

$$\Delta' = \left.\frac{\psi'}{\psi}\right|_{r=r_s-\epsilon}^{r=r_s+\epsilon} \epsilon \to 0. \tag{2.21}$$

The Δ' value calculated from ideal MHD flux functions outside the resistive layer must be equated to its value calculated inside the resistive layer.
Inside the resistive layer the resistive Ohm equation 2.4 is valid. Taking the curl of the equation and substituting for $\nabla \times \boldsymbol{J}$ and $\nabla \times \boldsymbol{E}$ gives

$$-\frac{\partial \boldsymbol{B}}{\partial t} + \nabla \times (\boldsymbol{v} \times \boldsymbol{B}) = \frac{\eta}{\mu_0}\nabla \times \nabla \times \boldsymbol{B}. \tag{2.22}$$

The radial component of equation 2.23 can be linearized and expressed in perturbed variables of the form $e^{\gamma t + i(m\vartheta - n\phi)}$, and equations 2.18 can be substituted. The equation can be solved together with the equation of motion, and the resulting equation determines Δ'_{in}, which is the change in ψ'/ψ across the layer:

$$\Delta'_{in} = \frac{\mu_0 \gamma}{\eta}\int\left(1 + \frac{B_\vartheta}{\gamma}\left(1 - \frac{nq}{m}\right)\frac{v_r}{\psi}\right) dr \tag{2.23}$$

where the radial integral is performed inside the resistive layer.
The equation of motion is solved as an inhomogeneous differential equation in v_r, defining the island characteristic lenght:

$$d = \left(\frac{\rho\eta\gamma r^2 q^2}{B_\vartheta^2 m^2 q'^2}\right)^{\frac{1}{4}}. \tag{2.24}$$

The integral in equation 2.23 can be carried out in the resistive layer giving the result:

$$\Delta' = 2.12\frac{\mu_0\gamma d}{\eta}. \tag{2.25}$$

Substituting equation 2.24 inside equation 2.25 leads to the expression of the tearing mode growth rate:

$$\gamma = 0.55\left(\left(\frac{\eta}{\mu_0}\right)^{3/5}\left(\frac{mB_\vartheta}{\mu_0\rho}\right)^{1/2}\frac{q'}{rq}\right)^{2/5}_{r=r_s}\Delta'^{4/5}. \tag{2.26}$$

As it can be seen the sign of the growth rate is linked to the sign of the Δ' term, a negative Δ' meaning stability, while a positive Δ' meaning instability.
Equation 2.19 can be expanded about the resonance and the continuity between the two solutions of equation 2.19 across the layer must be imposed, and Δ' must be equated to the difference in $\frac{\psi'}{\psi}$ between the two sides of the layer. Δ' is found imposing $\psi = 0$ at $r = 0$, and selecting the proper boundary condition at the plasma edge. The choice of the edge boundary condition is very important (for example choosing a perfectly conductive shell), because it acts directly on Δ' changing the mode stability.
The growth of the magnetic island associated to the tearing mode is usually driven by the same destabilizing effect that destabilizes linearly the associated mode, but the island growth is limited by the resistive diffusion physics. The physical law that describes the tearing island dynamics can be found from the equations 2.3, 2.4 and the Faraday law. Combining the three equations for the time derivative of magnetic field, and keeping only the radial component, and the radial derivatives that dominate across the island one gets:

$$\frac{\partial B_r}{\partial t} = \frac{\eta}{\mu_0}\frac{\partial^2 B_r}{\partial r^2} \tag{2.27}$$

this equation can be integrated over the island width w, taking B_r to be approximately constant across the island, and considering $B_r \propto w^2$ it can be rewritten as:

$$\frac{\partial w}{\partial t} \approx \frac{\eta}{2\mu_0}\frac{1}{B_r}\frac{\partial B_r}{\partial r}\bigg|^{r_s+w/2}_{r_s-w/2} \tag{2.28}$$

since B_r is linked to the helical flux ψ, Δ' can be recognized in the right hand side of equation 2.28, leading to

$$\frac{\partial w}{\partial t} \approx \frac{\eta}{2\mu_0}\Delta'_w. \tag{2.29}$$

Equation 2.29 is called Rutherford equation, as it stands it is valid for a simple *current-driven* tearing mode, but it does not take into account transport effects inside the island region. It can be enriched taking into account several effects that act in stabilizing or destabilizing way, as it will be discussed in Section 2.5.

2.3 The bootstrap current

Before the introduction of Neoclassical Tearing Modes and Resistive Wall Modes physics, focus will be put on the bootstrap current phenomenon, which is indeed

essential for tokamak advanced scenario operation, and represent the physical drive of NTMs as well.
In a toroidal device the poloidal symmetry typical of cylindrical geometry is no longer valid, and the toroidal field decreases with the major radius of the device R. For this reason the plasma particles with low momentum parallel to magnetic field lines remain trapped (*trapped particles*) in a bouncing orbit on the high R side of the device (low field side), while the ones with large parallel momentum can escape the magnetic trap and perform their complete revolution around the torus (*passing particles*). The effects that are introduced by toroidal geometry and are not foreseen by cylindrical theory are usually called *neoclassic*.
Trapped particles exhibit an orbit which is called *banana orbit*. Moving along field lines particles are subjected to a vertical drift due to toroidal magnetic field gradient. The drift is always directed in the same verse, and the projection of the orbit on a poloidal section of the plasma has the typical banana shape [7].
The neoclassical orbit also implies the presence of a diamagnetic current, mainly due to the radial gradient of the plasma electron density and temperature, and to the finite width of the orbit. This current must be calculated separately for trapped electron population and passing electron population, a simplified expression of the two current densities is:

$$J_t \approx -e \left(\frac{R_0}{r}\right)^{1/2} \frac{T}{B_0} \frac{\partial n}{\partial r} \tag{2.30}$$

$$J_p \approx -e \frac{T}{B_0} \frac{\partial n}{\partial r} \tag{2.31}$$

where J_t is the trapped electrons magnetization current, J_p is the passing electrons magnetization current, e is the particle charge, n is the particle density, T is the plasma temperature, r is the radial coordinate, R_0 is the major radius, B_0 is the total magnetic field at the central axis, and $\epsilon = r/R_0$ is called *inverse aspect ratio*.
The parallel momentum balance considering the collisions between passing electrons and trapped electrons leads to a nonzero value violating the equilibrium

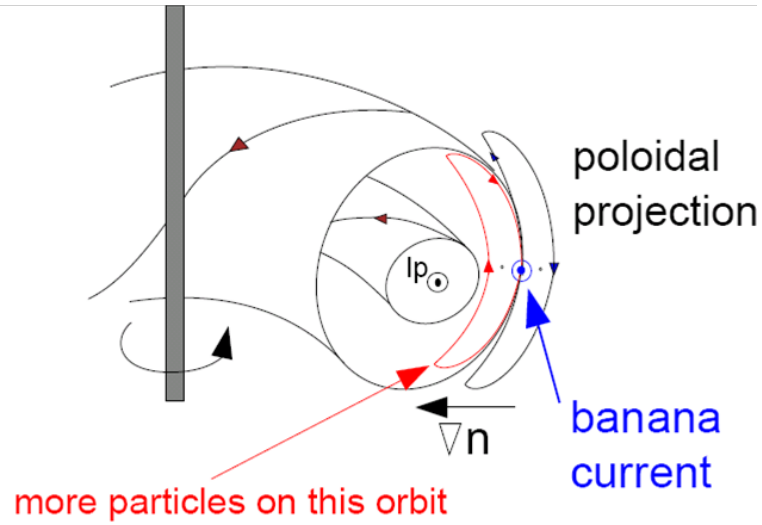

Figure 2.1: *Sketch of banana orbit.*

principle, if the momentum exchange is calculated using the polarization current expression for the two populations. The inconsistency can be solved if the passing electron velocity distribution has a non thermal parallel component due to passing electrons diamagnetism. This component can therefore be calculated from the toroidal momentum balance equation, and it generates a net parallel current which is called *bootstrap* current.
The low collisionality *bootstrap* current density expression is:

$$J_b = -4.71q \left(\frac{R_0}{r}\right)^{1/2} \frac{T}{B_0} \left[\frac{\partial n}{\partial r} + 0.04 \frac{n}{T} \frac{\partial T}{\partial r}\right]. \tag{2.32}$$

It is important to notice that the *bootstrap* current profile peaks off-axis, since $\frac{\partial n}{\partial r}/r^{1/2} \to 0$ when $r \to 0$.
In the $\epsilon \to 1$ limit it is found that

$$J_b = -\frac{1}{B_\vartheta} \frac{dp}{dr} \tag{2.33}$$

and with increasing ϵ the bootstrap current tends to be driven predominantly by the pressure gradient. This equation leads to the scaling for the ratio of the bootstrap current over the total plasma current, which is called the *bootstrap fraction*:

$$\frac{I_b}{I} = -c\epsilon^{1/2}\beta_p \tag{2.34}$$

with β_p being the poloidal β, i.e. the average plasma pressure over the poloidal magnetic field pressure at the plasma edge.
This neoclassical transport phenomenon is of huge importance for the so called tokamak advanced scenarios, because it is a spontaneous current drive effect unrelated to ohmic current drive and external current drive methods.

2.4 Tokamak Advanced Scenarios

In this section Advanced H-mode tokamak scenarios will be introduced. The H-mode is an improved confinement operational mode characterized by the formation of a steep edge transport barrier, which is generated by the reduction of electrostatic turbulence in the plasma edge [8, 9]. This transport barrier implies an important enhancement of plasma temperature in the whole plasma core, together with a cyclic MHD instability of the edge transport barrier called Edge Localized Mode (ELM). The transition from the conventional tokamak operational mode, also called L-mode, to the H-mode is triggered when a sufficient amount of power flows across the plasma last closed flux surface. This condition is reflected on a minimum input external power for the H-mode triggering which is called L-H power threshold [10].
For its improved confinement, and relative robustness, H-mode is the work-horse operational mode for most nowadays tokamaks.
A part from the mentioned characteristics, the H-mode equilibrium and current drive works as for the conventional tokamak, in the sense that most of the plasma current is driven in an inductive way via the so called central solenoid. The inductive nature anyway implies a pulsed operation, since the limited current available

in the central solenoid implies also a maximum amount of inductive magnetic flux that can be consumed in a pulse.
The advanced tokamak scenario is a particular class of tokamak H-mode in which a large fraction of the total plasma current is driven in a non-inductive way, and a considerable part of this non-inductive current fraction is generated by the plasma itself via the bootstrap mechanism. To achieve a high bootstrap fraction a high β_p is necessary. This implies that, given a fixed amount of external heating power, a smaller total plasma current is necessary (this also works for reducing the inductive fraction).
The goodness of confinement in H-mode is usually described by an empirical multi-device scaling law IPB_{98} [11], which describes plasma confinement time τ_E (in seconds) as a function of major plasma parameters. The scaling law is the following:

$$\tau_E = 0.0562 \times P^{-0.69} B^{0.15} I^{0.93} \kappa_a^{0.78} n^{0.41} a^{0.58} R^{1.39} M^{0.19} \tag{2.35}$$

where P is the external power in MW, B is the magnetic field in T, I is the plasma current in MA, n is the density in $10^{19} m^{-3}$, a and R are the minor and major radius in m and M is the mean atomic mass of the main plasma specie. $\kappa_a = \Delta/\pi a^2$, where Δ is the poloidal cross section area, is the used elongation measure. The ratio between the experimental τ_E over the one predicted by IPB_{98} is called $H_{IPB_{98}}$ factor, and it indicates an improved confinement with respect to the standard H-mode if it is larger than 1.
Since plasma confinement scales positively with plasma current, a lower plasma current implies a lower overall confinement, and therefore less fusion reactions and lower neutron rate. To reduce the loss in the total neutron rate, which is indeed one of the important parameter for a future reactor, the strategy is to seek for improved confinement regimes, where $H_{IPB_{98}} > 1$.
In these scenarios the formation and the sustainment of the correct q radial profile is very important, because magnetic shear has an effect on plasma electrostatic micro-turbulence, whose stabilization is the key for improving the plasma core confinement. A broad zero shear central region has demonstrated a reduction of turbulence in the core, leading to an improved $H_{IPB_{98}} \approx 1.4 - 1.5$ [12]. A reversed shear region also has given good results in terms of confinement, generating the so called Internal Transport Barriers (ITBs), i.e. radial zones where turbulence is suppressed, and a high temperature radial gradients build up. Internal transport barriers are generally good for tokamak scenarios, because they generate an hotter region with the consequent increase in β_p.
For these reason advanced scenarios are generated with a massive use of external heating and current drive to maximize β_p and reduce the ohmic current drive, especially during the plasma ramp up. In fact the desired q profile is obtained during the plasma ramp up, with the correct timing in the use of NBI heating, to heat the core plasma and reduce resistivity, slowing down the current profile evolution in the core [12, 13].
The current profile evolution is slowed down but not stopped completely, in fact in order to maintain the wanted current profile some off-axis current drive is necessary: Electron Cyclotron Current Drive (ECCD) and Lower Hybrid Current Drive (LHCD) are essential tools to maintain the desired current profile for a time longer than the plasma current evolution time, which is called the resistive time τ_r. The

advantage of this kind of scenarios over the standard H-mode is the lower or null flux consumption during the plasma current flat top, leading to longer or infinite discharge duration, more suitable for a reactor operation.
The advanced scenarios are generally divided in two large categories: the hybrid scenarios and the advanced tokamak scenarios. The hybrid tokamak scenario, sometimes called improved H-mode, is characterized by a q value at the edge $q_{95} \approx 4$, and a broad flat q region in the center with a value between 1 and 1.5. The plasma current is smaller than the standard H-mode one, but it is still high enough to produce a good fusion neutron rate. The non-inductive plasma current fraction is usually significant (≈ 0.5) but not equal to one. The advantage of this class of scenarios is that it is relatively resilient to Neoclassical Tearing Modes (that will introduced in Section 2.5) because of the absence or reduction of saw-teeth seeding.
The Advanced Tokamak Scenario is usually characterized by very high β and a fully non-inductive current fraction, a large part of which is produced by bootstrap current. The edge q value is $q_{95} \approx 5$, and the q profile is usually reversed in the center, with a minimum value $q_{min} > 2$. This reversed q profile has the effect of triggering internal transport barriers, leading to β enhancement and further bootstrap current, which is though localized inside the barrier, and tend to cancel the reversed shear configuration [13]. For this reason off-axis current drive is essential to the sustainment of the configuration. This configuration in principle is the most suitable to be used in future reactors, given the non-inductive character, even though the low level of plasma current at fixed toroidal field implies a smaller fusion neutron rate than the standard H-mode.

2.5 Neoclassical Tearing Modes

NTMs [14] are resistive tearing mode islands that are sustained by a helically perturbed bootstrap current. The NTMs degrade both plasma energy and plasma flow rotation, and can eventually lead to disruptions in high β_N plasmas. Studying the physics of onset and growth of these modes is of great importance both for physical understanding and for scenario development.
For a tokamak with safety factor monotonically increasing with radius and plasma pressure decreasing with radius, the parallel transport within a seed island can flatten the pressure profile within the island itself, making a helical perturbation of the bootstrap current that reinforces the seed, giving rise to a destabilizing effect.
The linear tearing stability depends on the total equilibrium current density $\boldsymbol{J}$ and safety factor q profiles (see section 2.2). For tokamaks with a safety factor at the 95% flux surface $q_{95} \approx 3$ and q on axis $q_0 \approx 1$, essentially all tearing modes are classically stable. However, the bootstrap current density j_{bs} can be perturbed leading to an additional unstable term in Rutherford equation 2.29. For a conventional tokamak with magnetic shear length $L_q = q/(dq/dr)$ positive and pressure gradient lenght $L_p = -p/(dp/dr)$ positive, the Rutherford equation is

modified as:

$$\frac{\tau_r}{r^2}\frac{\partial w}{\partial t} = \Delta' + \epsilon^{1/2}\frac{L_q}{L_p}\frac{\beta_p}{w} \tag{2.36}$$

with τ_r being the local resistive time calculated with Spitzer resistivity [15].
The assumption that L_q is positive is always verified for conventional tokamaks, but it might not be true for scenarios with reversed magnetic shear in the core, that are then stable to NTMs in the reversed shear region. Given $\Delta' < 0$, and a sufficiently large β_p value to get the NTM unstable, every island described by equation 2.36 should be unstable and growing until w reaches saturation value given by Δ'. This is not the case in experiments, whose results differ from the model for $w \to 0$. The model therefore is missing some small-island effect, that could introduce an island transport threshold for the NTM growth.
In fact the NTM mechanism starts from the assumption that the pressure gradients inside the island are completely flattened, but if the island is small enough to have perpendicular transport predominant over parallel transport, then the assumption is not valid anymore, and the NTM mechanism fails. The threshold width for having NTM unstable is therefore obtained equating perpendicular transport characteristic time $\tau_\perp \approx (w/2)^2/\chi_\perp$ and parallel transport $\tau_\parallel \approx \lambda_\parallel^2/\chi_\parallel$ characteristic time, where $\chi_\perp$ and $\chi_\parallel$ are perpendicular and parallel diffusion coefficients, and $\lambda_\parallel^2 = L_s/(k_\vartheta/2)$ is the connection length along magnetic field inside the island, with $k_\vartheta = m/r$ the poloidal wave number and $L_s = qL_q/\epsilon$.
The resulting threshold island width is:

$$w_d \approx \sqrt{2}L_s/k_\vartheta^{1/2}(\chi_\perp/\chi_\parallel)^{1/4} \tag{2.37}$$

and the Rutherford equation including a term for the small island threshold becomes:

$$\frac{\tau_r}{r_2}\frac{\partial w}{\partial t} = \Delta' + \epsilon^{1/2}\frac{L_q}{L_p}\beta_p\frac{w}{w^2 + w_d^2}. \tag{2.38}$$

The NTM is therefore linearly stable, and non-linearly unstable if the island width is larger than the critical width w_d. w_d value depends weakly on the transport model used for parallel and perpendicular transport, and most of cross-field transport models are not suitable to be applied in the spatial scales of the narrow island layer.

Other effect shall be included as well in the Rutherford equation to keep into account the complete NTM physics. The most important, other than the small island transport term, is experienced by an island which has non zero velocity in the ion diamagnetic rotation frame, where radial electric field is equal to zero. The fact that radial electric field is not zero introduces a polarization current, which is present if the island is smaller than the threshold:

$$w_{pol} \approx \left(\frac{L_q}{L_p}\right)^{1/2}\epsilon^{1/2}\rho_{\vartheta_i} \tag{2.39}$$

depending also on collisionality. Experiments confirmed that islands move in the ion diamagnetic direction (opposite to electron diamagnetic direction), corrisponding to a stabilizing effect, while the other direction would have meant a destabilizing effect. w_{pol} is predicted to be of the order of 2cm, somewhat larger than w_d.

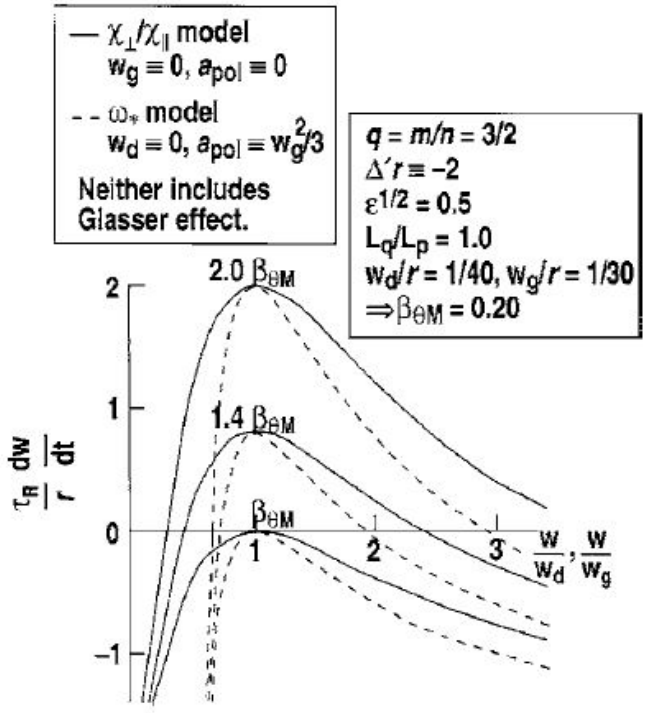

Figure 2.2: *Model curves for island growth vs island size as polidal β is increased. Solid curves represent the $\chi_\parallel/\chi_\perp$ transport threshold model and dashed curves the ω^* polarization threshold model. The labels $\beta_{\vartheta M}$, $1.4\beta_{\vartheta M}$ and $2.4\beta_{\vartheta M}$ stand for β_p and signify the curves and not the maxima. Taken from reference [16].*

Putting together these two threshholds in the Rutherford equation, the result is:

$$\frac{\tau_r}{r}\frac{\partial w}{\partial t} = \Delta' r + \epsilon^{1/2}\frac{L_q}{L_p}\beta_p \frac{r}{w}\left[\frac{w^2}{w^2 + w_d^2} - \frac{w_{pol}^2}{w^2}\right]. \tag{2.40}$$

According to this equation the NTM behaves in the following way: for a negative Δ' a sufficiently low β and small island width the NTM is stable. If for any reason the island width exceeds the critical value given by the last two terms in equation 2.40, it will grow until it reaches its saturation value. This can be seen in figure 2.2, where the NTM stability as a function of island width is shown separately for the small island transport effect (filled) and ω_{pol} effect (dashed). A change in β_p also affects the critical width, for a larger β_p a smaller width will be sufficient to destabilize the mode. The threshold value is larger for the ω_{pol} model than for the $\chi_\parallel/\chi_\perp$ model, even though the qualitative behaviour is similar.
Equation 2.40 has a non-physical behaviour for $w \to 0$, since the ion diamagnetic term goes to $-\infty$. In reference [17] an additional term has been added at the denominator of the last term to cure the non-physical behaviour. Both the approaches can be considered correct, since the diamagnetic term, a written in equation 2.40, explodes for an island width smaller than the one related to an experimentally observable NTM.

2.5.1 NTM seeding

As discussed in the previous section, high β_p NTM unstable plasma can be run without NTMs appearance if no magnetic islands are present at the resonant surface with width larger than the critical width. However many spontaneous seeding mechanisms are present in current tokamaks, which can provide the initial island that will be growing into a saturated NTM. Generally speaking any magnetic perturbation in toroidal geometry has several m components, and the richness in m spectrum is enhanced also by the effects of strong shaping typical of advanced scenarios, this effect will be studied in detail in Chapters 3 and 7. If one of these m components has the same n and m numbers of the unstable NTM, the perturbation it introduces will cause magnetic reconnection at the NTM rational surface, providing the seed island [18]. The seeding effect can be reduced if there is a radial gradient in toroidal rotation between the NTM resonant surface and the surface where the seeding mode has the largest amplitude. As a matter of fact the differential rotation can act as a shield for the radial propagation of the seed to the NTM resonant surface, if the difference in rotation is large enough [19].
The main effects that can produce a seeding island are the following:

1. $m = 1$ $n = 1$ sawteeth due to current profile peaking and q_0 lower than 1, these instabilities induce a periodical crash and magnetic reconnection events which are the most common seeding events in tokamaks.

2. $q = 1$ or $q = 2$ fishbones, which are periodical instabilities due to the resonance of MHD waves with fast ions precession frequency.

3. Edge Localized Modes (ELMs), which are periodic instabilities located at the edge of the tokamak, and are driven by a peeling-ballooning mechanism. These instabilities induce periodical crashes that release a large amount of thermal energy on the machine first wall.

4. Controlled seeding by externally applied resonant error fields.

Several experiment have been carried out to be able of predicting future devices stability to NTMs. The most widely used method is the measurement of the critical value of β_p at which NTM are stable, regardless the initial island dimension. This β_p value is identified with the solid and dashed lines which are tangent to the horizontal axis in Figure 2.2. The critical β_p value is therefore not the ultimate limit to avoid NTMs, but it is the limit over which there might be a chance of NTM onset. This quantity is not dependent on the onset physics, and can be measured by β ramp down experiments: once the NTM is triggered and the island width is on the right side of the maximum in Figure 2.2, β is ramped down until the NTM disappears, giving the critical β_p value. This is as equivalent to move from one curve to the lower next one, until the smallest unstable β_p value is found. The critical values obtained with such a method in different target plasmas and different devices have been collected and correlated to various plasma quantities, with the objective of building a scaling law to predict NTM stability in ITER. The scaling have been concentrated on the parameters $\rho^*_{i\vartheta}$, which is the ion poloidal gyro-radius normalized to the radius of the NTM resonant surface, and collisionality ν. These parameters are linked to the effect of polarization current and

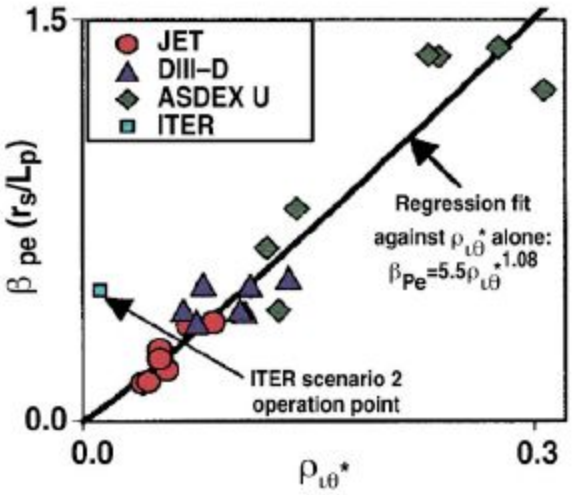

Figure 2.3: *3/2 NTM metastability threshold plotted against normalized poloidal ion gyroradius. Taken from reference [15].*

perpendicular and parallel transport. A clear linear dependence of the critical β on $\rho_{i\vartheta}^*$ has been found for all of the devices examined, which suggests a lower value of critical beta for a smaller gyroradius device as ITER, this trend is shown in Figure 2.3, where the instability threshold is plotted against $\rho_{i\vartheta}^*$ for different devices.

The NTM seeding mechanism needs to be characterized as well in order to predict

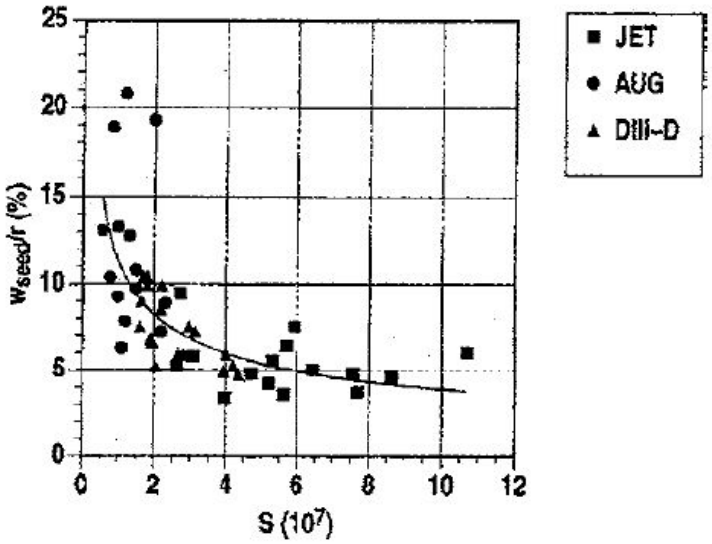

Figure 2.4: *Scaling of relative seed island $w_{seed}/r(\%)$ versus magnetic Reynolds number S at $q = 3/2$. Best fit is $w_{seed}/r(\%) = 11.3S^{-0.46\pm0.05}$ with a correlation of -0.74. Taken from reference [20].*

NTMs stability in future devices. Reconnection of magnetic field lines is a phenomenon linked to plasma resistivity, and therefore is likely to be scalable using the Lundquist number S.

$$S = \frac{\tau_R}{\tau_A} = \frac{30 I_p T_e^{3/2}}{(0.4 + 0.6 Z_{eff}) ln(\Lambda) \sqrt{m_i n_e}} \tag{2.41}$$

where τ_A is the Alfvén time, I_p is the plasma current in kA, T_e (eV) and n_e ($10^{19} m^{-3}$) are electron temperature and density, Z_{eff} is the effective atomic charge of plasma ions, m_i is the proton mass and Λ is the Coulomb logarithm.
The ratio of the seed island width necessary for destabilization over the normalized resonant radius has been studied as a function of S for different devices. The result of this plot is shown in Figure 2.4.

2.5.2 Magnetic island rotation

Tearing modes are usually rotating in the laboratory frame, and are therefore seen in magnetic probes as a time dependent oscillation which initially grows in amplitude to a saturation value, and afterwards can remain constant through the whole discharge, or eventually lock to the wall and appear as a growing mode in the integrated signals.
The determination of tearing mode rotation frequency and its prediction are important issues for NTMs, because it influences the polarization current threshold mechanism, and therefore NTM stability. Furthermore the information of rotation can be used in the opposite way as well, since given the measured rotation frequency, and given an expression of the island rotation frequency as a function of its radial location, it is possible to localize radially the mode, as it will be shown in Section 3.3.
The theory of island propagation in fusion plasmas has been evolving gradually in the last ten years, and one of the most advanced and complete models is developed in reference [21], where the island stability and rotation frequency is derived using a five fluid model, which is an extended-MHD model that incorporates diamagnetic flows, ion gyro-viscosity, fast parallel electron heat transport, the shear-Alfvèn wave, the ion sound wave, the drift wave and the average magnetic field line curvature.
The model is valid for conventional axisymmetric tokamaks, and it contains two different ordering schemes: the first ordering imposes the parallel heat transport along filed lines to be much larger than perpendicular transport across field lines of magnetic flux, particles, momentum and heat. The second ordering imposes $\epsilon_n = L_n / L_s \ll 1$ with L_n density gradient length and L_s magnetic shear length, which is usually verified in conventional tokamaks since L_n is of the order of the minor radius, while L_s of the order of major radius. This last ordering permits to distinguish between two different physics regimes, which are also linked to the island width w: the hypersonic regime where the ion sound wave can not propagate fast enough along field lines inside the island to flatten density profiles, and the sonic regime where this flattening effect can happen. The different regimes are described by the parameter α, $\alpha \ll 1$ for the hypersonic regime, $\alpha \gg 1$ for the sonic regime.

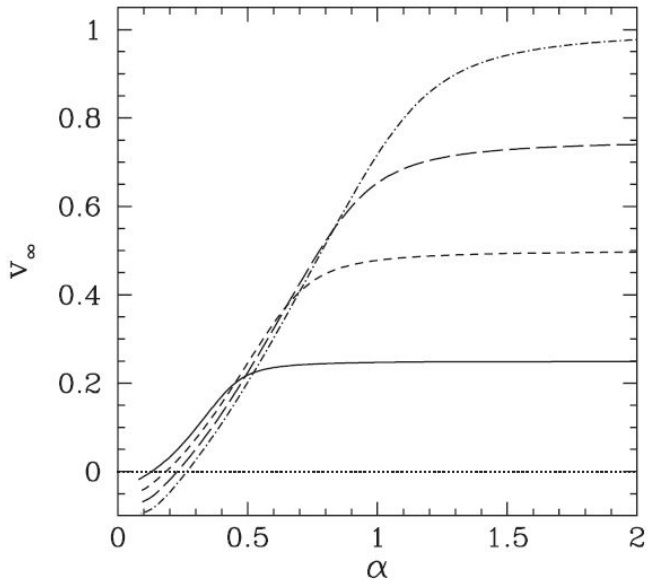

Figure 2.5: *Island rotation as a function of the ion-sound parameter. Taken from reference [21].*

In the sonic regime, which has a solution for w larger than a critical value, the larger the sound wave flattening effect, the more the island rotation speed tends to the ion diamagnetic rotation speed ω_i^*. Conversely the more the solution moves towards the hypersonic regime, the smaller is the rotation frequency in the zero electric field frame ($\boldsymbol{E} \times \boldsymbol{B}$ frame), eventually it also reverses to the electron diamagnetic rotation speed ω_e^* verse. This effect can be seen in Figure 2.5. The diamagnetic effect in this regime is found to have always a stabilizing effect.

A similar effect happens for the hypersonic regime, the solution of which cease to exists above a w threshold which is of the order of the ion sound radius ρ_s. In this case for small island width the island rotates near ω_e^*, and the rotation speed moves towards ω_i^* approaching sonic regime, i.e. having a larger w. If the unstable island starts as a small island in the hypersonic regime, it will reverse its rotation verse while getting larger until it reaches w critical, there the solution branches to the sonic regime and the island will continue growing and will finally reach ω_i^*.
In reference [22], the two fluid equations for electrons and ions are closed with the momentum balance equation on the island, taking into account the viscous stresses introduced by Neoclassical Toroidal Viscosity when the island is large enough to introduce non-axisymmetric effects.
The island rotation speed is calculated imposing a null total torque exerted on the island itself. The electromagnetic torque exerted on the island is determined by the current density component parallel to the magnetic field, which is linked to perpendicular current density $J_\perp$ by a closure equation imposed on J. The neoclassical component of $J_\perp$ has a form of a polarization current, and changes depending on the collisional regime used to describe the plasma ($1/\nu$,ν and PS) [4].
A self-consistent solution for the island rotation speed can again be derived by an

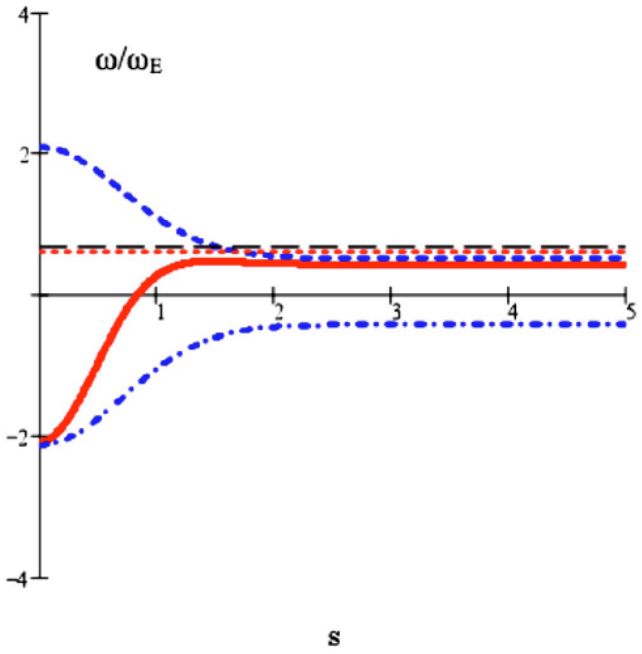

Figure 2.6: *Island self consistent rotation as a function of s in red solid line. The dashed and dashed-dotted blue curves are the island rotation in $1/\nu$ and ν regimes. Horizontal red dotted line is ion diamagnetic frequency. Taken from reference [22].*

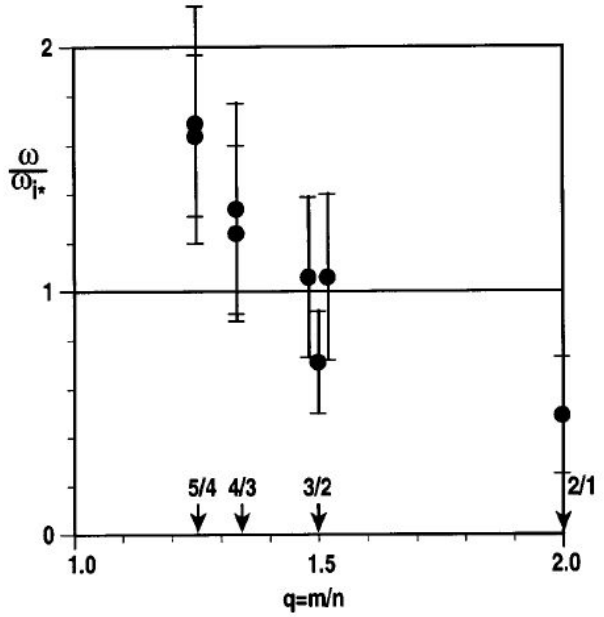

Figure 2.7: *The relative island propagation ω/ω_i^* in the frame of zero radial electric field. Error bars shown are $\pm 1\sigma$. All in ion direction. Taken from reference [15].*

ordering effect, imposing that in order to be effective in the momentum balance, the neoclassical component of the drag should be of the order of the ion perpendicular momentum diffusion term, which leads to a relation between the island width and the collisionality regime parameter s. s is the indicator for the transport regime which is dominating the neoclassical damping effect, giving ν regime for $s>1$ and $1/\nu$ regime for $s<1$.
In Figure 2.6 the self consistent island rotation is plotted as a function of s parameter. As in the previous example, the plot is describing the island frequency evolution as a function of its width, which determines the s parameter. The small unstable island will start rotating at the electron diamagnetic frequency, it will grow changing its rotation as well; it will cross zero at $s=1$, and it will finally reach the ion diamagnetic frequency, which is the saturation rotation frequency.
The NTM rotation has been studied experimentally as well, an shown in reference [15], where NTM rotation frequency has been measured in the first temporal frames after the NTM seeding, when the island is still relatively small, and neither toroidal plasma rotation is affected by the mode onset, nor locking effects are present yet.
The ion diamagnetic frequency has been carefully calculated using several diagnostics, and it has been compared with mode frequency in the null electric field frame in Figure 2.7. As it can be seen the rotation frequency is compatible with ω_i^* for $q=3/2$ NTMs, while it is slightly larger for more external modes and slightly smaller for more internal modes.

2.5.3 NTM avoidance and control

Various strategies have been developed over the years to avoid or control NTMs, the main ones are listed below:

1. To operate fusion devices in scenarios stable to NTMs: the easiest way would be to operate at β_p lower than critical β_p for NTM onset, but this would be deleterious for the device performance in terms of lower bootstrap current and lower fusion neutron rate for the same coils currents. Another strategy is to tailor the q profile to change L_q in a way to get a larger critical island width, and implies the availability of off-axis current drive tools to sustain the optimal q profile for mode avoidance. This has been tried in JET tokamak, where is one of the few key strategies to obtain improved confinement in advanced scenarios, more information on this will be given is Chapter 5.

2. To avoid the seeding process by other instabilities: making cyclic instabilities more unstable, and therefore more frequent, the related periodic crash has smaller entity and less capability of creating a seed island on the NTM resonant surface. This strategy includes the destabilization of sawteeth with ion cyclotron heating near the minority ion resonance layer [23]. For ELMs mitigation and suppression, the application of external error fields to ergodize magnetic topology near the plasma edge is used, with the aim of enhancing transport locally, and therefore making ballooning modes stable.

3. To use helical fields from other, benign, modes or externally applied fields to inhibit the perturbation of bootstrap currents for the mode of concern: the field produced by a m=4 n=3 (4/3) NTM on the q=3/2 resonant surface inhibits the helical perturbation of bootstrap current, creating the so called Frequently Interrupted Regime (FIR). In the FIR 4/3 and 3/2 NTMs are alternating, avoiding the 3/2 island to grow too large and affect transport in a significant way [24].

4. To Apply radio frequency (RF) power and current drive at mode rational surfaces: the current drive localized at the resonant surface has the double action of changing locally the current profile, in such a way to make Δ' more negative and the mode more stable, and replacing the missing helical current inside the magnetic island [25].

The physics of all of these methods have been deeply investigated in the references, but they won't be inspected here, since they are not essential to the development of the topics of the thesis.
The original work on NTMs carried out at JET consisted in the development of a radial localization method based on the coherence between Electron Cyclotron Emission (ECE) signals and the magnetic signal of the mode, and in the benchmark of the results of with other localization techniques and q profile measurements. The method has been used in a novel way also for the evaluation of the NTM m number structure.
The NTM stabilization methods have been listed anyway in this Section to highlight the importance of a good NTM localization technique to permit the NTM stabilization using active control with localized current drive methods.

2.6 Resistive Wall Modes

One of the most stringent limiting factors for tokamak steady state-high β_N operation is given by ideal kink instabilities, also called Resistive Wall Modes (RWMs). This name is due to the behaviour of these instabilities in presence of passive structures with finite resistivity placed near the plasma surface, which can lower the growth rate of these modes down to the time scale of magnetic field penetration through the resistive wall [3, 26, 27]. The stabilization is effective if the passive structures are sufficiently close to the plasma surface, and lasts until the magnetic perturbation produced by the mode penetrates the passive structures, as it is shown in Figure 2.8.
RWM 3D structure in tokamaks is usually characterized by one or more toroidal components, the main one being n=1, and might have a rich spectrum of poloidal mode numbers m=2,3,4, especially for strongly shaped plasmas. This is related to the fact that the mode has a *Ballooning* character, i.e the displacement is localized in the low-field size of the tokamak, where field line curvature and kinetic pressure gradient couple in an unstable way [3].

RWM stability introduces two limiting points of tokamak operation in plasma pressure, which also reflect on two β_N limits: the lower of the two is the no-wall β_N limit, which is the limit for MHD stability of tokamak plasmas without any

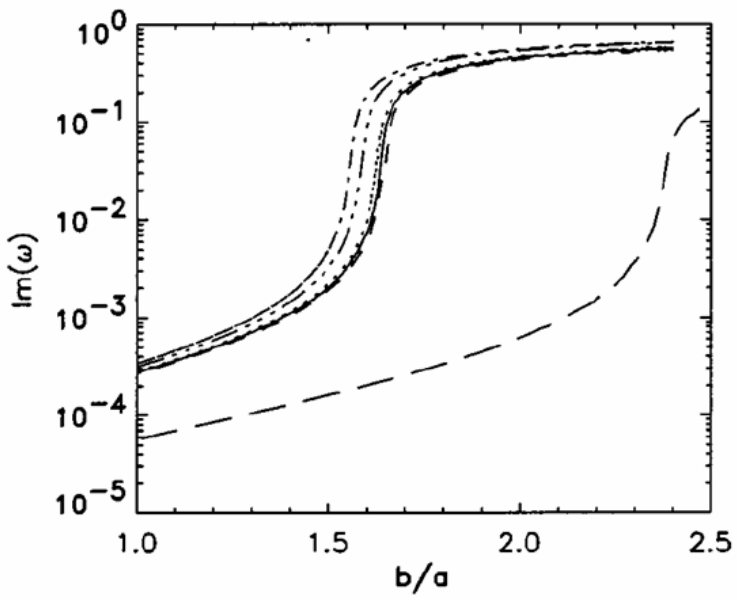

Number	Curves	α	Θ_o	F	Θ	χ	β_p
(1)	– – –	5.50	1.5	−0.18	1.48	0.0	0.0
(2)	-------	9.66	1.5	−0.59	1.60	0.0	0.0
(3)	——	5.45	1.6	−0.59	1.72	0.0	0.0
(4)	· · · ·	3.86	1.7	−0.59	1.80	0.0	0.0
(5)	–···–···	8.16	1.5	−0.59	1.93	1.0	0.081
(6)	–·–·–·	7.50	1.5	−0.59	2.17	1.8	0.15

Figure 2.8: *RWM stability plot in a RFP for different equilibria. Mode growth rate is plotted as a function of the the ratio between the wall (b) minor radius and plasma surface (a) minor radius [28].*

conductive shell around it, and the higher is the ideal wall β_N limit, and it identifies the maximum point of operation at stable MHD in the case of a perfectly conductive wall around the plasma [29, 30].
Experiments showed that current driven RWMs are present in tokamaks as well, and the free energy for their growth is provided by gradients in plasma current transiently induced during plasma ramp up, or when the q value at the edge of the plasma is lower than 2. This other RWM branch in tokamaks is more similar to the one that is observed in RFPs, and as the RFP one it is more reproducible. For this reason current driven RWM excited in the plasma ramp up have been used recently to optimize RWM control system in DIIID tokamak [31].
In Reversed Field Pinches (RFPs) an unstable branch of non-resonant, current driven, ideal kink modes is present as well, which grows on the timescale of the wall time, and therefore is called RWM branch. These modes were observed for the first time when a new generation of RFPs with a thinner conductive shell around the plasma was built. In the new experiments the conductive shell, which is indeed devoted to the stabilization of the large spectrum of unstable modes typical of RFPs, had a vertical field penetration time smaller than the discharge duration,

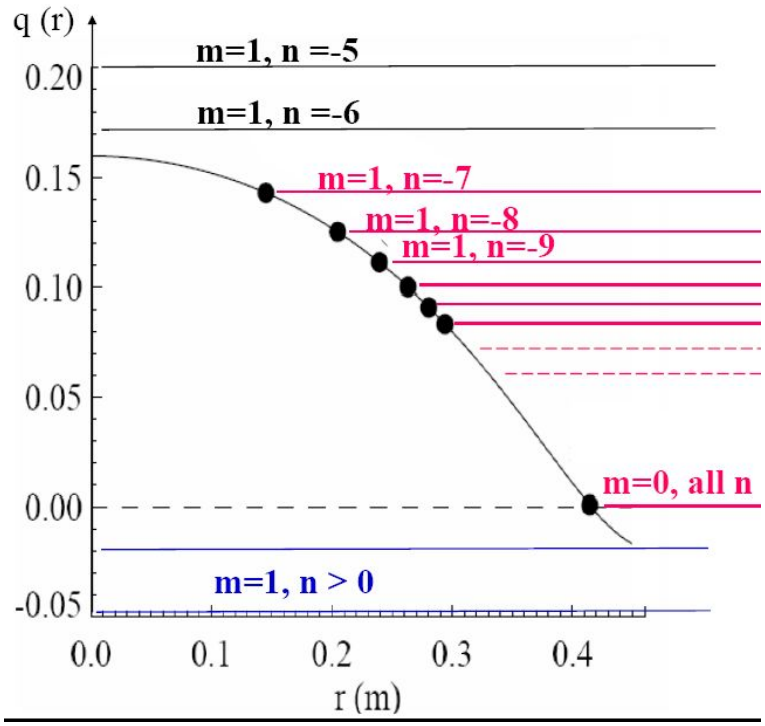

Figure 2.9: *Sketch of the possible resonant modes in RFX-mod.*

and therefore the RWM growth rates were large enough to be observed and studied [32]. In this case the mode has a main m=1 structure (according to cylindrical theory, only m=1 modes should be unstable) [27, 33], with several independent n components that can be unstable at the same time.
Possible kink modes in a RFP can be visualized in Figure 2.9, where a typical q profile in RFX-mod is shown as a function of minor radius. As it can be seen there are several resonances for modes having m=1 and $-7 > n > -\infty$, each of these resonances is linked to an unstable tearing mode, the most internal (n=-7) being also the most unstable. In the real device operation all of these modes grow to a saturated level, producing a large magnetic chaos, large plasma-wall interaction and poor confinement into the plasma core.
Also non-resonant modes are usually present in RFPs, one branch has m=1 and negative n values, i.e. the same winding direction as resonant modes inside the toroidal field reversal surface; the other has positive n, and the same winding direction as modes resonant outside the reversal surface.
In presence of a resistive wall surrounding the plasma the former are called *internal RWMs*, while the latter are called *external RWMs*. One of the two branches is usually unstable and the other stable, but which of the two depends on plasma equilibrium, as will be discussed in Chapter 7.
A typical m=1 magnetic amplitude spectrum in RFX-mod is shown in Figure 2.10 without active control (blue) and with active control (red). The measured amplitude is obtained during the flat-top from radial field sensors signals via spatial Fourier transform.

2.6.1 RWM stabilization and control

If not controlled RWMs are dangerous in both tokamaks and RFPs, being the main disruptive instability encountered during normal operation [29, 30, 34]. For this reason several stabilization techniques were developed in the last years, and some of these are common to the two configurations. The so called passive stabilization, which is based on the effect of plasma rotation, consists in the injection of angular momentum into the plasma via Neutral Beam Injection. Theory suggests that plasma toroidal rotation can be effective in stabilizing the mode, provided the rotation achieved to be larger than a critical value Ω_c, which is usually of the order of some % of the Alfvèn frequency [19, 35]. Experimental observations instead showed that $\omega > \Omega_c$ is a sufficient condition for stability until $\beta_N < \beta_{noWall}$, after this value the rotation velocity decreases down to a value smaller than Ω_c, and a Resistive Wall Mode is triggered (See Figure 2.11) [34].

This stabilization method is effective in present tokamaks [35], but not in RFPs [28], and it is yet not clear if it will be effective in ITER, for the limited amount of external torque that can be provided to the plasma using high energy NBI. Also latest experimental results demonstrate that RWM stability can be maintained with a rotation speed of some percent of Alfvén velocity, [36, 37, 38], provided that the magnetic boundary is optimized and error field reduced. This confirms theoretical prediction that show how Ω_c can be reduced taking into account kinetic stabilization effects due to the resonance of plasma rotation frequency with the precession frequency of passing ions and the bounce frequency of trapped ions [39, 40].

In figure (2.12) an example of stability window as a function of plasma toroidal rotation Ω_ϕ and of k

$$k = \frac{\frac{1}{d_c} - m}{\frac{1}{d} - m}$$

where d is the distance between the conductive wall and plasma suface, while d_c is the maximum distance to achieve stability in ideally conducting wall case.

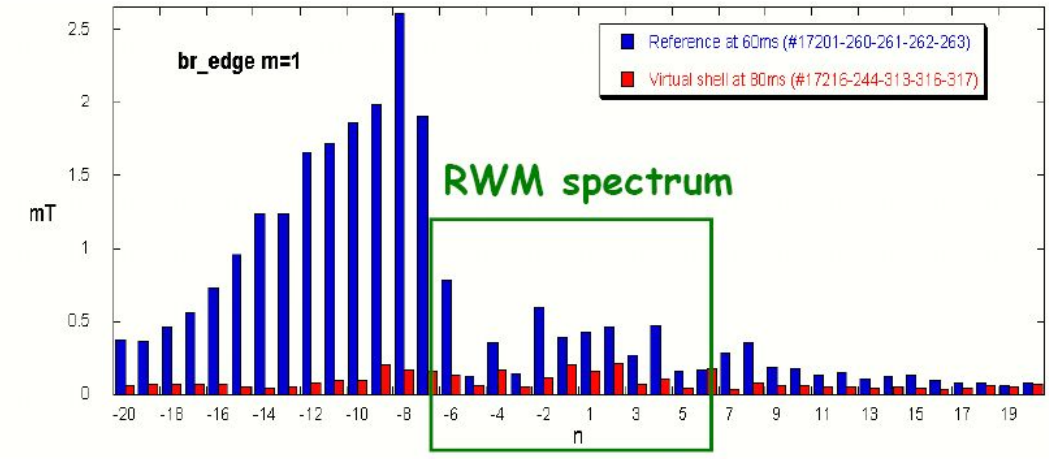

Figure 2.10: *m=1, several n amplitude spectrum in RFX-mod at $t = 40ms$.*

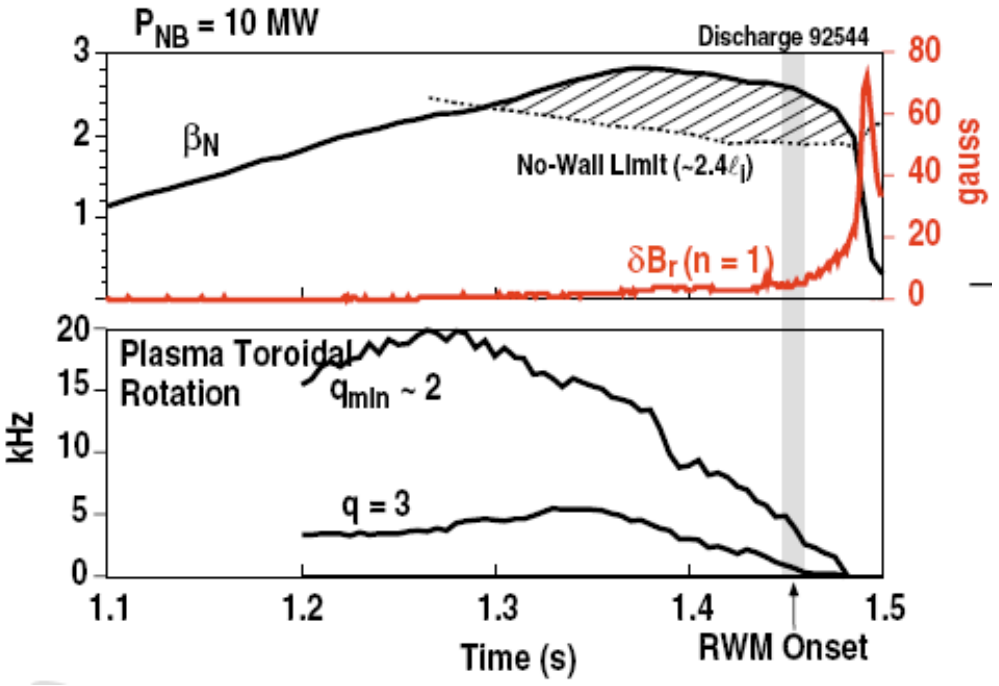

Figure 2.11: *β_N and toroidal rotation evolution as a function of time. The toroidal rotation decays after the no-wall limit is crossed, and eventually the RWM is triggered [34].*

On the other hand the active feedback stabilization at the plasma boundary by active coils has proven to be effective in fully stabilizing RWMs both in tokamak and in RFP configurations [41, 42].
Both in tokamaks and RFPs the feedback stabilization acts essentially to cancel non-axisymmetric magnetic field at the plasma edge by mean of an external set of active saddle coils, able to produce a radial magnetic field opposite to the mode's one. The technique can be carried out using two different approaches: the first one is to detect and stabilize in real time unstable modes addressing non axi-symmetric magnetic field as a feedback variable, or sometimes controlling the plasma response obtained subtracting the magnetic field produced by active coils to the measured one [41].
The second approach, which is applied mainly in tokamaks, is to use the control system to correct error fields at the plasma boundary. Error fields are stray fields different from plasma modes, that are usually produced by non axi-symmetry of conductive structures that surround the plasma. These fields, even being of the order of % of the total magnetic field, can be very deleterious to tokamak discharge interacting with the plasma in a dissipative way, damping toroidal rotation, and therefore worsening passive stabilization [43]. Error fields can also interact with modes that rotate with the plasma, causing the mode to lock to the wall. As already anticipated wall locking is deleterious for mode stability, this can be understood naivelly if we think that a rotating mode translates into an field oscillating in time at a certain position of the torus, while a locked mode translates into a

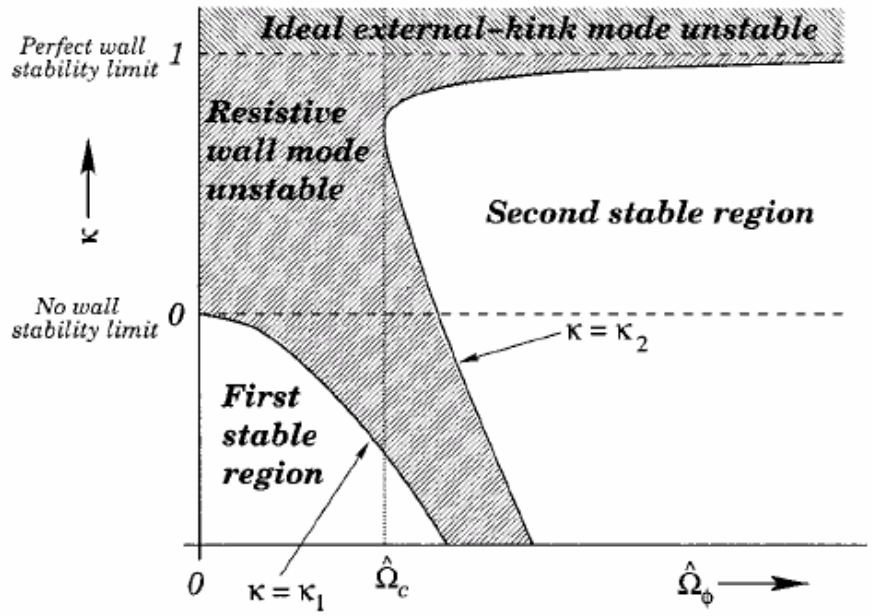

Figure 2.12: *Stability window in a tokamak as a function of toroidal plasma rotation [19].*

non-oscillating magnetic field which can penetrate into the wall.
The first approach, though deeply used in tokamaks devices as well, is the main strategy for RWM control in Reversed Field Pinches, since RWMs grow as locked modes from the beginning of the discharge.
Among RFP devices RFX-mod is, together with Extrap-T2R, the largest one and the best equipped for RWM study and active control. The RFX-mod active control system permits several different RWMs control studies, such as the simultaneous control of different RWMs, Induced RWM rotation experiments [44, 45], the exploration of RWMs mutual coupling, the study of RWM control using different sets of active coils, and the benchmark of predictive stability codes.
The last issue is indeed a very important point if we want to be able to predict RWMs growth rates given the plasma equilibrium and the 3-D structure of conductors that surround the plasma. Some codes that can perform this task are already available in fusion community [46, 47, 48], but lack a comparison with a very robust and reliable experiment where RWMs growth rates are reproducible and easy to measure, which could work as a testbed for the improvements of these codes, such as RFX-mod.

2.7 Resonant Field Amplification

Resonant Field Amplification (RFA) is a phenomenon linked to the presence of magnetic field errors which perturb the poloidal and toroidal symmetries of fusion devices. These error fields can be due to any conducting structure not symmetric in poloidal or toroidal direction, which during the discharge develop eddy currents.

Eddy currents are influenced by the 3D geometry of the conductors, and therefore the field they produce will not be axi-symmetric as well. Such 3D features, for example portholes in the vacuum vessel, are very complicated especially for tokamak devices, which need many accesses to the plasma for external heating. Error fields are also usually time dependent, since eddy currents depend on the poloidal and toroidal field, which can vary, especially during the ramp up and down of plasma current.
The basic idea of RFA is the resonant interaction between the mentioned error fields and the MHD modes, being resonant two different magnetic perturbations with the same m and n components. The interaction can lead to a damping or an amplification process, depending on the stability of the considered field harmonic. To describe the process in the RWM case, let us start from the equation describing the single harmonic RWM dynamics in the presence of an external magnetic perturbation, such as an error field [49]:

$$\tau_v \frac{\partial b}{\partial t} = \Gamma b - \Gamma_w b_{ext} \tag{2.42}$$

where b is the radial component of the considered field harmonic, b_{ext} is the radial component of the error field resonant with the chosen harmonic, $\Gamma = \gamma\tau_v$ is the RWM growth rate normalized to the wall time, and Γ_w is the stability index in vacuum, relative to the chosen harmonic, which depends on the device geometry and on τ_v. The convention is that $\tau_v = \mu_0\sigma b h/2$ is the penetration time of the vertical component of the magnetic field, while τ_w is called *long wall time*, and it is twice as long as τ_v. In the equation b is the average wall minor radius, h is the wall thickness and σ is the wall conductivity.
If the mode (m, n) spectrum is composed by more than one component, equation 2.42 is recast in matrix form, with $[b]$ column vectors, and $[\Gamma]$, $[\Gamma_w]$ diagonal matrices.
If the perturbation is stationary then $b_{ext} = b_{err}$, and the solution of equation 2.42 is given by:

$$b_{stat} = \frac{\Gamma_w}{\Gamma} b_{err} \tag{2.43}$$

therefore the perturbation amplitude is amplified if $\Gamma_w > \Gamma$, and the effect is larger for modes near, marginal stability $|\gamma| \ll \tau_w^{-1}$.
The RFA amplitude is expressed as:

$$A_{RFA} = \frac{b - b_{ext}}{b_{ext}} = c_s \frac{1 + \gamma\tau_w}{-\gamma\tau_w} \tag{2.44}$$

where b is the total measured radial field, b_{ext} is the part of it which is linked to the error field, and c_s is a geometric factor [50]. If the perturbation is rotating the simple model can be extended to

$$A_{RFA} = c_s \frac{1 + \gamma\tau_w}{i\omega_{ext}\tau_w - \gamma\tau_w}. \tag{2.45}$$

The maximum amplification is therefore foreseen for perturbation rotating with the frequency $\omega_{ext} = \omega$, and the amplification amplitude is the larger the nearer to mode marginal stability ($|\gamma| \ll \tau_w^{-1}$).

This effect has been documented in tokamaks and RFPs, and in both cases it has been studied deeply by mean of magnetic perturbations produced by active control coils [49, 50], which were pre-programmed ad-hoc for the RFA study.
In both the configurations the results agree with the simple model, in the DIIID tokamak an experimental scan of A_{RFA} as a function of the external perturbation rotation frequency was carried out, finding a resonance with the plasma flow rotation frequency. As already stated, A_{RFA} is also dependent on how far the plasma mode is from marginal stability, and this in turn for tokamaks depends on β_N. This statement is confirmed by the fact that experimental A_{RFA} has a large enhancement when β_N exceeds β_{noWall} [50]. Above this limit the large amplified field is also generating eddy currents is the passive structures, which dissipate energy resistively and have a damping effect on plasma rotation, with the mechanism explained in [43]. The rotation damping is indeed a deleterious effect in tokamaks, since rotation is one of the main actors in RWM passive stabilization, as explained in Section 2.6.
RFA studies have been carried out as well in the RFP device Extrap-T2R, where the amplification has been observed for small n modes, which are usually marginally stable. The observed A_{RFA} was slowly growing for the whole discharge, and no saturation was observed, even because of the short discharge duration. In this device also RF damping has been documented ($A_{RFA} < 1$), since the amplitude of a stationary perturbation on the stable mode ($m = 1, n = 22$), which was produced with the active coils system, has been shielded by the plasma, with respect to its amplitude in vacuum [49].
The RFA phenomenon was also observed in RFX-mod, in the particular form of the amplification of error fields produced by the control of the most unstable RWM using a reduced set of active coils. This will be shown in Chapter 10.

2.8 Fishbones

In this section the fishbone instability will be introduced. Fishbones are cyclic q=1 kink instabilities observed in tokamaks in presence of energetic ions injected in the plasma by external heating systems. The effect that can lead to an energy transfer between fast ions and MHD waves in the plasma is called Landau damping [51], and can happen when the fast ion motion around the torus is resonant with the toroidal frequency of the wave. In this case energy is transferred from fast particles to the wave.
In the fishbone case the resonance occurs with trapped ions population, which is drifting around the torus, following the movement of the banana orbit, since at each bounce point the orbit is shifted toroidally [52]. The drift velocity of the trapped particles can be calculated from the perpendicular velocity of the particles, and in case of strongly trapped particles it has the form:

$$v_{d\phi} = \frac{q v_\perp^2}{2\omega_c r} \tag{2.46}$$

where ω_c is the ion cyclotron frequency and $v_\perp$ is the velocity component perpendicular to magnetic field.
The MHD stability analysis leads to a dispersion relation for ω that has a term

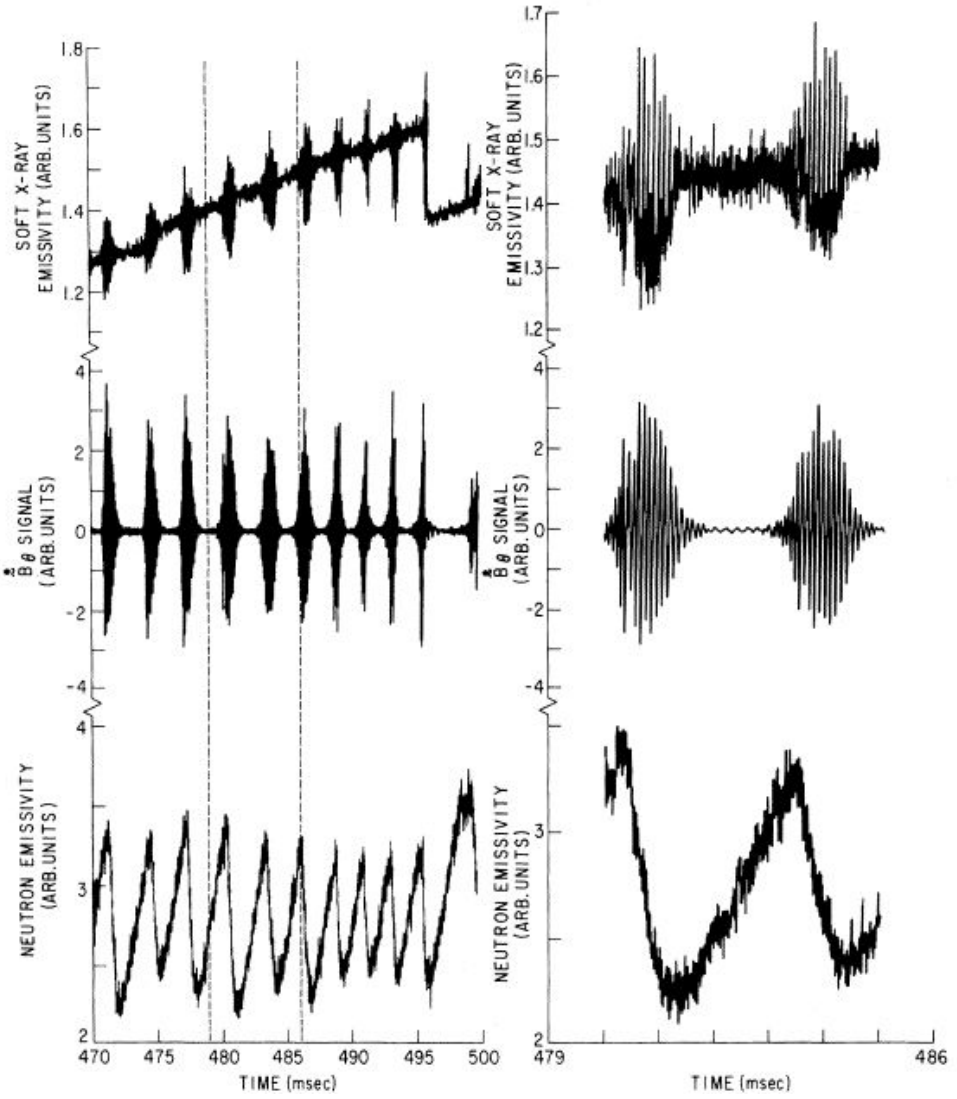

Figure 2.13: *The time evolution of the Soft-x-ray emission along a central chord, the $\dot{B}_p$ signal from a coil near the outer wall of the vacuum vessel, and the fast neutron flux. Expansion of the data near the two fishbones is also shown. Taken from reference [53]*

which describes the contribution from trapped particles, and depends on $\partial f/\partial r$, that is the radial gradient of the fast particles distribution function f.

In the case of a steady state equilibrium distribution function, assumption that is valid if the ions are injected at a certain energy and then slow down to the plasma thermal energy, an approximate dispersion relation can be found:

$$-\frac{i\omega}{\omega_A} + \delta\widetilde{W}_p + \alpha\beta_h \frac{\omega}{\omega_{dm}} ln\left(1 - \frac{\omega_{dm}}{\omega}\right) = 0 \tag{2.47}$$

where α is a quantity of the order of unity, $\omega_{dm} = v_{d\phi}/R$ at the ion injection, $\omega_A = (B_\phi/R)(\mu_0\rho)^{1/2}$ and $\widetilde{W}_p$ is the normalized MHD potential energy change in the plasma produced by the kink mode. The first two terms of equation 2.47

describe the m=1 internal kink dispersion relation, the last term describes the energy given by the trapped ions population, that is proportional to β_h, which is an effective β for fast particles.
In case of marginal kink stability ($\widetilde{W}_p = 0$) the real part of equation 2.47 gives the critical β_h value to get instability:

$$\beta_h = \frac{\omega_{dm}}{\alpha\pi\omega_A} \tag{2.48}$$

and the solution of equation 2.47 gives a resonant rotation frequency which is half of ω_{dm}.
Using a more general assumption on the dispersion relation gives a mode frequency that can range from ω_d down to ω_{*i}.
Fishbones have been observed experimentally in several tokamak devices, giving the same experimental signature in the magnetics and Soft-x-ray signals [53], as shown in Figure 2.13. Each fishbone event is characterized by an exponentially growing oscillation to a saturation level, which decays on its own afterwards.
The fishbone impact on the thermal content of the plasma is usually negligible, as it can be seen in the soft-x-ray signal, where the oscillation is detected, but the background radiation level after it is unchanged.
On the other hand the fast ion content in the plasma is deeply reduced during the fishbone, as it can be seen in the neutron emissivity.
The mode action on the fast ion population is such to expel fast ions from the plasma, reducing β_h and therefore becoming stable itself. After the mode disappears the fast ion population builds up again, and the instability reappears, that's why the cyclic behaviour.

2.9 Instabilities in the operational domain

In this section the distribution of instabilities in the operational domain will be explained, to give the reader a better feeling of the instabilities that can be encountered in Advanced Scenarios.
A simplified cartoon of the operational space is given in Figure 2.14, where β_N is plotted against q_{min}. In the cartoon the operational zones of the two main scenarios treated in the thesis are shown as blue ellipses: the hybrid scenario with q_{min} slightly above 1, and the Advanced Tokamak with q_{min} slightly above 2 and a larger β_N.
The simplified operational regimes are limited by MHD instabilities both in q_{min}, where fishbones and sawteeth limit the current penetration via and current redistribution effects, and in β_N, where ideal kink modes or RWMs determine the no-wall β_N and the ideal-wall β_N limits.
The operational domains where instabilities can be found are shown as red ellipses: NTMs constitute a first soft limit, which determine the maximum β_N that can be reached in the two scenarios enhancing transport, and therefore disabling the rise in β_N.
If NTMs are avoided or stabilized, a higher disruptive limit is given by RWMs, which can be encountered above the no-wall limit.

A q=2 fishbone constitute a vertical ellipse, because it appears when q_{min} is around 2, and can act as trigger for both the listed instabilities. The two described scenarios have been optimized to stay within operational zones without dangerous instabilities, but in some cases the operation in these domains is not maintainable for longer than τ_r without proper current drive techniques.

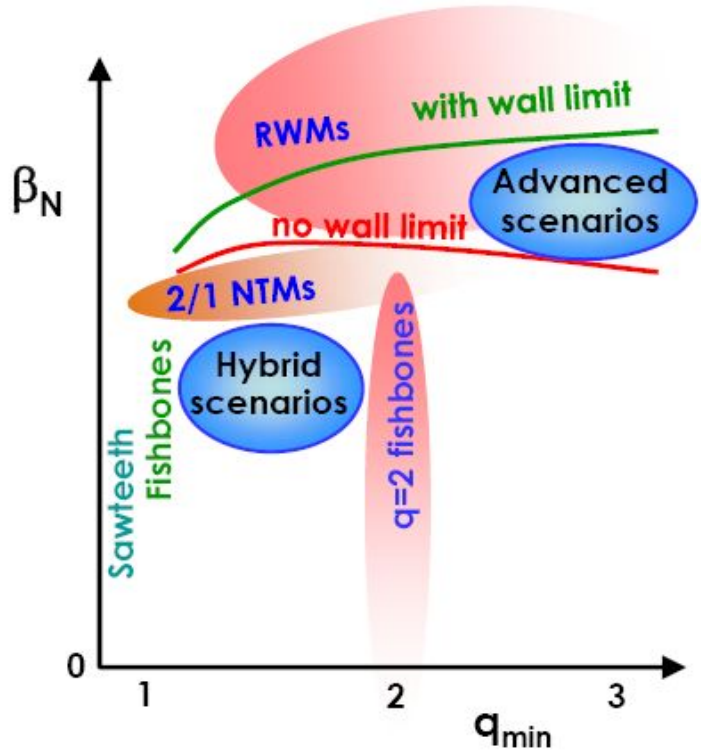

Figure 2.14: *Cartoon of the various instabilities that can be found in the operational space as a function of the central q value (q_{min}) and β_N.*

CHAPTER 3

Tearing mode radial localization techniques

In this chapter different radial localization techniques for tearing modes will be shown, and the results of these techniques will be compared with q profiles in JET obtained with Motional Stark Effect diagnostic.
The performance of Tokamak Advanced Scenarios is deeply linked to the shape of the q profile, as described in Section 2.4. The direct measurement of q is a challenging diagnostic issue, due to the inaccessibility of high temperature plasma regions to material probes. Significant information can be obtained by the Motional Stark Effect (MSE) diagnostic, which measures the direction of the local magnetic field by the polarization of radiation emitted by fast neutral beams [54].
Information on the radial q profile can also be extracted by the radial localization of magnetic islands, which are linked to tearing modes that resonate on surfaces where $q = m/n$, as described in Section 2.2.
Two methods have been studied to localize these islands, the first one identifies the island radius as the position where the temperature oscillation radial profile, associated to island rotation, exhibits a π phase jump. The second method assumes that at the resonant radius the island rotation frequency matches the ion diamagnetic frequency in the frame with zero radial electric field, i.e. $\omega = \omega_i^* + \omega_{E\times B}$.

3.1 Current profile measurements at JET

A full description of the tokamak magnetic equilibrium can be obtained by solving the Grad Shafranov equation [4], which describes the balance of plasma kinetic and magnetic pressure as a function of poloidal and toroidal magnetic fluxes, and can be solved numerically imposing the peripheral boundary conditions on magnetic fields. The equilibrium reconstruction of a tokamak discharge can therefore be obtained using experimentally measured fields as boundary conditions.
However this procedure leads to large uncertainties in the plasma core. In a well-diagnosed tokamak there are several diagnostic inputs, which can be used to constrain or supplement the equilibrium reconstruction: namely Thomson Scattering,

Core Spectroscopy and Electron Cyclotron Emission (ECE) provide profiles of the electron and ion temperatures and densities to evaluate the kinetic pressure; while some knowledge of the line averaged magnetic field and plasma rotation is also available from Faraday rotation and Charge Exchange Spectroscopy (CSX) [55].

The most relevant contribution to the description of the magnetic equilibrium is obtained from the Motional Stark Effect (MSE) diagnostic, which measures directly the pitch angle of magnetic field lines. This technique relies on the observation of the D_α line emitted by the fast neutral Deuterium atoms injected in most tokamaks for additional heating. Due to the high electric field experienced by the particles moving in the magnetic field, one of the Stark-split components of the D_α line is polarized in the direction of the magnetic field. Polarimetric measurements [56] can thus provide the local magnetic field orientation at the intersection of the line of sight with the beam. A typical layout for the MSE diagnostic is illustrated in Figure 3.1.

The accuracy of this technique is very high although it can be hampered by the presence of background-polarized radiation. Although the MSE polarization angles can be measured precisely, they do not independently determine the shape of the plasma magnetic surfaces. As a consequence, MSE data can be used more profitably as a constraint to magnetic equilibrium reconstruction codes. Equilibrium simulations including constraints from the diagnostics listed above give better descriptions of the magnetic surfaces and of q-profiles.

3.2 ECE coherence technique

Tearing Modes lead to magnetic field reconnection and then to the generation of magnetic islands chains, which have the same poloidal and toroidal periodicity of magnetic field lines at the resonant surface. The radial position of magnetic island chain is hence tightly linked to the resonant surface.

In order to detect the radial position of island chains, a time-frequency domain

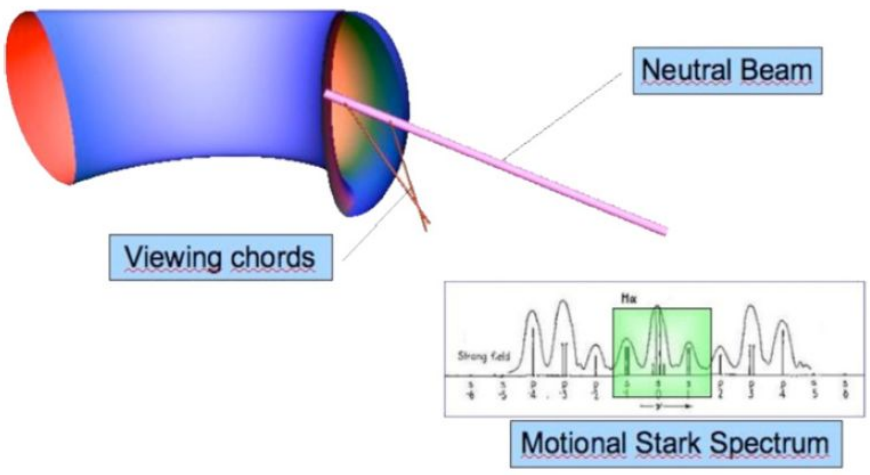

Figure 3.1: *Schematic of MSE diagnostic*

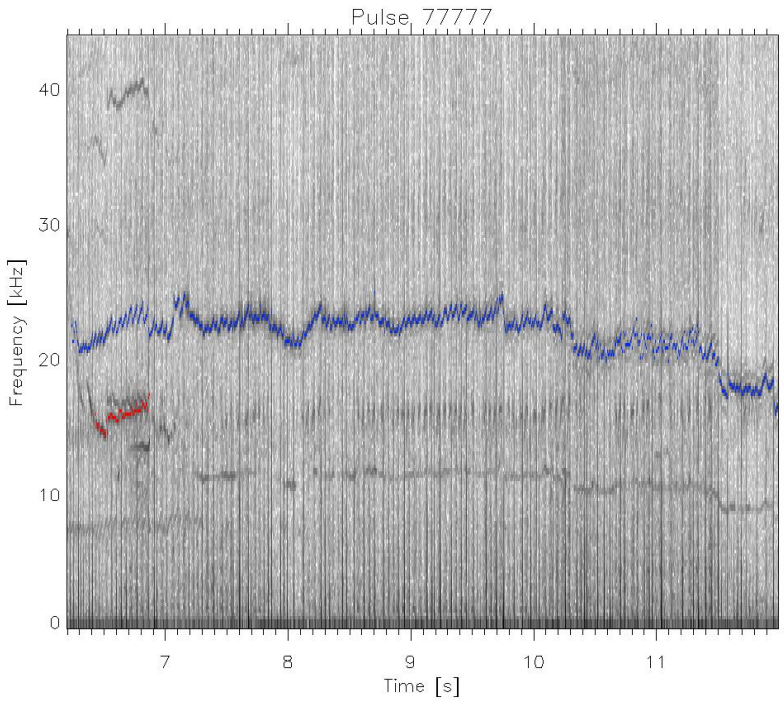

Figure 3.2: *Magnetic spectrogram from a 1MHz bandwidth pick up coil for discharge 77777. Red tracks are linked to n=1 activity and blue tracks to n=2 activity.*

coherence technique, Welch's method [57], was implemented using two different diagnostic measurements: the signal from a tangential magnetic pick up coil and the set of 48 signals from the ECE fast radiometer which measures the radial profile of electron temperature and its time oscillations.
This activity, along with the work presented in Chapter 4, was carried out as the leading author during several visits to JET Culham laboratories (UK), for a total period of more than one year. In this time range control room support as MHD expert was given in several experimental sessions, especially focused in advanced scenarios and MHD campaigns.
The technique is based on the observation that the equilibrium perturbation produced by a rotating magnetic island induces a particular pattern in temperature profile oscillations, in such a way that oscillations of magnetic signals are linked to the temperature oscillations inside the plasma [58], and the phase of the coherence between the two oscillations shows a π jump in its radial profile whenever an island is crossed, moving along the plasma radius.

The technique starts from n number analysis of magnetic signals, which assigns an n number to each frequency bin in the spectrogram, and provides a basis to filter out the temperature oscillations not linked to the selected n number perturbation. Then an automatic algorithm for mode tracking in the time-frequency domain is used to follow the frequency evolution for each n mode number, as it can be seen in Figure 3.2. This procedure also gives the absolute amplitude of each mode in the magnetic signal.

A calculation of the coherence amplitude and phase in Fourier space between the magnetic signal and each of the 48 ECE channels is performed using Welch's method; the mode frequency provided by the tracking algorithm is used to calculate coherence just in the FFT frequency bin of the mode, in order to increase signal to noise ratio and to reduce the computing time. The results are shown in Figure 3.3, where the radial profiles of coherence amplitude and phase are shown. The following step in the analysis is to find the radial position of phase jumps for each time slice and for each mode. Particular care is taken to discard low average coherence amplitude temporal frames (C<0.4) and couples of points too far one from each other (δR>10cm).
The last step is to produce a signal describing the mode radius as a function of time. For this aim a tracking algorithm is used, similar to the one used to detect mode frequency in the magnetic signals, which follows in time the maximum value in space-time density of phase jump points. More than one iteration of this process is used to find NTMs position, in this way multiple tracks for each mode can be found, till a maximum number of three. Again particular care is taken to avoid picking up phase jumps due to noise, using a cross check with coherence cross spectrum at the same radius, to find a fluctuation amplitude above the noise level. This software can run in a completely unattended mode.
Figure 3.4 shows the results of the analysis for a typical 3/2 NTM on JET, with detected phase jumps represented by dots with error bars and the tracked mode location over plotted to phase jump points as a black line. Error bars are estimated as half of the distance between the two neighboring channels that enclose the phase jump.
As it can be seen the mode radial position is in reasonable agreement (within 3σ) with the q=3/2 surface position from the equilibrium reconstruction.
The main uncertainty of this technique arises in the determination of the radial positions of ECE channels, which depends on the accuracy of magnetic field profile reconstruction including plasma current and vacuum magnetic field. The latter can give a systematic localization error if it is not well calibrated. This uncertainty is not included in the error bars of Figure 3.4.

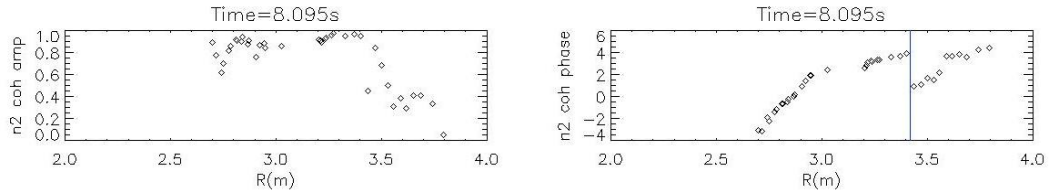

Figure 3.3: *Coherence amplitude (left) and phase (right) radial profiles at the n=2 mode frequency.*

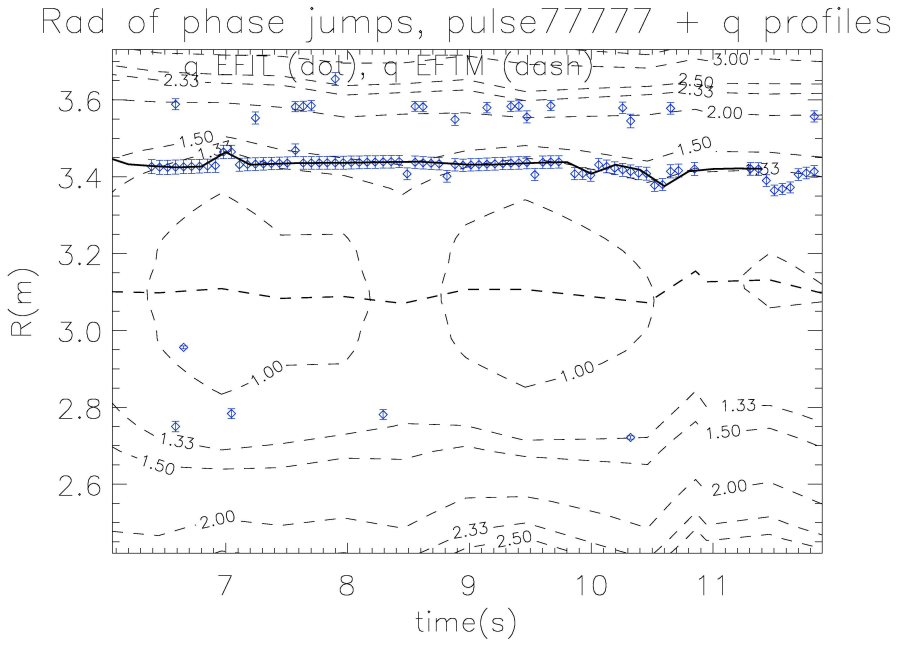

Figure 3.4: *Mode position detected by ECE phase jumps, as a function of time and channels radii for discharge 77777. Blue points correspond to n=2 mode. The error bars are the distances between the two channels that enclose the phase jump. The contour plot of q profile inferred from the EFIT equilibrium reconstruction constrained by MSE, CXS and pressure data, also called EFTM, is over-plotted. The central dashed line is the central axis reconstructed radius as a function of time.*

3.3 Diamagnetic frequency technique

This technique is based on the assumption that magnetic islands propagate, in the frame with zero radial electric field ($\omega = \omega_{E\times B}$), at the ion diamagnetic frequency:

$$\omega_i^* = -\frac{n}{eN}\frac{dP_i}{d\psi} \tag{3.1}$$

with P_i ion pressure, and N ion density.
The frequency in the laboratory frame is then $\omega = \omega_i^* + \omega_{E\times B}$. This assumption is supported by experimental and theoretical studies, in fact $\omega_i^* + \omega_{E\times B}$ corresponds to the right side limit of Figures 2.5 and 2.6, discussed in §2.5.2. The technique is quite recent, and it could take advantage from the validation with other localization methods, and with internal current profiles measurements as well.

$\omega_{E\times B}$ is given by the radial momentum balance of carbon impurity; neglecting poloidal rotation and density gradient it is expressed as

$$\omega_{E\times B} = n\Omega_t - \frac{n}{6}\frac{dT_c}{d\psi} \tag{3.2}$$

with carbon temperature T_c and carbon toroidal rotation Ω_t as measured by Charge Exchange Spectroscopy. Assuming $T_i = T_c$ and neglecting the density

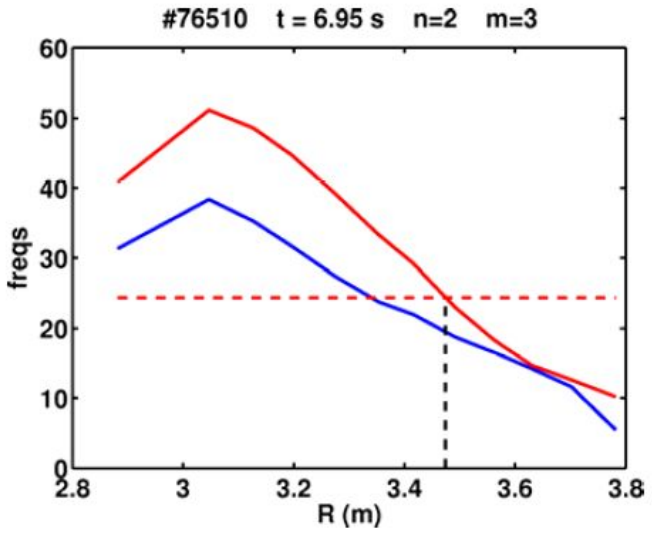

Figure 3.5: *$\omega_{E\times B}$ (blue) and $\omega_i^* + \omega_{E\times B}$ (red). The horizontal line shows measured mode frequency. The vertical bar shows the resulting mode location.*

gradient in ω_i^*, the island frequency in the laboratory frame becomes

$$\omega = n\Omega_t - \frac{5n}{6}\frac{dT_c}{d\psi} \tag{3.3}$$

ω is therefore a function of ψ, which can be translated into the minor radius with the appropriate mapping. Matching the radial profile of equation 3.3 with the mode frequency measured by fast magnetic coils gives the island location $R_{m,n}$, as shown in Figure 3.5, where the calculated frequency profiles are compared to the measured mode frequency.

Several spectral lines can be followed in time in the mode spectrogram, as shown in Figure 3.6. A location signal is generated for each line by tracking the local spectral maximum as it is done in Section 3.2.

Measurement errors usually depend on fluctuations in Charge Exchange data (mainly due to ELMs). Others errors might arise from the assumptions made in order to get a robust calculation of equation 3.3: neglecting density gradient, neglecting poloidal rotation term and assuming that carbon temperature and rotation profiles are the same as deuterium ones. The first assumption can be removed with a more refined analysis, given a reliable density measurement. The second assumption can also be removed having good poloidal rotation data, even though the correction is thought to be negligible compared with the toroidal rotation term [15]. Future work will concentrate on the implementation of these two aspects.

Another possibility is to use ψ from a constrained equilibrium reconstruction, which have been built recursively using the resonant q radial positions given by modes as constraints. This procedure have been tried with positive results, as will be shown in the next section.

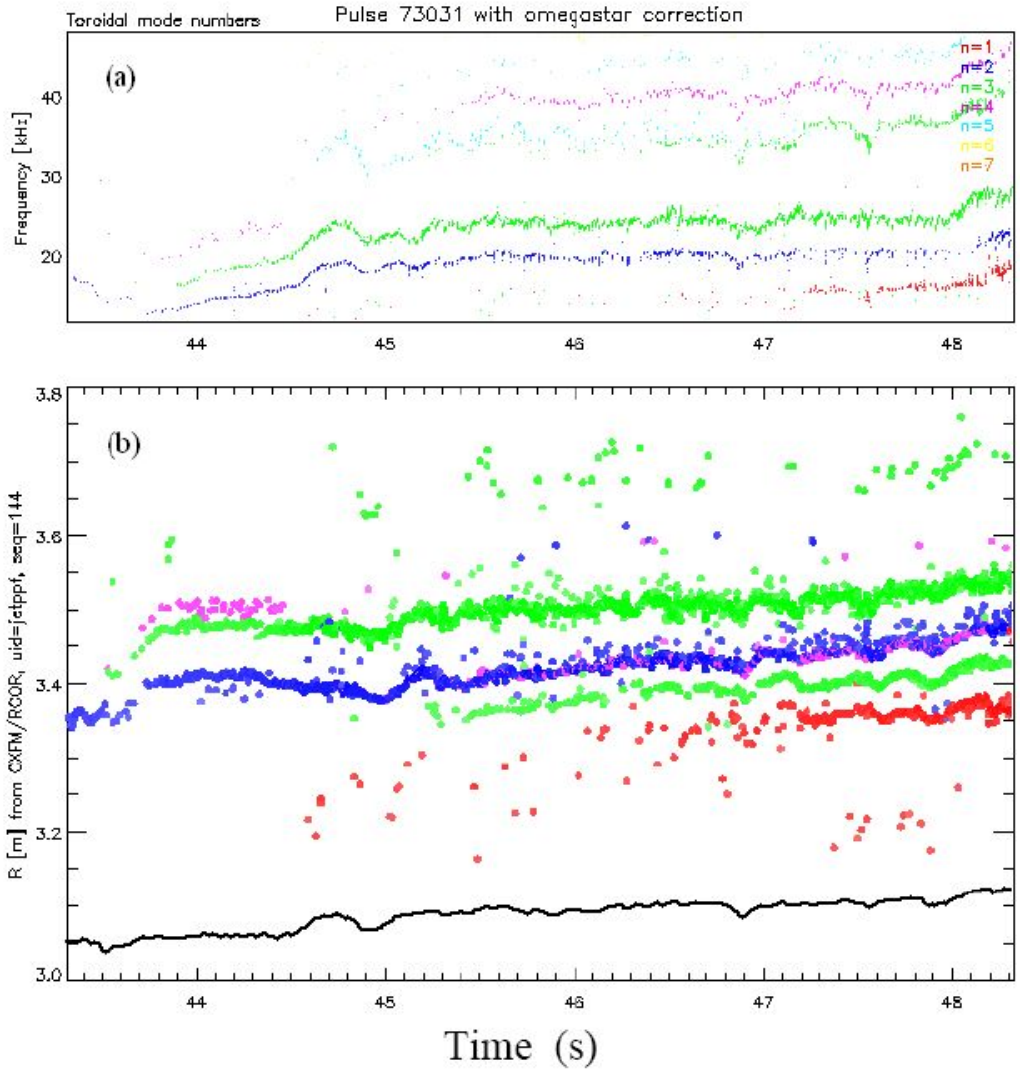

Figure 3.6: *Upper frame: spectrogram of magnetic signals, with toroidal number shown in color code. Lower frame: Mode locations for m/n=1/1 (red), 4/3 (inner green), 3/2 (blue), 5/3 (outer green). The discharge begins at 40s.*

3.4 Localization benchmark and comparison with current profiles

To benchmark the different localization techniques and compare the results with current profiles measurements, an extensive NTM (the most usual tearing instability in Advanced Scenarios) database at JET was built, including almost 200 events. The selected NTMs were localized when the mode was already large enough to be detected in the magnetic signal, and the internal displacement was large enough to have good coherence with fluctuations in the magnetic signal for the ECE localization technique. It can be therefore assumed that the island width should be already saturated, and the island rotation dynamics should fall into the sonic regime (effective flattening of density profile inside the island) of reference [21], and the mode rotation frequency should be $\omega_i^* + \omega_{E\times B}$.

Figure 3.7 shows a comparison between radial locations from frequency and ECE methods, for n=1, 2, 3 mode numbers. On average, mode locations from ECE are 9cm more internal than the ones from mode frequency (The comparison is carried out for low field side data). It is interesting to notice that the shift is not constant for all of the data points, and the data spread is similar for 2/1 and 3/2 NTMs, while it is somewhat smaller for 4/3 NTMs.
Figure 3.8 shows a comparison between locations from ω_i^* technique and from MSE diagnostic. In this case there is agreement on average, but still with significant spread, in particular at low R_{MSE}. The black star shows the effect of applying to the most discrepant point (connected by the black curve) a recursive correction for ψ and an improved fit to the temperature gradient. Still a significant discrepancy remains for this single point, which has to do either with errors in the MSE q-profile, or to the previously listed effects neglected in mode analysis. Figure 3.9 shows that a large discrepancy arises if ion diamagnetic drift is completely ignored, this is a confirmation that ω_i^* correction gives a better accuracy in the determination of mode radial position, even using the mentioned assumptions.
In summary, comparison between MSE and ω_i^* data shows that the assumption of mode rotation at the ion diamagnetic frequency is substantially correct, even though a large data spread remains. A systematic discrepancy with ECE data is found, that could be due to an error in the total magnetic field calculation, which is very important for the localization of the source of ECE radiation. This discrepancy is also highlighted in the comparison of ECE temperature profiles at JET with regard to electron temperature profiles measured with other diagnostics, and in the comparison of Low Field Side with High Field Side ECE profiles as well, as it is shown in reference [59].

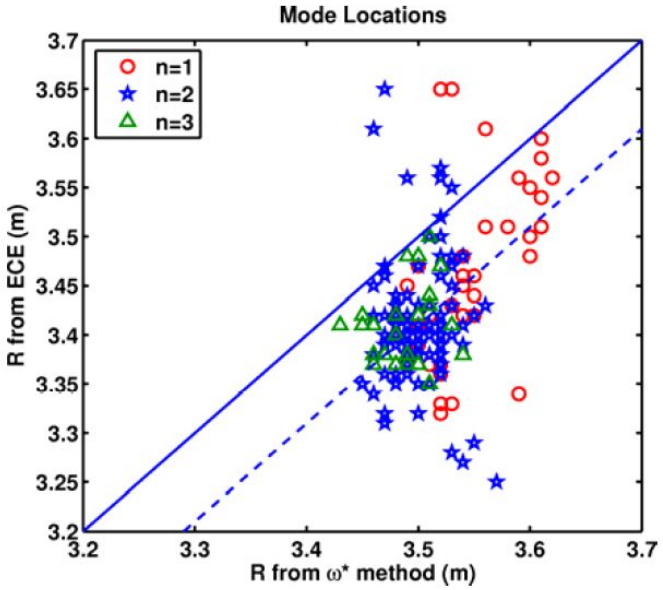

Figure 3.7: *Comparison between locations from ω_i^* technique and from ECE oscillations for m/n=2/1, 3/2 and 4/3 modes. Identity corresponds to the blue solid line. The dashed line is shifted by 9 cm.*

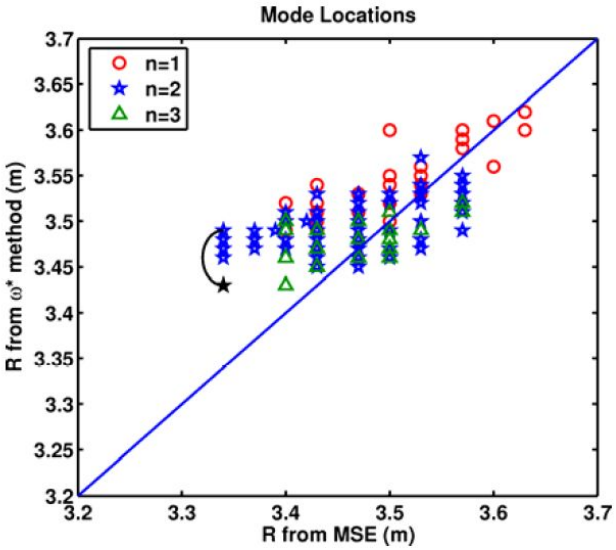

Figure 3.8: *Comparison between rational q locations from ω_i^* technique and from MSE diagnostic for m/n= 2/1, 3/2 and 4/3. Identity corresponds to the blue solid line.*

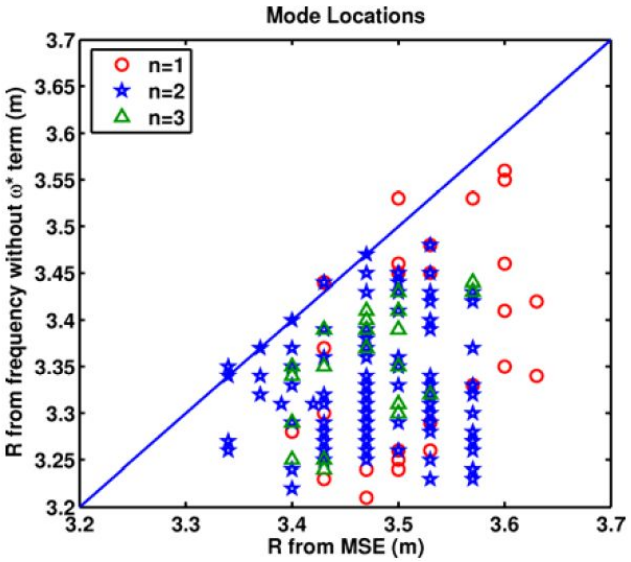

Figure 3.9: *Comparison between rational q locations from mode frequency without ion diamagnetic drift and from MSE diagnostic. Identity corresponds to the blue solid line.*

The agreement between ECE localization and ω_i^* localization could be improved with a $2-3\%$ correction to the total equilibrium magnetic field, which is larger than the toroidal field calibration error of 1% in JET, even though the origin of the discrepancy might not be due to just one of the techniques, but to both of the techniques errors.

CHAPTER 4

NTM magnetic spectrum and magnetic coupling on JET

In this Chapter the problem of the determination of the NTM spatial structure will be faced, in particular focus will be put on the composition of the poloidal m number spectrum.
Toroidal curvature and poloidal shaping effects introduce sidebands of the main m component that can interact among each other and with the plasma (as shown in Chapter 8 as well), especially in high β plasmas with a highly elliptic and triangular shape.
Clearly these sidebands, having different m numbers from the main one, might resonate inside the plasma at different radial positions: for example an $m = 2$ mode with $n = 1$ toroidal mode number has toroidicity-induced sidebands, whose phase fronts match field line winding where $q = (m + 1)/n = 1$ and $q = (m - 1)/n = 1$ [58, 60].
Sidebands might then cause forced magnetic reconnection on different resonant surfaces, giving rise to secondary magnetic islands, that in turn could degrade the plasma confinement properties. A particular care will be given in treating this point, to verify whether this is the case for the JET tokamak.

4.1 Experimental evidences of n=1 NTMs

In this section the outputs of the technique described in Section 3.2 will be exposed for two different pulses, following the logical order of the various analysis steps, with a final link to rotation data analysis.
The first example of the use of the method is shown for JET pulse 77590, which is characterized by a 2.1MA plasma current, a 1.75T toroidal field, β_N=2.2, and an Advanced Tokamak scenario with a high triangularity configuration and a total heating power of approximately 30MW, subdivided in 20MW of Neutral Beam Injection power (NBI), 7MW of Ion Cyclotron Resonance Heating (ICRH) and 2.5MW of Lower Hybrid wave heating (LH) [61]. External input power and β_N traces are shown in Figure 4.1 upper and mid plot.

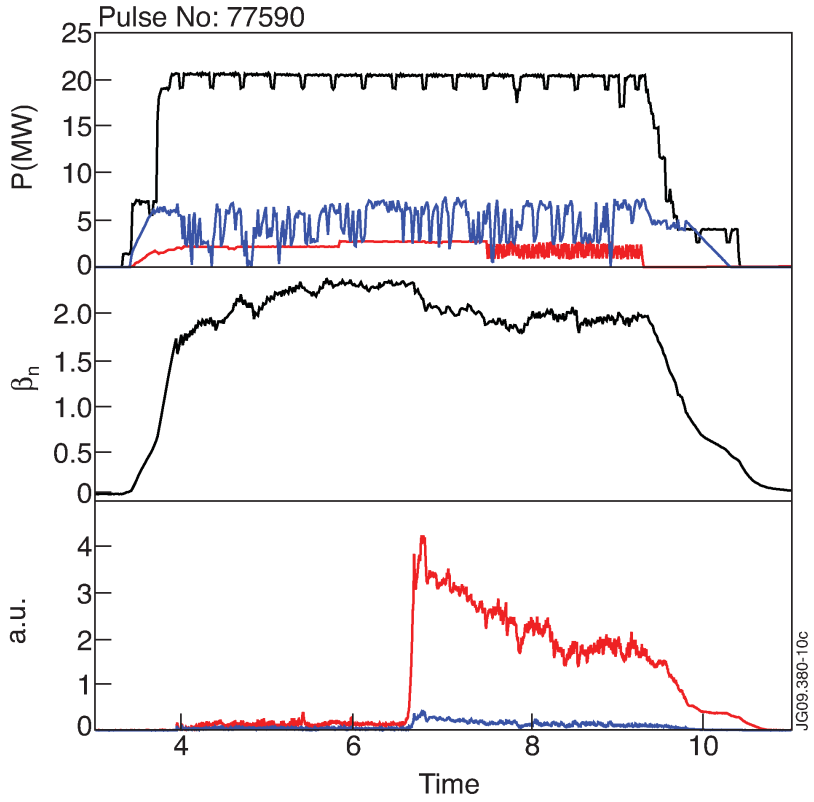

Figure 4.1: *In the upper box the amount of NBI input power (black), ICRH (blue), LH (red) are shown for pulse 77590. In the central box β_N evolution is shown and in the lower box the odd n (red) and even n (blue) integrated magnetic amplitudes are shown.*

This is one of the Advanced Tokamak configurations developed at JET in the last years, where a considerable effort has been made for the tailoring of the magnetic q profile, to achieve a rather flat q in the center of the plasma, with the minimum value of q around 2.
Despite the aim of the tailoring effort was to obtain a higher MHD stability, MHD events still happens in this type of scenario, also given the natural evolution of the q profile towards its relaxed state, and they can have very detrimental effects on plasma global confinement. In Figure 4.1, where the integrated n=1 (red) and n=2 (blue) magnetic signals from tangential pick up coils are shown in the bottom plot, it is clear that the peak in n=1 activity around 6.5s is then reflected on a drop in β_N from 2.3 to 1.8, which is in turn an evidence for a considerable drop in confinement, given the constant input power coupled to the plasma.
From the magnetic spectrogram (Figure 4.2) the presence of two NTMs during the heating phase is highlighted. In fact an early NTM appears at 4.2s and is identified by the green n=3 track, then a larger 2/1 NTM (in red) appears at 6.5s and remains in the plasma for the rest of the heating phase.
In Figure 4.3 a contour plot is shown of the cross amplitude between each ECE channel and a single magnetic coil at the frequency of the mode magnetic fluctu-

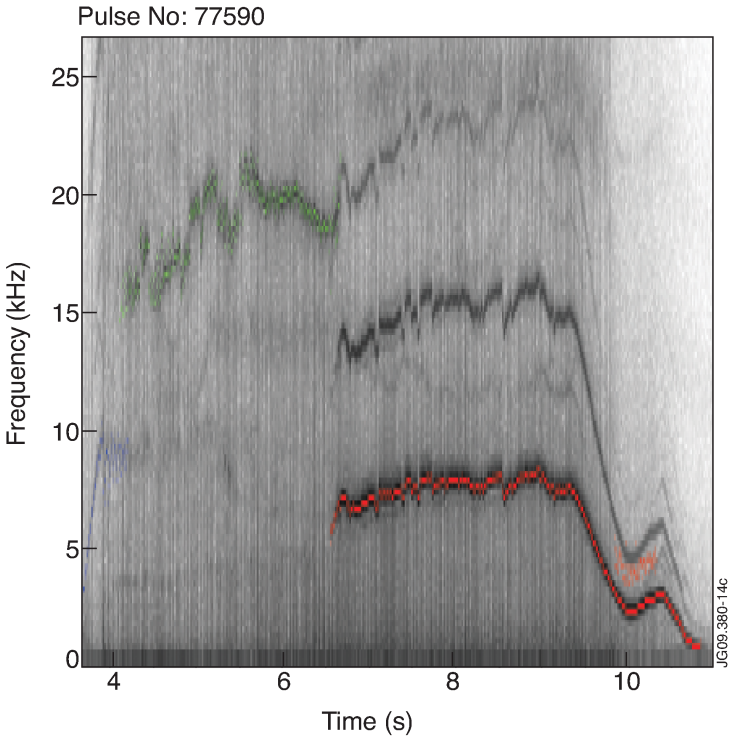

Figure 4.2: *Spectrogram from a 1MHz bandwidth pick up coil for discharge 77590. The different coloured tracks are the output of the mode tracking algorithm. Red tracks are linked to n=1 activity, blue tracks to n=2 activity and green tracks to n=3 activity.*

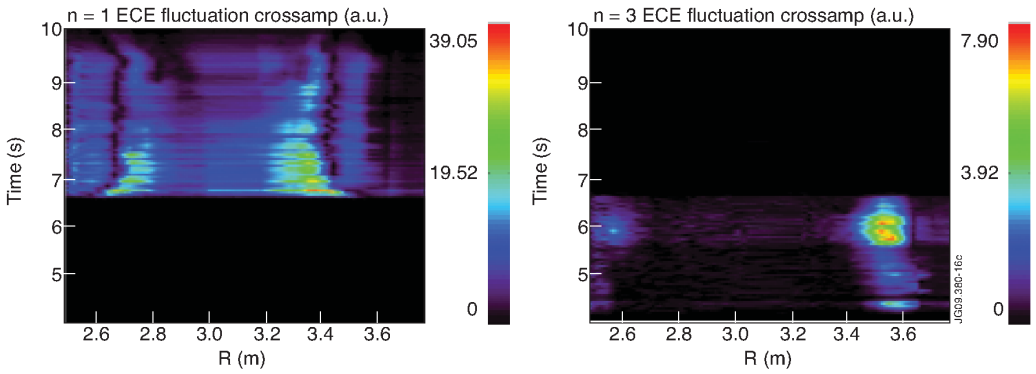

Figure 4.3: *Contour plot of fluctuation cross-amplitude between magnetic a signal and all ECE channels, as a function of channel position and time at the frequency of the mode, for n=1 and n=3 modes respectively, for pulse 77590.*

ation. The plot displays two high fluctuation amplitude traces at the high field side at 2.7m and at the low field side at 3.4m, that are due to the same magnetic surface crossing twice the ECE line of sight. Moving towards a larger radius, a contrast with a dark zone can be observed, followed by another bright zone with high fluctuation amplitude. This typical structure gives us preliminary informa-

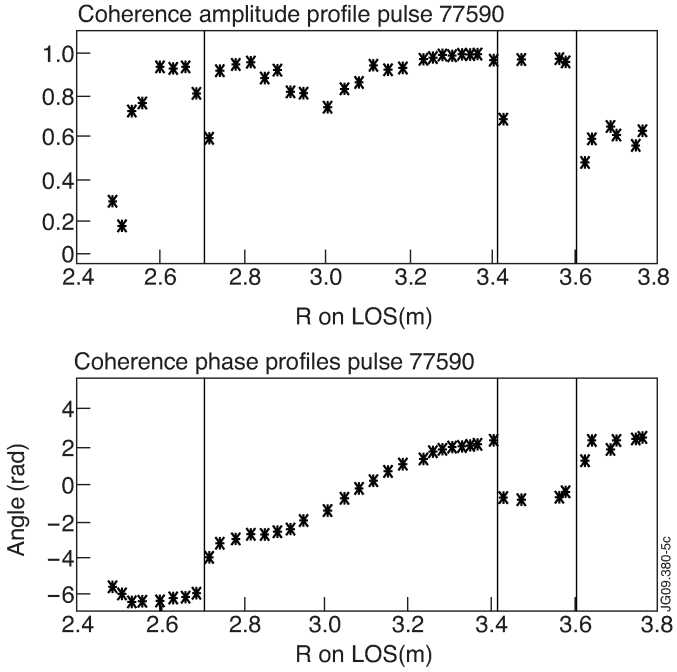

Figure 4.4: *Coherence amplitude and phase radial profile for an n=1 NTM in pulse 77590 at t=8s. Solid lines are in the positions of detected jump radii.*

tion on the island position, since the displacement of magnetic surfaces should be anti-symmetric from one side to the other of the resonant surface where the island is located [62], for this reason we expect to find the fluctuation phase jump right at the position of the dark surface.
In Figure 4.4 typical coherence amplitude and phase profiles are shown for a 2/1 NTM, the vertical lines are the detected phase jumps. It can be seen already that more than one phase jumps can be observed in the low field side.
In Figure 4.5 the location of phase jump detected by the algorithm is shown as a function of time, and a contour plot of magnetic q profile has been over laid for reference. The q profile displayed is inferred from the EFIT equilibrium code reconstruction constrained by Motional Stark Effect (MSE), polarimetry, and pressure profiles data. ECE radii are also calculated using the reconstructed equilibrium magnetic field. In the plot the main n=1 NTM is localized in both the high field side at 2.7m and the low field side at 3.4m is visible. The uncertainty on mode position is about 0.031m, that is the average distance between the two neighbouring channels that enclose the phase jump.
A secondary track is also present at the LFS and partially at the HFS, it is localized around the q=3 surface; a similar experimental behaviour is reported in [63].
An m number analysis from magnetic coils at different poloidal angles was performed during the transition time interval between n=3 mode to n=1, the result is shown in Figure 4.6. Considering these measurements it is important to bear in mind that this kind of calculation has always been difficult in JET, in fact poloidal asymmetries in the pick up coils position lead to the systematic overestimation of the m number, compared to other m deduction methods [64, 65, 66].

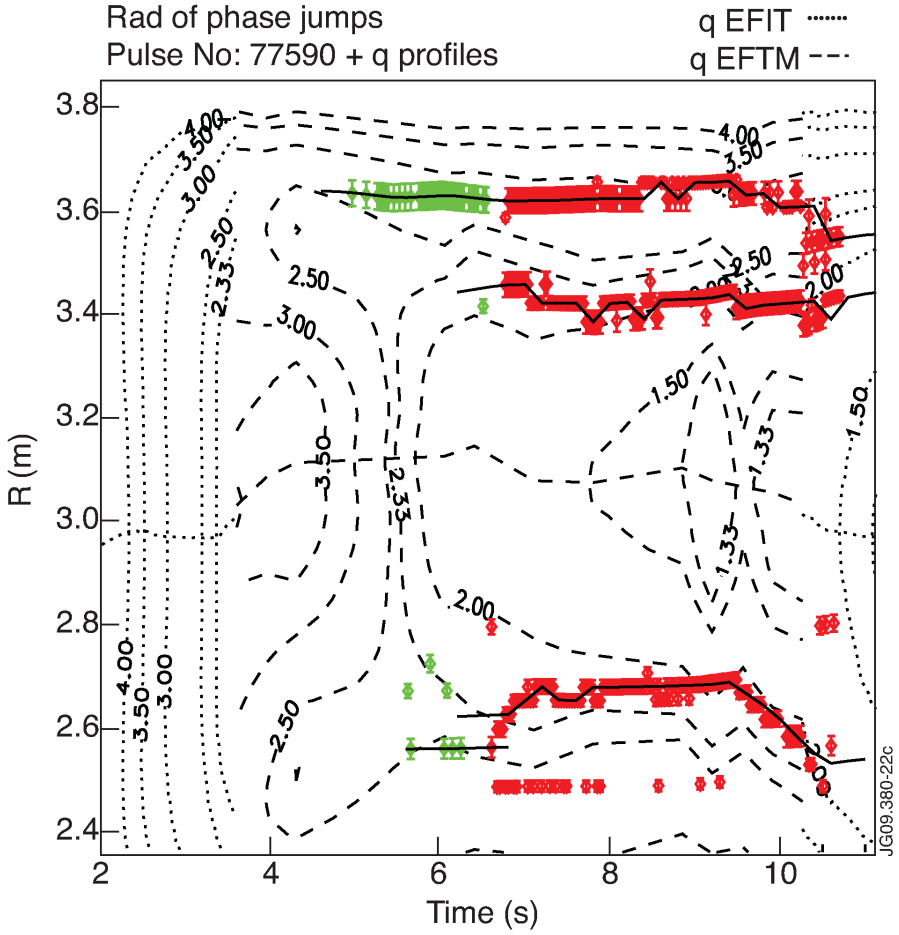

Figure 4.5: *Mode position detected by ECE phase jumps, as a function of time and channels radii for discharge 77590. Red points are due to n=1 mode and green points to n=3 mode. The error bars are the distances between the two channels that enclose the radius of phase jump. The contour plot of q profile inferred from EFTM is over-plotted. The central dotted and dashed line is the central axis reconstructed radius as a function of time.*

The calculated m for the n=3 NTM is around 9, and the best fitted m for the n=1 NTM is around the value of 2.5, after a short phase of m=3, while both the modes are present. This result, taken within the uncertainties described above, can give some hints about the observed physics. In fact the m analysis for the n=1 NTM gives a mode which is neither a pure m=2 nor a pure m=3 harmonic, but could be a superposition of both the two harmonics, and in the following section we will give other arguments in support to this statement.
To understand the meaning of the more external track around 3.6m, let's call it second track from now on, an interesting piece of information comes from the profile of plasma toroidal rotation frequency.
The picture could be then completed using the information contained in Figure 4.7, in which the temporal evolution of toroidal rotation radial profile, measured

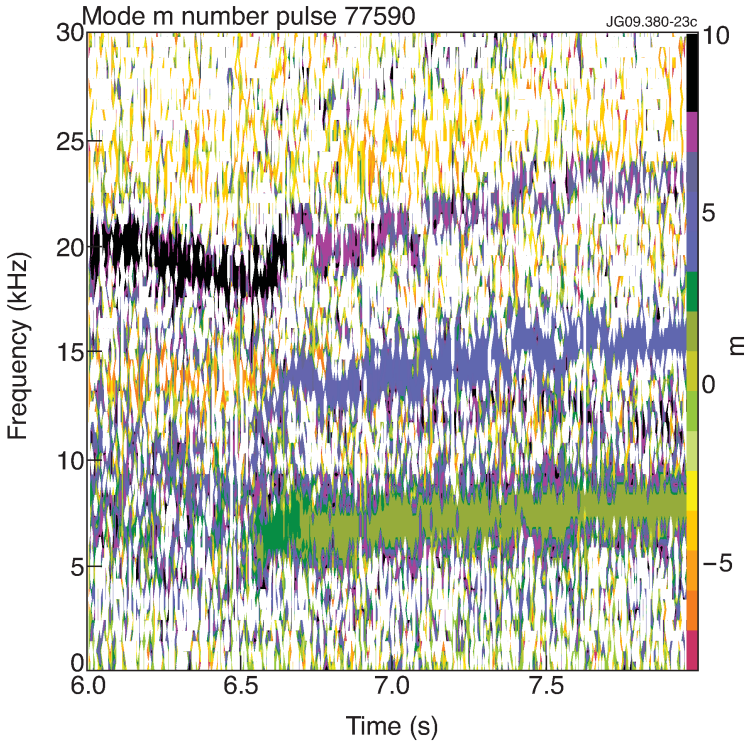

Figure 4.6: *m number analysis from HFS 1MHz bandwidth pick up coils for pulse 77590.*

with Charge Exchange Spectroscopy (CXS), is shown. The first part of the heating phase exhibits a monotonic rotation profile from the plasma edge to the core. At 5.55s the doubling of n=3 NTM amplitude is followed by a modification of the rotational shear, with the creation of a low shear region between 3.4m and 3.5m in major radius. The rotation flattening in this zone, which therefore appears to be linked to the n=3 NTM, has the effect of modifying the rotation profile to the boundary conditions that favour further MHD onset. In the third part of the heating phase, from 6.6s on, the discharge is seriously affected by the onset of the large 2/1 NTM, with a significant drop in confinement.

A larger effect on toroidal rotation is observed as well, in fact a zone with zero or even weakly negative rotational shear is created, with an off axis rotation minimum around 3.36 m, in agreement with the position of the main track of the 2/1 NTM. The difference between black line and red line is very close to uncertainty of the measurement (5%), so, even if the relative behaviour of different radial measurements is clear, further investigations to confirm the actual magnitude of negative rotational shear are needed.

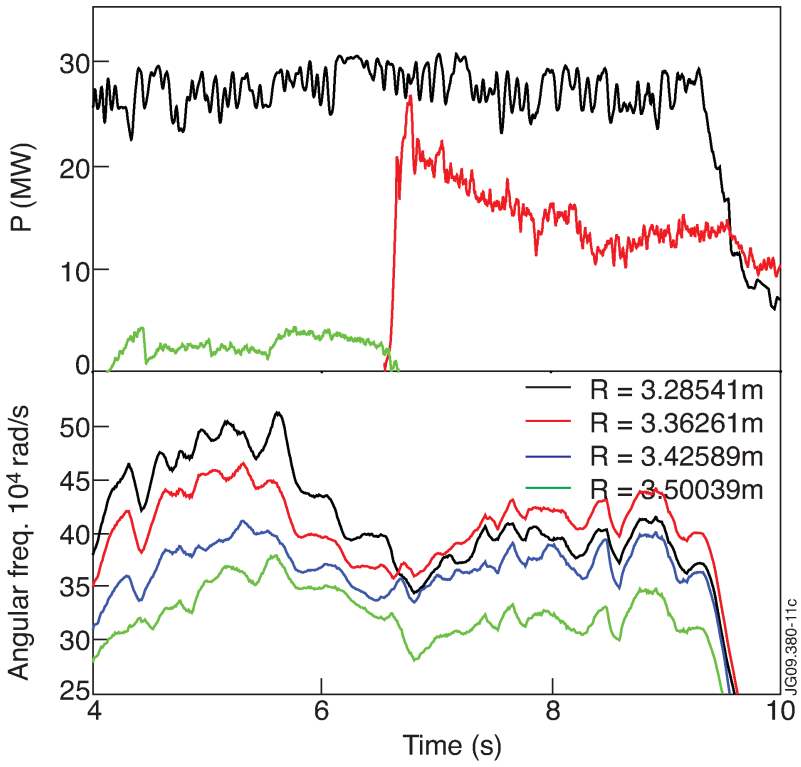

Figure 4.7: *In the upper plot the total input power coupled to the plasma is plotted in black for discharge 77590, n=3 (green) and n=1 (red) magnetic amplitudes are over plotted (a.u.). In the lower plot toroidal rotation evolution from Charge exchange spectroscopy is plotted for different radial positions in the plasma.*

4.2 Experimental evidence of n=2 NTMs

In this section the n=2 mode will be considered, which is typically weaker than the n=1 mode but occurs more frequently. As an example, the analysis of pulse 76893 will be presented, which is characterized by a 1.3 MA plasma current, a 1.7T toroidal field, β_N=3, and an hybrid scenario with a high triangularity configuration and an external input power of approximately 12 MW of neutral beam, the input power and β_N traces are shown in Figure 4.8 upper and mid plot.
This scenario has a flat q profile in the plasma core, with a minimum value of q around 1, for this reason it is prone to q=1 fishbone and sawtooth activity, and it is frequently affected by 3/2 and 4/3 NTMs as well. While fishbones are not dangerous for plasma global confinement, NTMs can indeed spoil plasma performances, as shown in Figure 4.8, where the increase in n=2 signal amplitude at 6.2s (lower plot) is coincident with a large decrease in β_N (mid plot), despite the input power is raised (upper plot).

From the magnetic spectrogram in Figure 4.9 q=1 activity is present at 13-14 kHz from 4.4s on, but it is not recognized by the tracking algorithm as a continuous mode, and it is then discarded (only the first longer sawteeth periods are kept). The frequency of this activity is suddenly reduced to 7-8 kHz after the onset of a

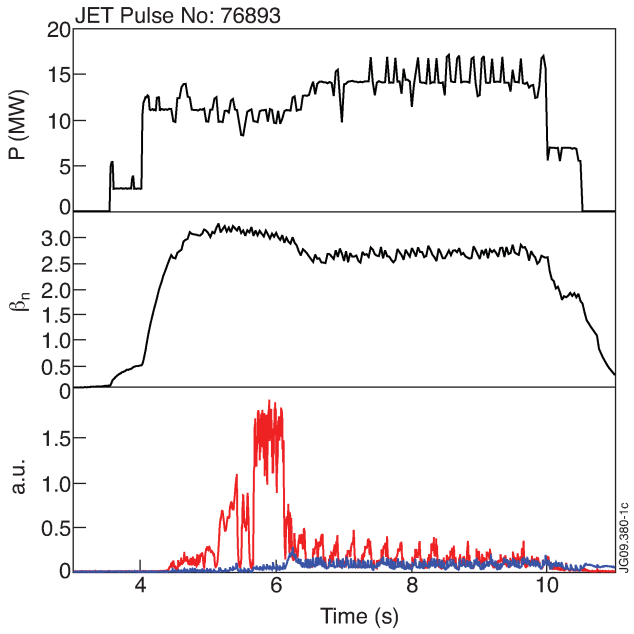

Figure 4.8: *In the upper box the amount of NBI input power (black) is shown for pulse 76893. In the central box β_N evolution is shown and in the third box the odd n (red) and even n (blue) integrated magnetic amplitudes are shown.*

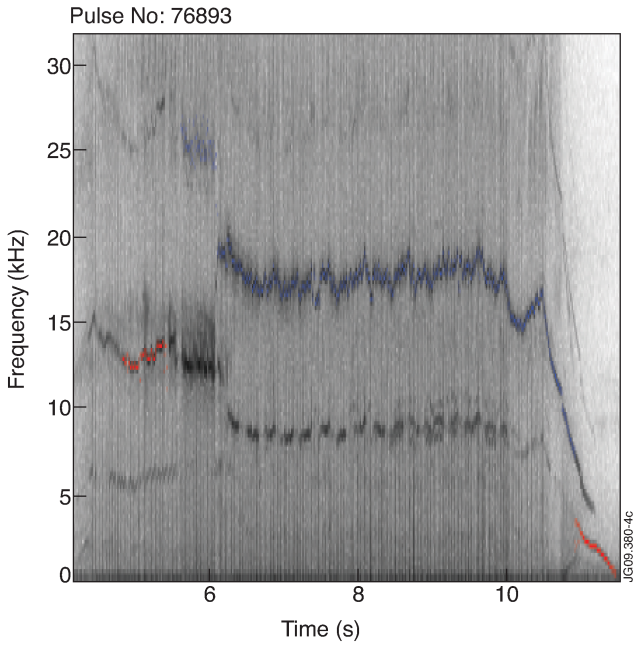

Figure 4.9: *Magnetic spectrogram from a 1MHz bandwidth pick up coil for discharge 76893. Red tracks are linked to n=1 activity and blue tracks to n=2 activity. The mode at 9 kHz is not recognized as a continuous mode by the tracking algorithm, and then discarded*

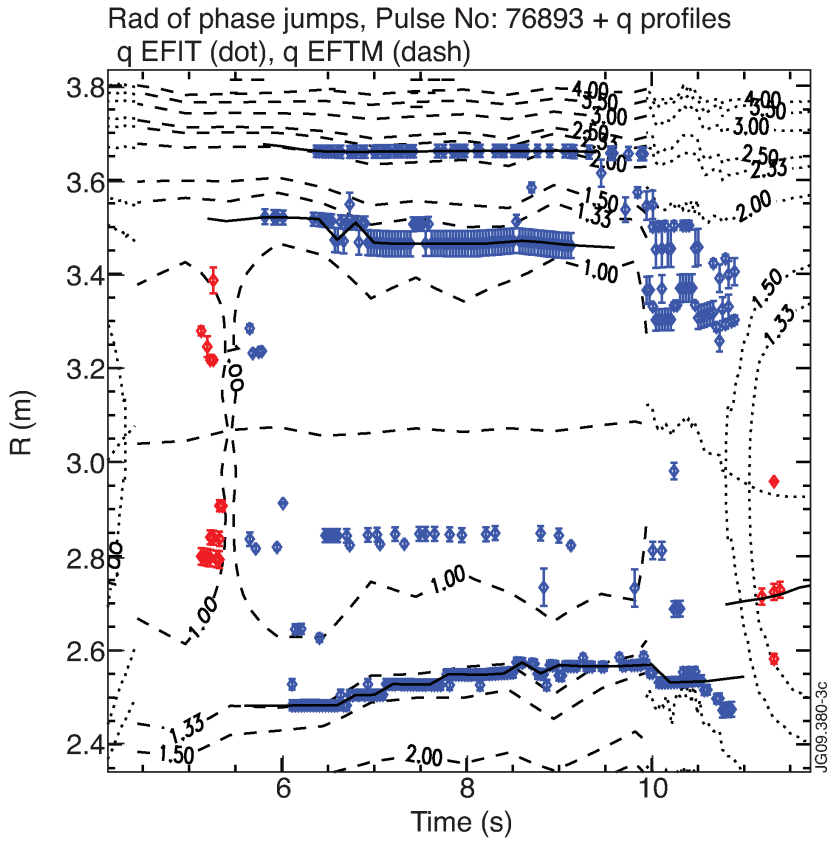

Figure 4.10: *Mode position detected by ECE phase jumps, as a function of time and channels radii for discharge 76893. Red points are due to n=1 mode and blue points to n=2 mode. The error bars are the distances between the two channels that enclose the radius of phase jump. The contour plot of q profile inferred from EFTM is over-plotted. The central dashed line is the central axis reconstructed radius as a function of time.*

n=2 NTM at 6.2s, which lasts till the end of the heating phase.
The mode radial localization can be seen in Figure 4.10, in which two main tracks can be seen around 2.5m and 3.45m, in good agreement with the position of q=1.5 surface within the error bars of the ECE channels position. Another n=2 track in the LFS can be seen in this case as well, around 3.7m, and it appears from the beginning of the n=2 NTM life. The n=1 quasi-continuous activity can be localized as well at 2.8m and 3.25m, but only in the first part, when no NTMs were present. On the other hand during the NTM phase some sporadic n=2 points are detected at the same position of previous q=1 activity, this could be due to the coupling of q=1 activity with the n=2 NTM (the latter has exactly twice the frequency of the former) observed in the spectrogram.
For this pulse the rotation profile behaviour has been studied as well, and again a clear correlation between n=2 mode onset and a sudden decrease of toroidal rotation frequency is observed, as can be seen in Figure 4.11, where the rotation frequency evolution as a function of time is shown for four different CXS channels.

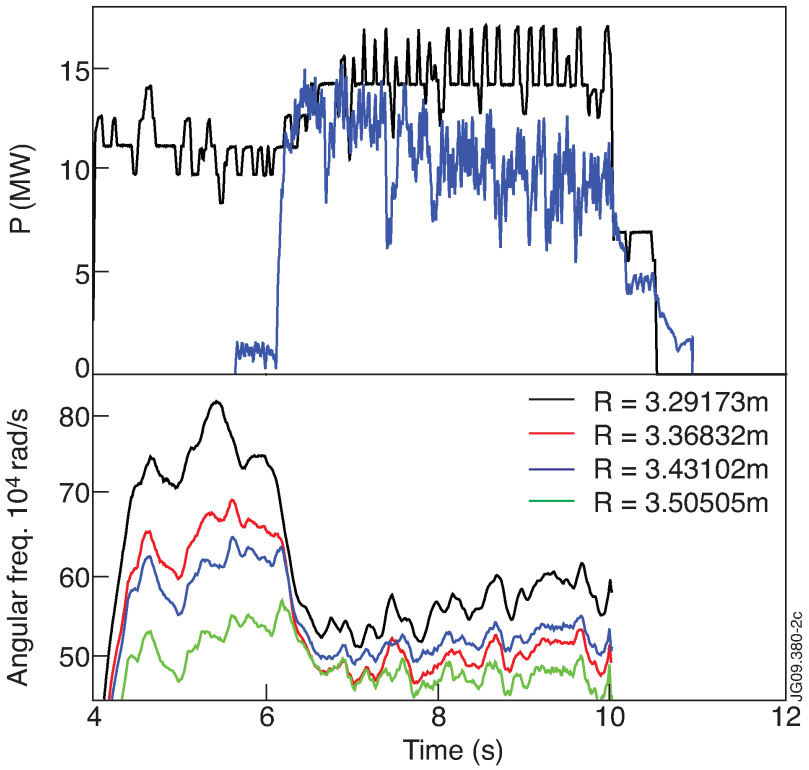

Figure 4.11: *In the upper plot the total input power coupled to the plasma is plotted in black for discharge 76893, and n=2 (blue) magnetic amplitude is over plotted (a.u.). In the lower plot toroidal rotation evolution from Charge Exchange Spectroscopy is plotted for different radial positions in the plasma.*

But the action of the mode on rotation is more complex than an overall damping of the whole profile, in fact again a localized damping at 3.37m is experienced (red line in Figure 4.11), which creates again a non monotonic rotation profile.
In this case the distance of the local rotation minimum from the mode position is about 10cm, and the distance from reconstructed q=1.5 surface is about 15 cm.

4.3 ECE oscillation profile modelling

In this section a simple modelling of the ECE fluctuation due to the NTM will be presented. The modelled profiles will be used as input in the localization code, with the aim of finding the profile that fits best the experimental coherence profile.
The shown experimental evidences are a relatively common feature observed in JET advanced scenarios discharges, particularly regarding the ECE and magnetic coils data. The related effects on toroidal rotation are less clear at the present state of the analysis, rotation features may change from pulse to pulse and they have not the same magnitude in different pulses. The aim of this analysis is to explain the experimental evidences for the two examples presented, while a sys-

tematic work of characterization of the evidences for the complete JET advanced scenarios database is still being carried out.
The experimental observations of the second external phase jump in the low field side, which were possible thanks to the newly implemented coherence tool, require a physical explanation which has to be compatible with the plasma rotation behaviour as well. In this section some possible explanations will be proposed, and their consistency with ECE radial profile and toroidal rotation data will be verified.
Once checked for a high coherence level in correspondence to the secondary jump, one of the possible explanations is a one to one correspondence between coherence phase jumps and magnetic islands, in other words, this statement would imply the presence of a secondary magnetic islands chain in the plasma. This idea is sensible, since the presence of the main m=2 island resonant on q=2 surface produces an m=2+1 resonant sideband field that might cause forced magnetic reconnection on the q=3 resonant surface. Accordingly to [58, 62] this could happen only if the difference in toroidal rotation frequency between the two surfaces is small enough, and the secondary island should be born phase locked to the main one, in other words it should have zero toroidal rotation in the reference frame of the moving main mode.
On the other hand the double island structure gives rise to a slightly complicated picture, and it is certainly worth looking for the existence of a simpler idea that could satisfy the experimental observation as well. Let's then consider a double mode structure, similar to the one considered so far, but with the only difference that the m=2+1 sideband has a simple kink structure without any magnetic island. It would be interesting to check if such a mode structure, simpler than the double island one, is still able to reproduce a coherence phase as the one which is observed experimentally in the data previously shown.
To make this test an ECE fluctuation signal with the desired radial profile was built artificially, and it was used as an input to the analysis coherence algorithm, to check if the output was similar to the real measured phase profile. In this process a large advantage was taken from the fact that ECE radiometer line of sight is slightly off-axis, in fact this means that the poloidal angle ϑ is also varying along the line of sight, and then the phase profile changes along the major radius with a dependence of the form $m\vartheta(r)$ with r the radial coordinate along the ECE line of sight. Then knowing $\vartheta(r)$ from the previously used magnetic equilibrium reconstruction, and given the slope of the measured phase profile, we can extract information about the m number of the modes.
The ECE profiles used as first guess to reproduce the measured phase were the sum of two different profiles, the main one which had an oscillation profile of the form:

$$A_1(R)e^{-\phi_1(R)} \tag{4.1}$$

with

$$A_1(R) = A_1\left(e^{-\frac{(R-c_{11})^2)}{2w_1^2}} + e^{-\frac{(R-c_{12})^2)}{2w_1^2}}\right) \tag{4.2}$$

$$\phi_1(R) = \phi_1 + m_1\vartheta(R) + J_1(R) \tag{4.3}$$

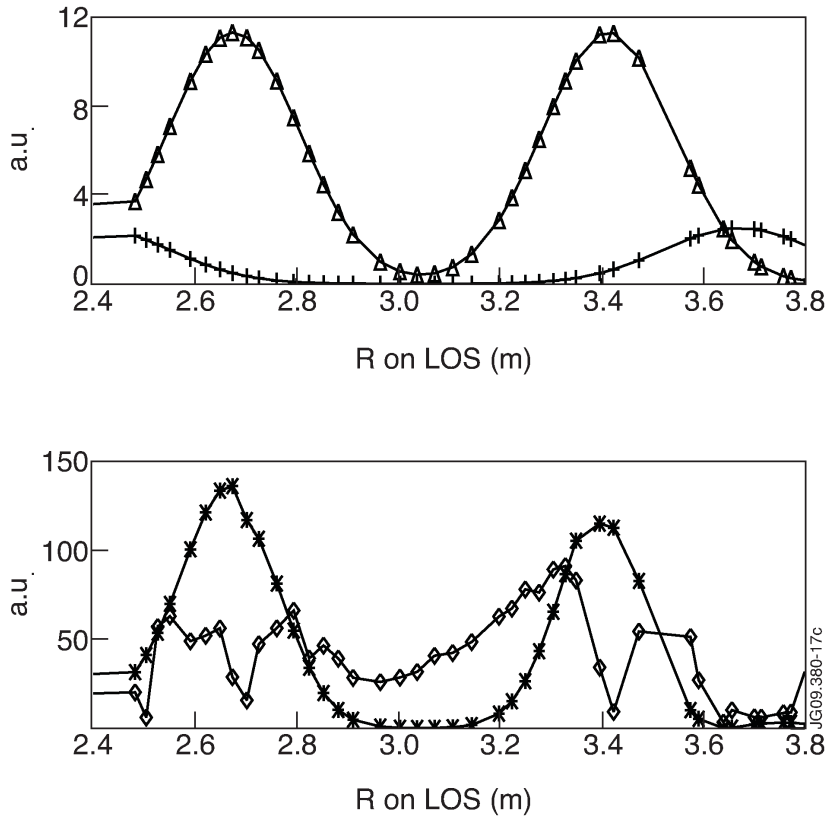

Figure 4.12: *In the upper plot the radial oscillation amplitude profile is shown for pulse 77590 at t=8s, reconstructed with fitted parameters. The amplitude profile for m=2 component is shown as triangles, while for the m=3 component as plus signs. In the bottom plot the total reconstructed amplitude (stars) is compared to the measured one (diamonds). The radii values are along ECE line of sight.*

where the poloidal angle ϑ has a radial dependence

$$\vartheta(R) = atan\left(\frac{(R - X_0)}{Z_0}\right) \tag{4.4}$$

R is the radial coordinate along the line of sight, X_0 is the radial position of the central axis and Z_0 is the vertical distance from ECE line of sight to plasma central plane.

The modelled amplitude profile has a double Gaussian shape, initially centred on the two radial points in which the line of sight (LOS) crosses the q=2 surface (c_{11} and c_{12}) , and with a width w_1 (Figure 4.12, upper plot). This double Gaussian shape was chosen to give a good support to very localized modes, as NTMs can sometimes be, keeping still the possibility to fit well a rather broad profile.

The phase profile is composed instead by an initial phase value ϕ_1, plus a phase variation related to the radial variation of the poloidal angle and to the mode m number m_1=2. Then, since the mode is expected to have a tearing characteristic, a phase jump term J_1 was added which simulates the tearing behaviour, i.e. adds a π jump in the positions c_{11} and c_{12} where the main mode is localized.

For the secondary mode more than one shape for phase profiles have been tested, both with tearing behaviour or with kink behaviour, and amplitude profiles similar to the main mode ones, but centred at different radii and with different m number values. The equations for a non tearing secondary component are:

$$A_2(R)e^{-\phi_2(R)} \tag{4.5}$$

with

$$A_2(R) = A_2\left(e^{-\frac{(R-c_{21})^2)}{2w_2^2}} + e^{-\frac{(R-c_{22})^2)}{2w_2^2}}\right) \tag{4.6}$$

$$\phi_2(R) = \phi_2 + m_2\vartheta(R) \tag{4.7}$$

To determine the best value of the initial parameters for the reconstructed profile, a non linear least squares multi-parameter fit has been used on the experimental phase profiles, using the coherence amplitude profile as weighting factors. The parameters A_1 and A_2 are useful to judge the relative amplitudes of the two mode components, ϕ_1 and ϕ_2 give information on the relative modes phases (both A_1, A_2 and ϕ_1, ϕ_2 are not independent fitting parameters). The parameters c_{11} - c_{22} should identify the position where mode's resonant surface crosses the ECE line of sight and w_1, w_2 express the radial extent (half maximum width) of mode's temperature fluctuation.
An example of fit output is given Figure 4.13, where the best fitting results are shown. The experimental phase profile is reproduced at best with the m=2 tearing plus m=3 kink configuration, given a particular relation between the initial phases of the two different modes, and given a zone outside the main resonant component in which the fluctuation amplitude of the sideband is considerably larger than the amplitude of the main mode.
The best fitted values for the fitting parameters are listed in Table 4.1:

Table 4.1: *Fitting parameters.*

A1 (a.u.)	A2(a.u.)	ϕ_1 (rad)	ϕ_2 (rad)
11.2867±0.117	2.4967±0.026	-0.520±0.015	5.029±0.020
c_{11} (m)	c_{12} (m)	c_{21} (m)	c_{22}
2.676±0.051	3.414±0.001	2.400±0.065	3.672±0.007
w_1 (m)	w_2 (m)	m_1	m_2
0.150±0.027	0.129±0.004	2.258±0.013	3.107±0.015

In this case the minimization has been performed only on the coherence phase radial profile, but the consistency of the process can be checked comparing the simulated fluctuation amplitude with the ECE fluctuation amplitude measured at mode's frequency (Figure 4.12, lower plot). The simulated overall amplitude is similar to the experimental one, although it seems to have a simpler behaviour,

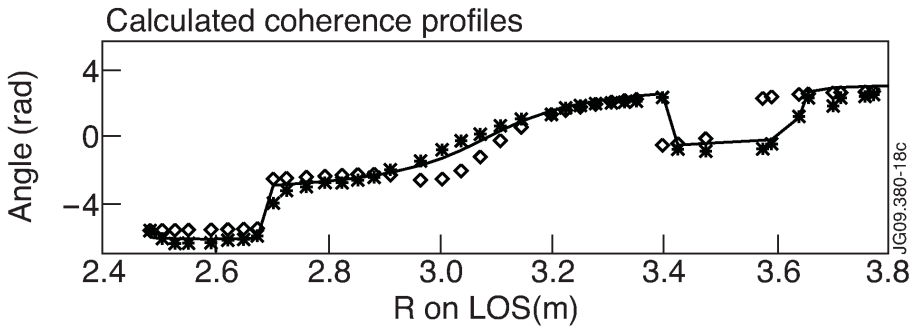

Figure 4.13: *In this figure the phase profile built using initial guess values is shown (diamonds) for pulse 77590 at t=8s. Experimental points are shown (stars) and the fitted profile is over plotted as solid line. The radii values are along ECE line of sight.*

and it exhibits larger peaks in correspondence to m=2 mode resonant surface, but smaller average amplitude everywhere else. Anyway the fit can not return a quantitative value for mode amplitudes, since it is performed on coherence phase, which does not depend individually on the two amplitudes, but on the ratio of the two. It is worth remarking that m_1 and m_2 are fitting parameters as well, but their final value is not far from the initial one, even though they are not compatible with their nearest discrete value within the fit uncertainty.
A weakness in the model could be introduced by the choice of the shape of coherence amplitude, in fact the fitted points are very close to the experimental ones for the coherence phase, but not as much close in the total fluctuation amplitude plot. Perhaps a more meaningful function for mode structure might be deduced from the pressure fluctuation radial structure modelled in non linear magnetohydrodynamic calculations [67].
To check for the consistency of this method also a single m mode profile has been used as input function. This was unable to reproduce the experimental behaviour of the phase slope inside the main resonant surfaces, and also the second jump in the external zone.

A physical picture with two independent m=2 modes was considered as well, and the result of the fit is shown in Figure 4.14. The quality of the fit is clearly worse than the previous one, in fact the model is less good in reproducing the radial behaviour of the coherence phase even between the jumps. Furthermore the fitted m_2 value in this case is 2.567±0.012, which is very far from the m=2 initial value.
A similar thing happens trying to fit the experimental data using double mode structure with m=2 plus m=3 modes, both with tearing characteristic. In Figure 4.15 the result of the fit is shown, the fit parameters converged towards a minimum point close to the one obtained for the tearing-kink case, but the phase jumps due to the m=2 mode are more external, and the phase behaviour for R>3.6m is not reproduced (note that radiation coming from R>3.8m is heavily affected by non-thermal effects, and consequently it is not reliable).

A correct hypothesis should be compatible with rotation measurement results. The double tearing hypothesis would be well explained by the double island pic-

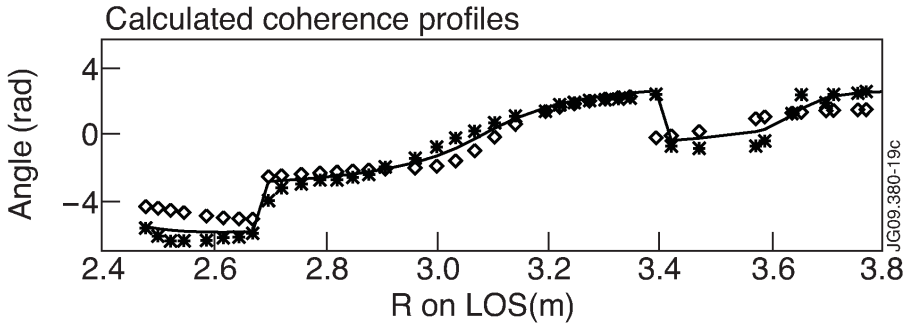

Figure 4.14: *In this figure the phase profile built using initial guess values is shown (diamonds) for pulse 77590 at t=8s (two different m=2 modes are supposed). Experimental points are shown(stars) and the fitted profile is over plotted as solid line. The radii values are along ECE line of sight.*

ture, in fact the generated multiple tearing structure should rotate at the same angular speed at different resonant radii, but being in clear conflict with the rotation shear induced in the plasma by external momentum injection, it could interact with the plasma itself via a torque, changing the rotation profile. The multiple tearing structure might act to cancel out the differences in toroidal rotation between the islands, in this way the rotation frequency of the most internal mode can be lowered by the torque exerted by the external island, which can in turn be accelerated by the torque of the main one, to a level in which the total torque balance between magnetic torque exerted by the other island and kinetic torque due to natural plasma rotation will be zero.
This explanation foresees the action of a very localized braking mechanism as the one experimentally observed, since from the measurements the effect of the mode is to reduce the rotation frequency in the channel nearest to the mode radial position, while in the other regions of the profile rotation is less affected. The toroidal momentum input to the plasma remains unchanged with the appearance of the

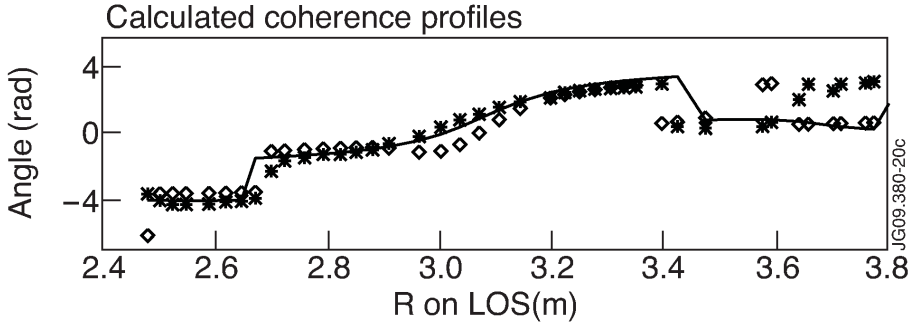

Figure 4.15: *In this figure the phase profile built using initial guess values is shown (diamonds) for pulse 77590 at t=8s (for m=2 and m=3 both tearing). Experimental points are shown (stars) and the fitted profile is over plotted as solid line. The radii values are along ECE line of sight.*

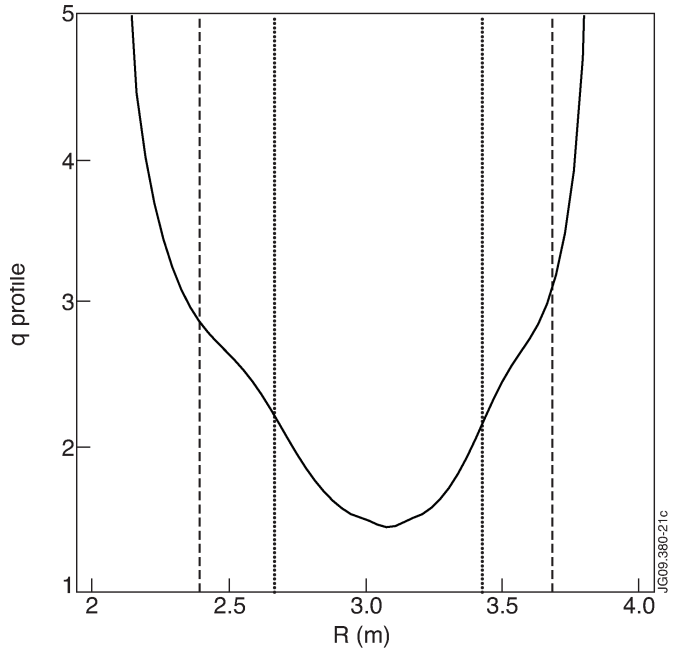

Figure 4.16: *In the plot the magnetic q profile at t=8s is shown for pulse 77590. The dotted line is the position of the tops on the m=2 double Gaussian, while the dashed line is the position of the m=3 double Gaussian.*

mode, though the zones in which the localized braking is active experience also the torque due to braking, the result of this mechanism might be a non monotonic rotation profile.
In the kink sideband picture a clear link from mode behaviour to rotation data is less straightforward to draw than in the double island picture. It is out of doubt that the mode has a clear impact on rotation, both in a localized and in a global way, though the origin of the braking mechanism needs still to be understood, and the presence of an interaction between the mode and an external error field might be invoked.

In Figure 4.16 the q profile from the equilibrium reconstruction is shown, for pulse 77590. The q profile is fairly peaked, with a value of q_{min} around 1.5, and it increases steeply going towards the edge. The fitted positions of the m=2 ECE fluctuation maxima for the best fit case are over-plotted as dotted lines, while the positions of m=3 maxima as dashed lines. It could be argued that m=2 mode positions are not in perfect coincidence with the position of q=2 surface, and also that the positions of m=3 mode in the low field side and high field side correspond to two different q values, but this is compatible with a systematic error in the total field determination, which affects ECE channel position at JET, and is now under investigation [68].
In this chapter the original work on NTMs poloidal structure has been presented, which has been carried out as first author during several visits to JET Culham Science Center [1].
The presence of a multiple jump structure in ECE phase radial profiles has been

documented in JET plasmas under different experimental conditions, and the consequences of this structure on plasma toroidal rotation have been analyzed.
Different hypotheses have been presented in order to explain the double phase jump experimental evidence, among these the most reliable is based on an m=2 plus m=3 structure. This hypothesis has been tested with an ad-hoc simple modelling of ECE fluctuation radial profile, which demonstrated a good agreement with experimental data.
It is worthwhile noting that both the two different m harmonics have been detected at the frequency of the mode, and for this reason could not be found previously with routine magnetic m analysis at JET. The insight on the radial mode structure given by the technique has indeed played a crucial role in the determination of the m mode structure as well.
The issue of the nature of the m=3 sideband is still open, in principle both a tearing structure and a kink structure could be adequate to describe the experimental evidence, even though the second one has proven to be much more effective in reproducing the experimental phase profile in a very good way. Being born at the same time of the main m=2 component, and rotating at the same angular frequency, the m=3 component appears to be an m=+1 toroidal sideband of the main NTM, which could not manage to cause forced reconnection at the q=3 surface, since the q=2 and q=3 surfaces rotated toroidally at different frequencies.
A simple mechanism for the interaction of the mode itself with plasma rotation has been proposed as well, particularly for the double island case, which involves the torque that the two island exerts one on each other.
More investigations are needed to explain the rotation behaviour in the kink sideband case, but we think that a localized resonant damping can only partially reproduce the complex observed behaviour.

CHAPTER 5

NTM impact on tokamak advanced scenarios

In this Chapter the impact of NTMs on JET advanced tokamak discharges will be documented.
Steady-state operation of ITER at $Q \approx 5$ is envisaged with a plasma current $I_P \approx 9MA$, a large fraction of which must be provided by the bootstrap mechanism. In these conditions q_{95} will be ≈ 5 and the minimum value of q (q_{min}) is expected to be > 1. It is well known that in this operational range the most degrading effect for plasma confinement will be represented by NTMs and RWMs. For this reason experiments have been performed on JET to vary the q-profile shape in this domain to investigate the effect on NTMs stability and confinement. The large ratio of resistive time (τ_R) to energy confinement time (τ_E) on JET ($\tau_r/\tau_e \approx$20-40) in these experiments at 1.1-1.6MA/1.6-2.3T has allowed the study of a wide range of q profile shapes without the need for fully non-inductive current drive [69]. This condition means that the characteristic time of changes in plasma confinement is much shorter then the equilibrium evolution timescale, and this permits to generalize obtained results in a stationary equilibrium condition.

The most extended study has been carried out in the $1.0 < q_{min} < 1.5$ domain, in which good stability was obtained with $\beta_N \approx 4$ for many τ_E, as shown in Fig 5.1. Here the neutral beam heating is applied at approximately the time that q_0 reaches unity due to current penetration during the initial phase of the pulse. The main obstacle to the prolongation of the high β_N phase was the onset of $m = 2, n = 1$ NTMs, the time of which is illustrated in Figure 5.1 for the pulses shown. The prompt appearance of these performance limiting modes was avoided by smoothly raising β, as illustrated in Figure 5.1, rather than abruptly applying high power heating.
When this optimisation is applied the 2/1 mode tends to appear on a timescale long compared with the energy confinement time, but small compared with the resistive time, indicating the slow evolution of the q profiles to a less favourable state. In plasmas of the type shown in Figure 5.1 the current density profile broadens during the heating phase, gradually shrinking the radius of the q=2 surface until the (2/1) mode becomes unstable. In this case both the local magnetic shear

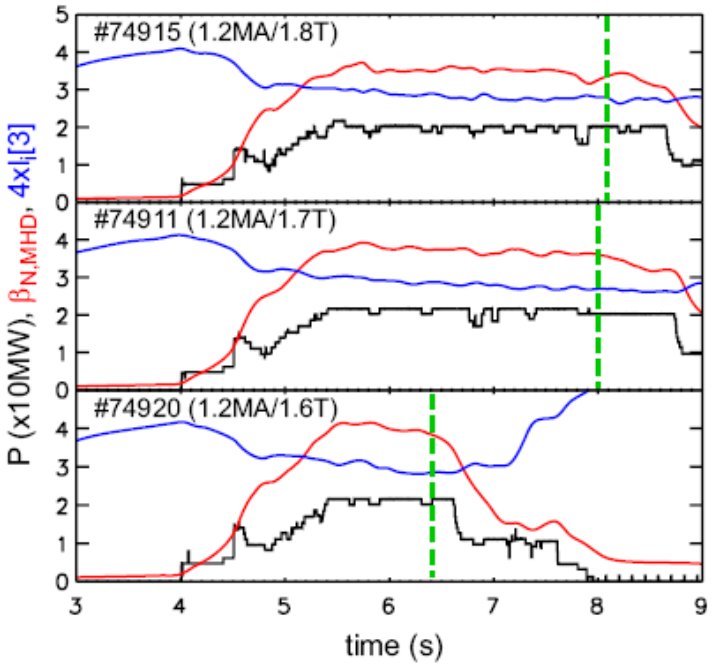

Figure 5.1: *Achieved β_N (also power and $4l_i$) for pulses with $q_{min} \approx 1.0 - 1.5$. Broken lines indicate onset of 2/1 mode. Taken from reference [69].*

and the pressure gradient at the q=2 surface are being modified, both of which may play a role in changing the stability of the observed mode.
The effect of the (2/1) mode on the plasma confinement is clearly seen in Figure 5.2, where $H_{IPB_{98}}$ is plotted as a function of time in (a), β_N is plotted in (b), and the n=1 magnetic amplitude is plotted in (c). The continuous (2/1) mode is triggered at 46.2s, it starts with a kink-balloning structure, as it can be seen in box (c) where the LFS amplitude is much larger than the HFS amplitude, and it keeps the kink structure until 46.5s [70]. After this time the mode turns into a classical (2/1) NTM, and the change in plasma quantities after the mode onset can be evaluated: β_N drops from 2.55 to 1.5, and $H_{IPB_{98}}$ drops from 1.3 to 0.8. The appearance of neoclassical tearing modes (NTMs) with higher toroidal mode numbers can also degrade the plasma confinement, and the avoidance of these has allowed the achievement of improved confinement with respect to the $H_{IPB_{98}}$ confinement scaling. The method used is analogous to the technique for avoiding the (2/1) mode, which is to increase the radius of low order rational q surfaces with $q > 1$ where deleterious instabilities can be encountered. To avoid large $q = 1$ sawteeth q_0 was simultaneously kept as high as possible, leading to an optimum q-profile with q_{min} close to unity and a wide region of very low magnetic shear in the plasma core. This class of q profile has been exploited on many tokamaks in the hybrid regime.
Despite the fact that none of these plasmas had a clear internal transport barrier (ITB), $H_{IPB_{98}}$ >1 could be obtained with $q_{min} \approx 1$ where NTMs associated with low order rational q surfaces were either absent or restricted to the plasma core.

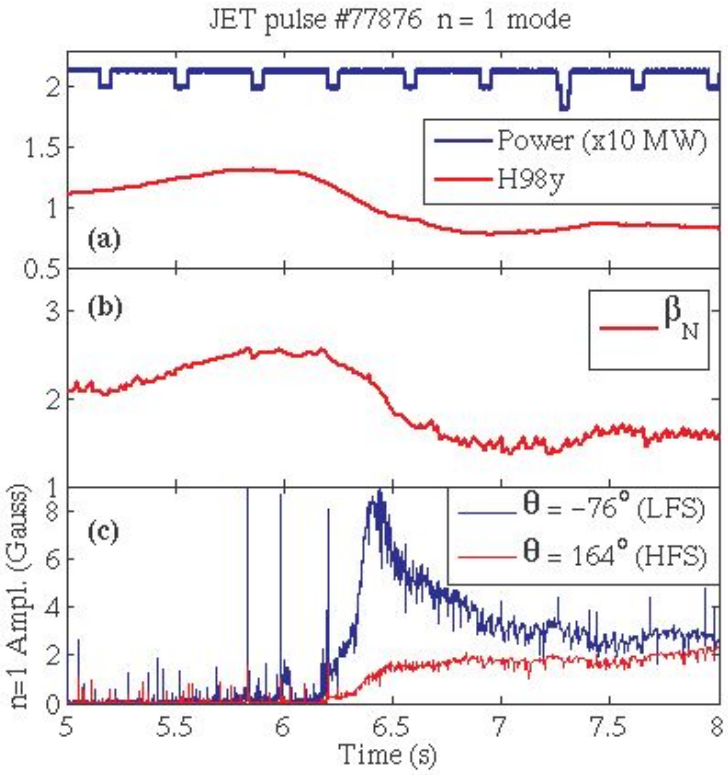

Figure 5.2: *a) Power and $H_{IPB_{98}}$ factor waveforms as a function of time. b) Normalized beta. c) n=1 mode amplitude on LFS (blue) and HFS (red). Taken from reference [70].*

Avoidance of low n NTMs was achieved using a plasma current overshoot just before the main heating was applied to generate a wide region of low magnetic shear close to $q = 1$ in the plasma core. This technique was developed for the hybrid regime on JET [71] and has led to good confinement ($H_{IPB_{98}}$ ≈1.3-1.4) and good stability ($\beta_N \approx 2.8$) for a period of order of a resistive time. During these pulses the radius of the $q = 1.5$ surface shrinks until a 3/2 NTM is triggered and the confinement is degraded.
The location of NTMs is an important factor in the resulting impact on confinement, as was suggested in [72]. The characterization of global plasma confinement drop with respect to the radius of the mode is ongoing for plasmas in the range $q_{95} = 4 - 5$. The analysis is complex, since the reduction of β_N due to the mode also causes a change in the plasma internal inductance l_i and the plasma shape. This mechanism can in turn determine a change in confinement which adds to the mode effect in the global confinement drop. For this reason the original plasma before the mode onset might not be the best reference to compare with the plasma after the mode onset. Work is ongoing to clarify this point.
The original contribution given in the reported analysis is the mode radial localization, which was performed with the ECE coherence technique.

CHAPTER 6

q=2 fishbones on JET

During JET campaigns aimed at the development of improved confinement Advanced Scenarios more performance limiting MHD activity has been documented other than NTMs. The observed modes are similar to fishbone modes in their magnetic signatures, with the appearance at a certain frequency and the subsequent chirp down in frequency of ≈20%. The most evident difference with respect to conventional fishbones is that, while the last are relatively benign, these modes can cause large and energetic ELMs, and also fast disruptive kink modes.
Similar chirping modes were observed also in other fusion devices, as JT-60U [73], DIII-D [74] and in past L-mode Scenarios with large ITBs at JET [75]. In addition these modes are thought to be influenced by energetic particles, and they have a role in triggering of RWMs, for this reason they have been also called Energetic particles driven Wall Modes (EWM).
In this chapter the experimental signatures of these modes will be reported, which were encountered and studied during the Steady State Scenario development campaign. The original contribution given to the analysis has been the thermal profile study of the mode oscillation.
The magnetic n analysis performed with high bandwidth pick up coils highlighted modes being n=1, as are conventional fishbones, but the frequency was generally lower than q=1 activity usual frequency, and in fact the q=1 surface was not present in Advanced Tokamak and Steady State Scenarios where the modes were observed.

The effect of chirping modes on a typical JET Steady State discharge is plotted in Figure 6.1, where the overall behaviour of pulse 78081 is shown. This pulse uses a Steady State high triangularity plasma scenario and it is characterized by 1.55 MA plasma current, a 2.7T toroidal field, β_n=2.7, and an external input power of approximately 21MW of NBI, 2.3MW of LH and 5.9MW of ICRH.
As it can be seen in the fifth panel from the top, where the D_α signal is plotted, the discharge enters H-mode around 44.4s with the first ELM, the electron temperature (fourth from the top) grows slowly until 45.4s, when a first bursting event appears in the odd-n magnetic signal in red (third from the top). This event does not have any effect on the plasma current in pink (first on top), and on $H_{IPB_{98}}$ in red.

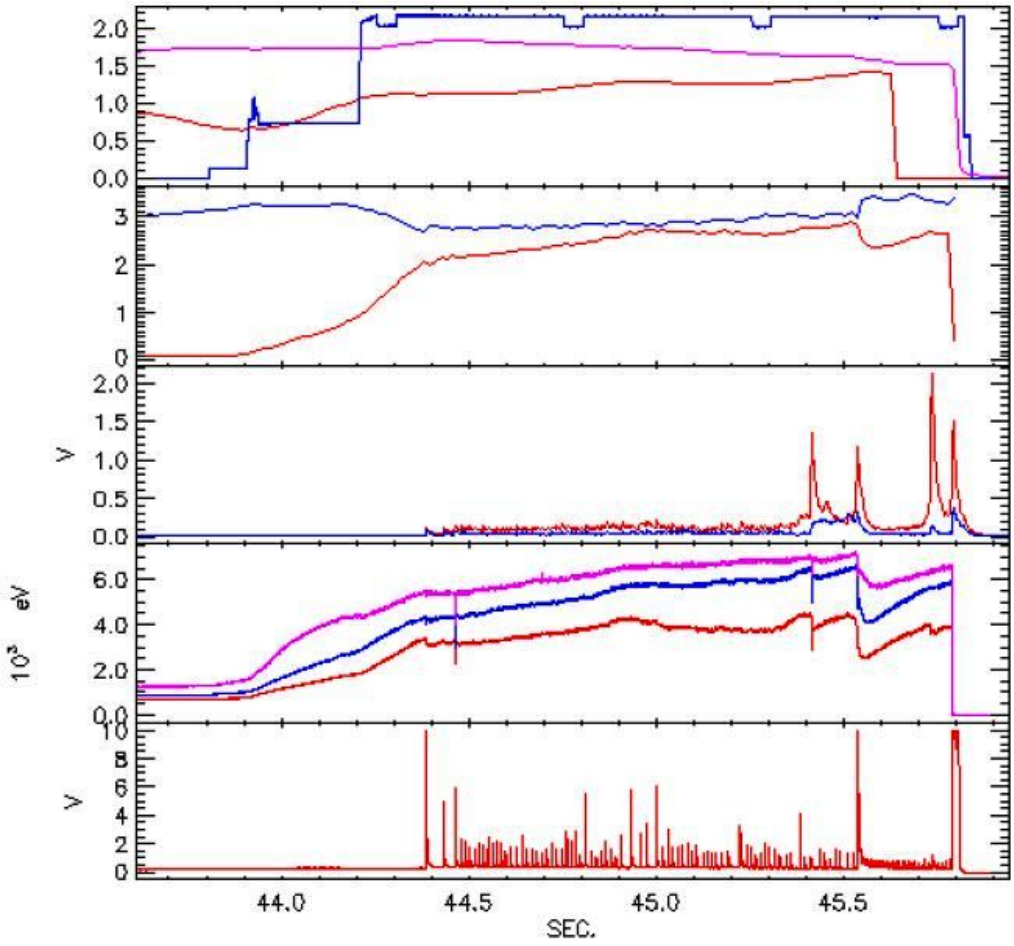

Figure 6.1: *First plot: $H_{IPB_{98}}$ in red, plasma current in pink (MA) and NBI power in blue(MW). Second plot: β_n in red and l_i in blue. Third plot: n=1 magnetic signal in red and n=2 in blue (a.u.). Fourth plot: electron temperature (ECE) at R=2.99m in pink, R=3.27m in blue and R=3.44m in red. Last plot: D_α signal (a.u.). The discharge begins at 40s.*

Another event appears in the magnetics at 45.52s, which has larger effect on the discharge: there is a large drop in the electron temperature which also corresponds to a peaking of the temperature and current profile, this is also reflected in the larger internal inductance l_i. The plasma shape is probably modified by the fast change in l_i, the interaction with the wall is changed and plasma goes in type three ELMs (last plot from the top). After this large drop the temperature recovers for 0.25s, then other two events are triggered, the first one being harmless, the second one causing a plasma disruption.

In Figure 6.2 the magnetic signature of three different events is shown. In all of the three cases the signal shows an exponentially growing oscillation with slightly decreasing frequency in time. After the growth phase the three events are rather different one from each other: in the green case the oscillation measured by pick up probes reaches a maximum and then it decays on its own, no locked mode is

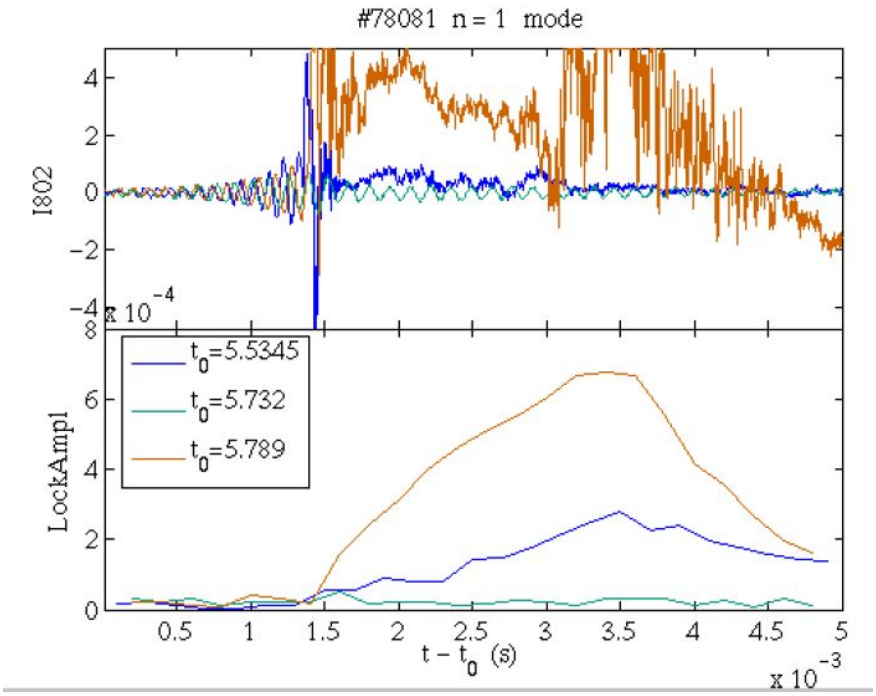

Figure 6.2: *Magnetic signal from a pick up coils on the top plot, and mode lock signal calculated using integrated signal from radial field saddle coils on the bottom plot.*

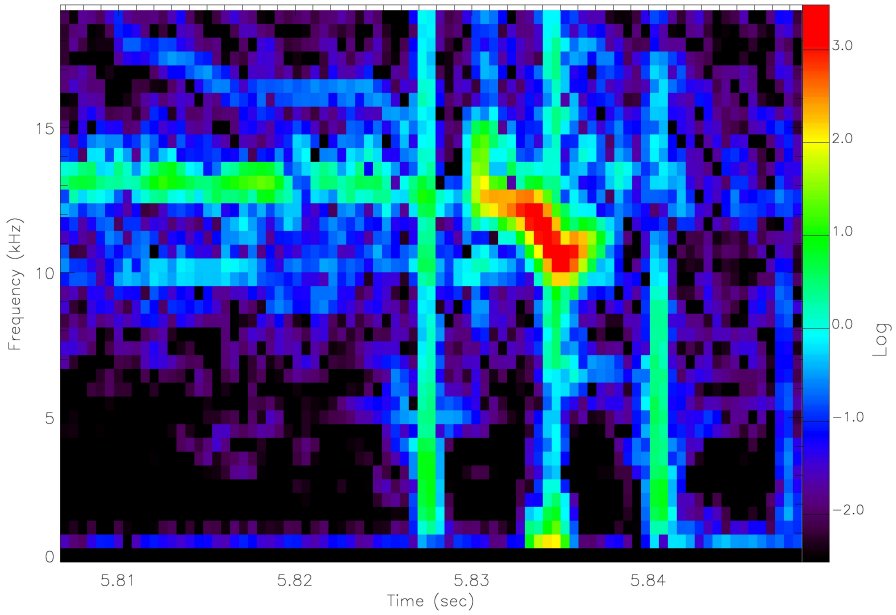

Figure 6.3: *Chirping mode magnetic spectrogram for JET pulse 77876. The colour scale is logarithmic in arbitrary units, the time scale is zeroed at 40s, at the beginning of the discharge.*

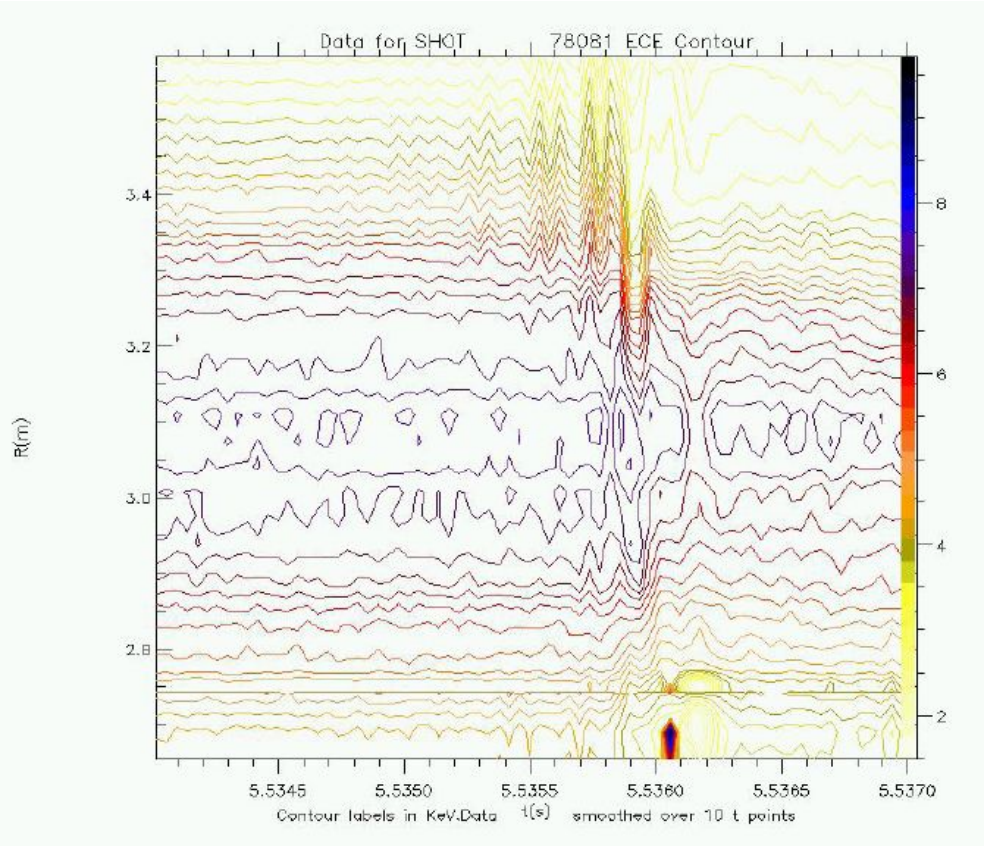

Figure 6.4: *Contour of electron temperature oscillations as a function of time and plasma major radius R, for pulse 78081 at 5.535s.*

detected. In the blue case the oscillation triggers a large ELM, afterwards there is a slowly growing mode in the locked mode signal which grows for two milliseconds, and then it disappears gradually. In the orange case after the ELM there is again a mode in the locked mode signal, which is though growing faster than the previous modes, and causes a disruption after few milliseconds.
An example of these modes in the magnetic spectrogram is seen in Figure 6.3, where the frequency components of the mode as a function of time are shown. As already said the mode starts at 45.83s at a frequency of 13kHz, and then it rapidly chirps down to 10kHz in 5ms. A broad band precursor is observed at 13 KHz [70].
The bursting nature of these modes and their fast timescale prevent the frequency analysis and the rotation localization used for NTMs. Nevertheless the displacement they introduce can be inferred from the oscillation in the fast ECE system, which are plotted in a contour in Figure 6.4 for the blue case. As it can be seen the oscillation radial profile is quite broad, the oscillations are visible for R>3.3m, and the peak in the oscillation amplitude is around 3.45m, which is the position of the q=2 surface from EFIT reconstruction. Another difference from q=1 fishbones is in the radial eigenfunction of the mode, which broad in the q=2 case, while quite localized in the q=1 case.
From the temperature oscillation the thermal profile redistribution that is caused

by the mode can be seen clearly: much of the thermal content in the outer part of the plasma is lost, and therefore the pressure profile becomes more peaked.
In Figure 6.5 the temperature oscillation induced in the green case is shown, the oscillation profiles are similar to the orange case ones before the large ELM: the oscillation is broad and purely kink, centered on q=2 surface. In this case the oscillation reaches a maximum and then decays alone going to lower frequency as well.
These modes can be very deleterious to the plasma discharge in two ways: either they can trigger a very fast disruption, as seen in Figure 6.1, or they can act as a trigger for q=2 continuous kink modes, which are high β modes observed is Hybrid and Steady State scenarios at JET that lead to a very large loss (20-30%) in $H_{IPB_{98}}$ and sometimes induce wall locking and disruption [70].
An example of this triggering mechanism is shown in Figure 6.6, where a magnetic spectrogram of the triggering is shown. The q=2 fishbone appears at 46.2s, it is possible to recognize the fast decrease in frequency even though the time scale is larger than in Figure 6.3. After the mode a continuous post-cursor can be seen at 9kHz, which lasts for the whole heating phase, causing a large loss in $H_{IPB_{98}}$.

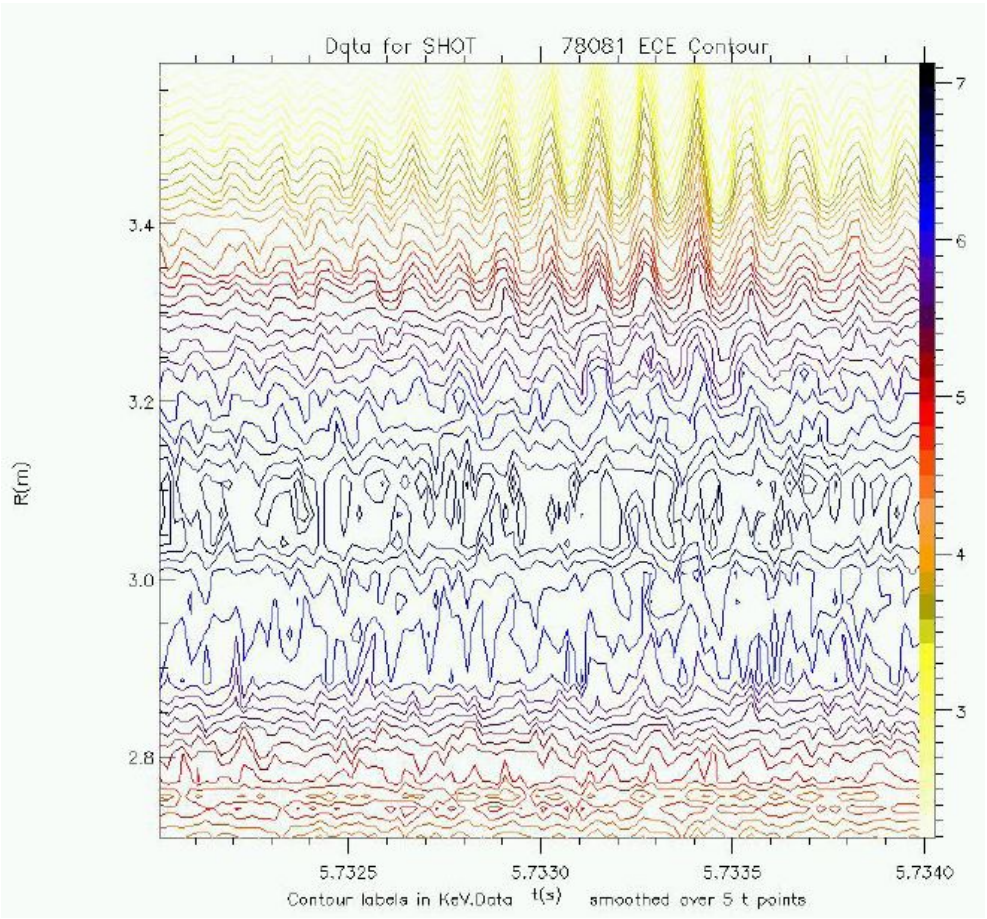

Figure 6.5: *Contour of electron temperature oscillations as a function of time and plasma major radius R, for pulse 78081 at 5.733s.*

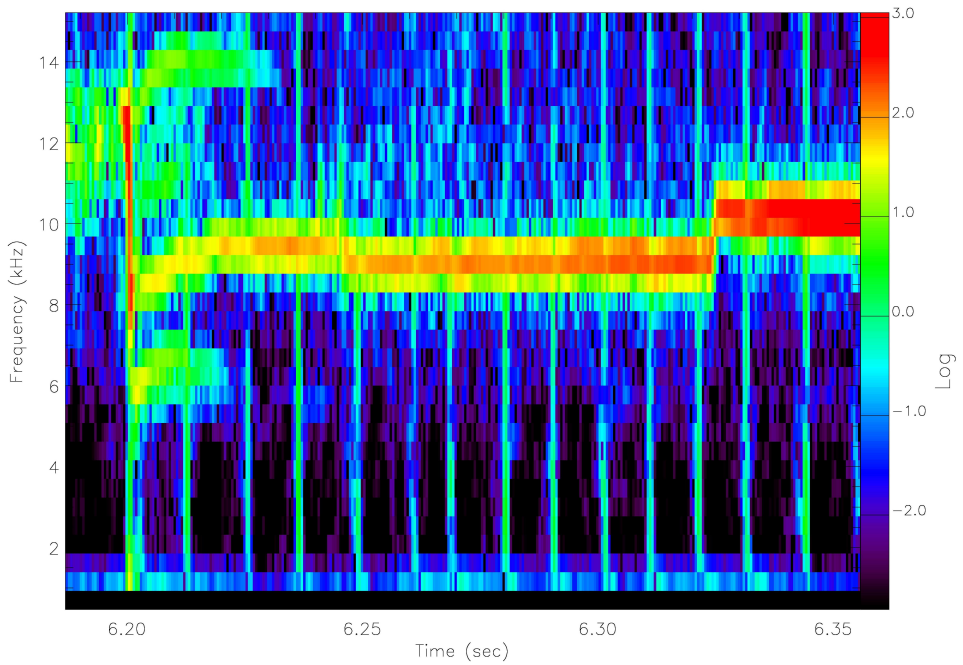

Figure 6.6: *Example of continuous kink mode triggering, as seen in the magnetic spectrogram for JET pulse 77876. The colour scale is logarithmic in arbitrary units.*

The continuous mode prevents the appearance of other fishbones, probably acting in the reduction of the fishbone drive.
It is therefore very important to understand what are the parameters that differentiate the benign q=2 fishbone that decays on its own, from the dangerous one that triggers ELMs and changes internal thermal profiles, making them more prone to disruptions.

CHAPTER 7

RWM growth rates characterization in RFX-mod

In this chapter the Resistive Wall Mode growth rates measurements in RFX-mod, which are carried out using the MHD active control system, will be presented.
For this reason in Section 7.1 the RFX-mod layout will be outlined, and the MHD active control system will be analyzed in detail, while in Section 7.2 the creation of a RWM growth rate database as a function of RFX-mod plasma parameters will be presented.

7.1 RFX-mod and its active control system

RFX-mod is a large Reversed Field Pinch device, with major radius of 2m, a minor radius of 0.459m, plasma current up to 2MA and a vacuum toroidal magnetic field up to 0.7T, even though a much lower toroidal field is needed in standard RFP operations. High frequency stabilization and fast plasma position control is provided by a thin copper shell (orange shell in figure 7.1) at average minor radius b=0.513m, of thickness h=3mm and vertical field penetration time of around $\tau_v = \mu_0 \sigma b h/2 = 50ms$ (μ_0 is vacuum magnetic permeability and σ is the resistivity of the wall material). This shell is composed by four pieces; two of the gaps are left insulated, while the other two are short circuited, either with copper plates or via welding [76]. A steel support structure lays outside the shell sustaining it (grey shell in figure 7.1), it has a field penetration time of about 15ms and poloidal and toroidal cuts located π far from the shell's ones. Inside the shell a stainless steel vacuum vessel is located, with a penetration time considerably smaller than the other two structures, of the order of 10ms. The vertical field penetration time of the overall conducting structures has been estimated as slightly greater than 60ms [77]. It is clear that this complex passive boundary will have, as we will demonstrate quantitatively, important consequences in the determination of the real structure of an unstable RWM during its growth.
The experiment is also equipped with an extensive set of 192 active saddle coils, divided in 48 poloidal arrays of 4 coil each, which cover the full surface of the

torus. These coils lay on the external surface of the support structure (in green in figure 7.1) and are independently fed, while on the internal surface of the shell 192 radial field saddle sensors are located, covering the same solid angle as the active coils, and also 192 biaxial pick-up probes are present, which measure toroidal and poloidal magnetic field in the middle of each saddle coil [78].
The dynamic response of the saddle coils is determined by a Proportional Integral Derivative digital controller, which can exert the control action both in real space (feedback gains applied to the field signals) and in the (m, n) Fourier space (gains applied to Fourier harmonics in the range m=-23,..,+24; m=-1,..,+2). During each control cycle the controller acquires 192 radial field signals, 192 toroidal field signals and 192 signals of current flowing in the active coils, plus other control signals, for a total of almost 600 signals. These signals are pre-processed and decomposed in Fourier components by an FFT algorithm, then the control algorithm is applied and the control reference for each mode is created. Finally an inverse FFT is performed on control references, creating signals that are sent to saddle coils power supplies. The cycle time strongly depends on the control algorithm used, and it is usually smaller than $400\mu s$ [79].

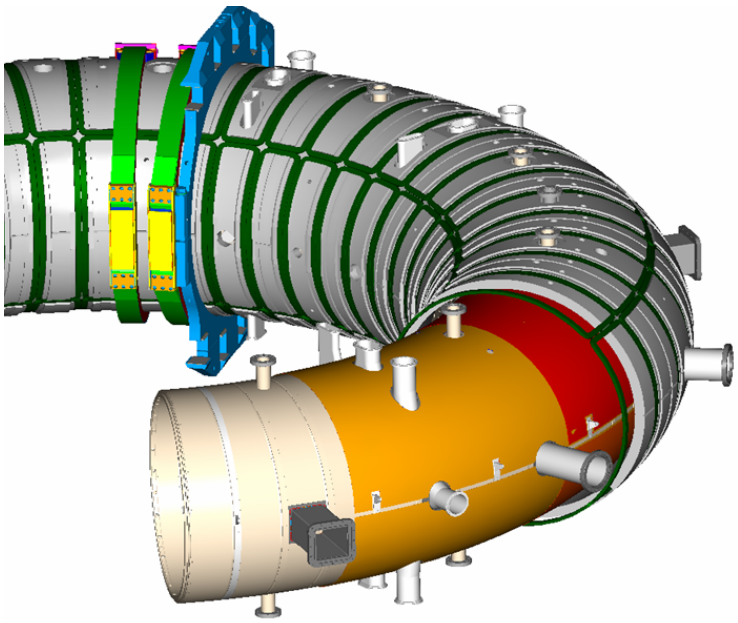

Figure 7.1: *RFX-mod control coils and passive structures layout.*

7.2 Growth rates measurement and statistical study

7.2.1 Description of the method

The possibility of using a feedback control in the Fourier space is a great advantage both from the performance point of view, because the suitable control PID gains can be studied and optimized for each mode, and from the physics point of view, because it makes possible to let grow a predefined number of modes free of control.

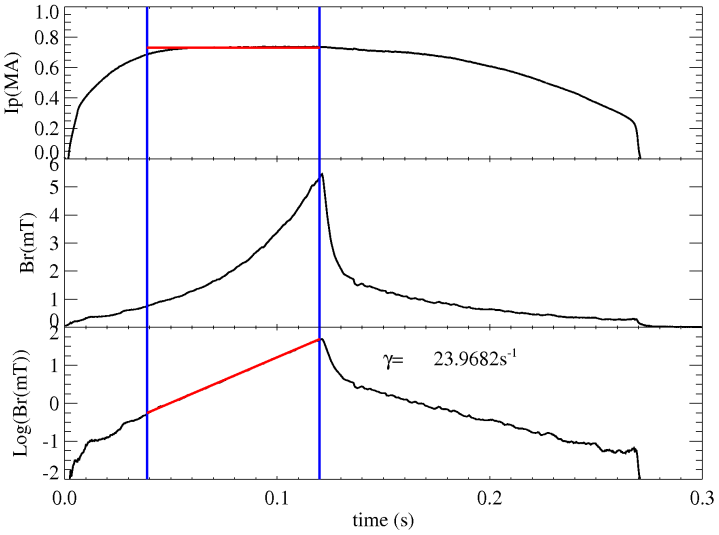

Figure 7.2: *RWM growth rate calculation in RFX-mod. The growth rate calculation interval is included within the vertical blue lines. The plasma current is shown in the top plot, with the average value shown in red. The (m=1,n=-6) magnetic amplitude is shown in central plot and its logarithm in the bottom plot, the calculated growth rate is the angular coefficient of the red line.*

This flexibility permitted the characterization of each mode's unperturbed growth, and the simultaneous growth of different modes to verify possible couplings.
An important feature of the controller is that control strategy can be changed along the discharge using different time windows, so each mode can be set free to grow just in a predefined time window decided by the operator, for example making it coincident to the flat top of the discharge. The importance of this feature is related to the need of selecting the most stationary plasma conditions along the discharge, to ensure a constant mode's drive, therefore a constant RWM growth rate, to facilitate data interpretation. This can be seen in Figure 7.2, where the $(m = 1, n = -6)$ mode grows free in the first control window from 0ms to 120ms, while it is controlled in the second control window to avoid detrimental effects to the discharge.
The real time control signals are suitable for RWM growth measurement and post pulse analysis as well. The magnetic signal of the various harmonics can be obtained with spatial FFT of radial field sensor's signal, which gives amplitude and phase for each (m, n) harmonic. The logarithm of mode's amplitude is calculated, and the growth rate is obtained as the coefficient of a linear interpolation of logarithmic amplitude versus time (Figure 7.2). This procedure has been implemented in an automatic fashion.
In this section the result of a statistical study of measured RWM growth rates in RFX-mod will be presented, which contains all of the pulses with RWM free to grow since the beginning of active control system operation. The creation of the database, and the refinement of the growth rate measurement was an original contribution of mine.

For each of the considered pulses, for each control time window and for each resistive wall mode free to grow, the mode's growth rate was calculated within the maximum interval in which the growth rate was purely single exponential. This constraint is important to avoid the effects of possible spurious error fields or sudden changes in the mode drive polluting the measurements. The range of the fitting interval was enlarged in an iterative way, until the merit parameter $r = cov(a,b)/\sigma_a\sigma_b$ kept larger than 0.99999, indicating a good linearity. In the equation a and b are the two considered variables (the time and the logarithmic amplitude of the mode in our case), $cov(a,b)$ is the covariance between a and b, and σ_a and σ_b are respectively the standard deviations of a and b. In this way a database of 949 points, related to 337 plasma pulses was established.
In some circumstances the repeated measurement of a negative growth rate was possible, in the presence of reproducible error fields due to current ramp up, which led to the growth of certain harmonics in the first 50ms of the discharge [80]. This effect was observed for $(1,4)$ and $(1,6)$ modes, and gave the possibility to measure the exponential decay of these harmonics from a finite amplitude value to the noise level.
To reveal possible dependencies of RWMs growth on plasma parameters, the measured growth rates have been then classified as a function of the main plasma equilibrium parameters in RFX-mod, such as the plasma current I_p, plasma electron density n_e, β_ϑ defined as

$$\beta_\vartheta = \frac{2 < p_e >}{\frac{B_\vartheta(a)^2}{2\mu_0}} \tag{7.1}$$

and the reversal parameter F defined as

$$F = \frac{B_\phi(a)}{< B_\phi >} \tag{7.2}$$

the latter parameter is distinctive of RFP equilibria, and is tightly linked to the radial position of toroidal field reversal surface inside the plasma: the more negative its value the farther from plasma edge is the reversal surface.
The mentioned quantities have been averaged in the growth rate fitting window, provided them to be stationary. This was ensured in the fitting procedure since the progressive extension of fitting window has been constrained in intervals where the main plasma quantities were constant.
The global range of variation for the statistic studies and the number of experimental points is shown in figure 7.3, where plasma equilibrium parameters in each fitting window are plotted as a function of the pulse number .
The explored parameters range was determined by the match of intentional scans with RFX-mod operational constraints. An example is the large number of low plasma current discharges compared to high current discharges, that are difficult to perform and dangerous with regard to enhanced plasma wall interaction and thermal stresses that might be induced by a wall locked RWM. A similar criterion holds for F range, in fact though several F scans have been performed, very negative F experimental points are less frequent than near zero F points, because the operation in that range implies a very resistive RFP plasma, with a large needed loop voltage and the risk of a non sustained plasma current discharge. The results

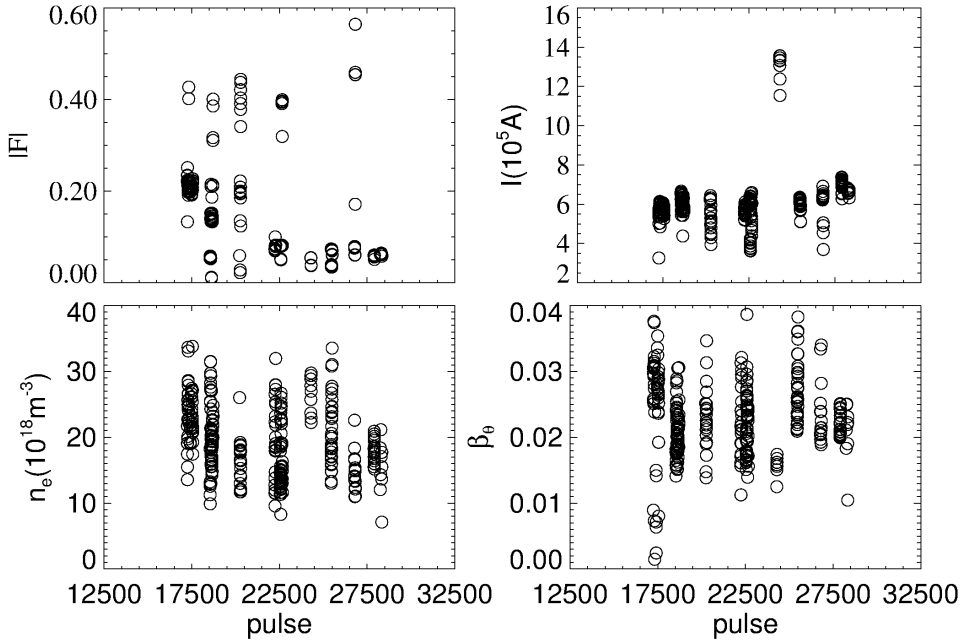

Figure 7.3: *Plasma equilibrium parameters variation as a function of pulse number in different RWM campaigns in RFX-mod*

of the statistical study for (m=1, n=-6) RWM harmonic is shown in figure 7.4, where measured RWM growth rates are plotted as a function of plasma current, line averaged electron density, β_ϑ and reversal parameter F. The line averaged electron density is an interferometric measure, β_ϑ is calculated using line averaged electron density and plasma temperature measured using the double filtered *Bremsstrahlung* emission, while I_p and F are obtained from magnetic measures. The error bars on single points are the output error of the linear fit for the growth rate calculation (colors will be explained in Section 8).
The chosen parameters set was considered to be complete for the description of the RFP equilibrium. Another parameter commonly used for RFP equilibrium description is Θ, described as:

$$\Theta = \frac{B_\vartheta(a)}{< B_\phi >} \tag{7.3}$$

this parameter was initially considered and successively discarded, because in common RFP operation it is tightly linked to F value [81].
Growth rate predictions have been over-plotted in the experimental plots as triangles for several F values, which were obtained using a linearized MHD cylindrical code [33] and considering $\beta_\vartheta = 0$, and the equilibrium lying into the $F - \Theta$ curve [81] (Figures 7.4,7.5,7.6,7.7,7.8,7.9).
It is already clear from figure 7.4 that the only evident dependence of $m = 1$ $n = -6$ RWM growth rate on considered plasma parameters is, as expected, on $|F|$, while the other plots show a larger scatter. For this reason we will show for the other RWMs just the γ versus $|F|$ plots (Figures 7.5, 7.6, 7.7, 7.8, 7.9), and we will comment the results in the following subsections, separating the internal

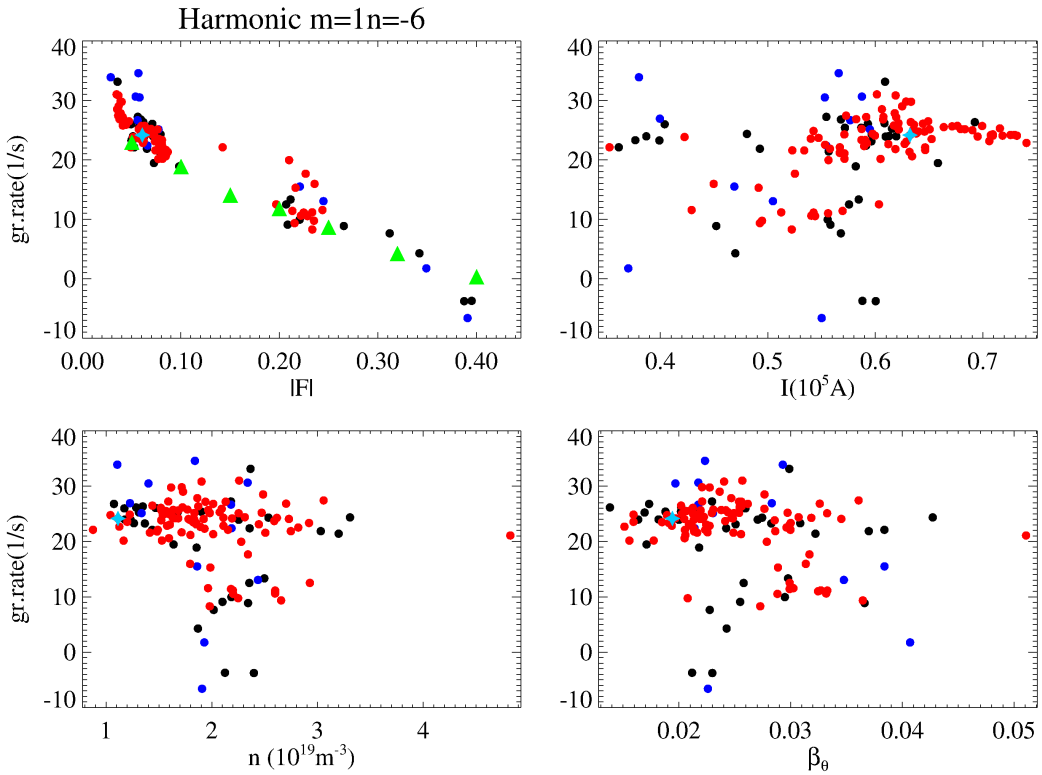

Figure 7.4: *RWMs experimental growth rates as a function of plasma equilibrium parameters for m=1,n=-6 RWM (circles). Cylindrical growth rate calculations are over-plotted (triangles).The color code is explained in Chapter 8 (the same is true for Figures 7.5-7.9).*

and external modes cases.

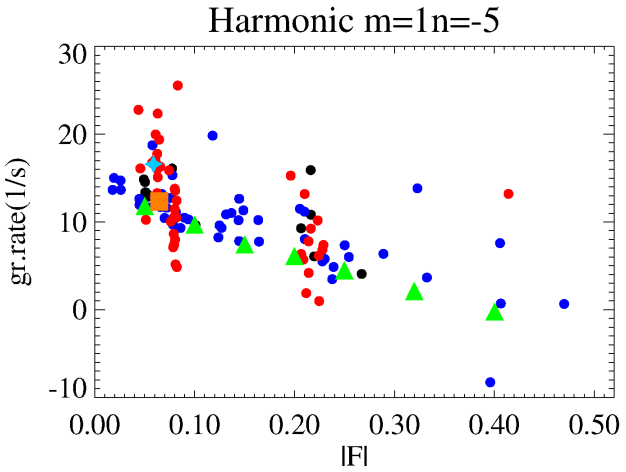

Figure 7.5: *RWMs experimental growth rates as a function of $|F|$ parameter for m=1,n=-5 RWM (circles). Cylindrical growth rate calculations are over-plotted (triangles).*

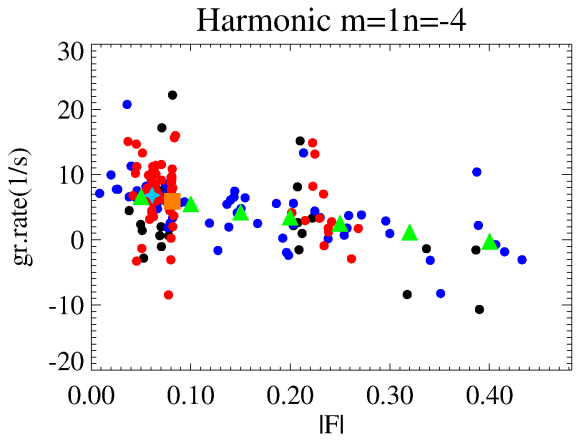

Figure 7.6: *RWMs experimental growth rates as a function of $|F|$ for m=1,n=-4 RWM (circles). Cylindrical growth rate calculations are over-plotted (triangles).*

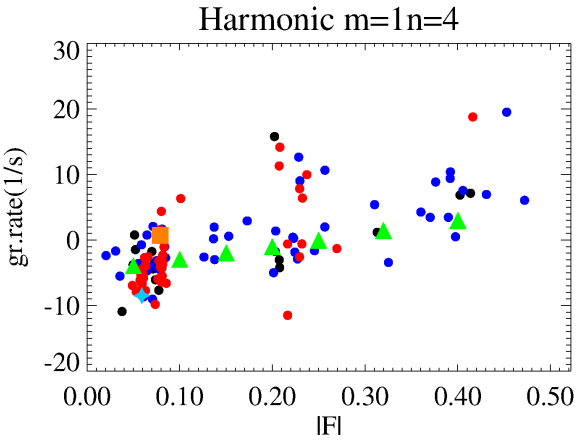

Figure 7.7: *RWMs experimental growth rates as a function of $|F|$ for m=1,n=+4 RWM (circles). Cylindrical growth rate calculations are over-plotted (triangles).*

7.2.2 Internal RWM

These are the RWMs that are characterized by the same helicity direction as magnetic field lines inside the toroidal field reversal surface, i.e. the surface inside the plasma where the toroidal field changes sign, and by convention are identified by negative n number [81]. In the RFX-mod case these modes are mainly $(m = 1, n = -4, -5, -6)$, and are predicted to be unstable for small $|F|$ values [27, 33, 82].
For these modes no significant dependence is observed in any of the plasma parameters, except from $|F|$. This can be seen in Figure 7.4, where the top-right plot and the bottom plots do not show any particular trend, while there is instead a clear trend in reducing $(1, -6)$ growth rate with $|F|$.
For all of the internal mode branch the experimental trend is in good agreement

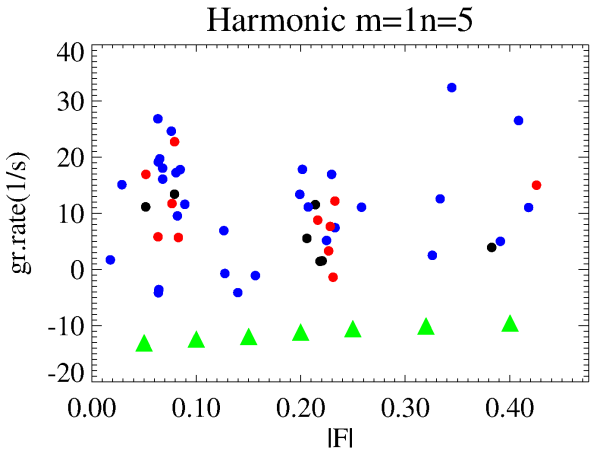

Figure 7.8: *RWMs experimental growth rates as a function of $|F|$ for m=1,n=+5 RWM (circles). Cylindrical growth rate calculations are over-plotted (triangles).*

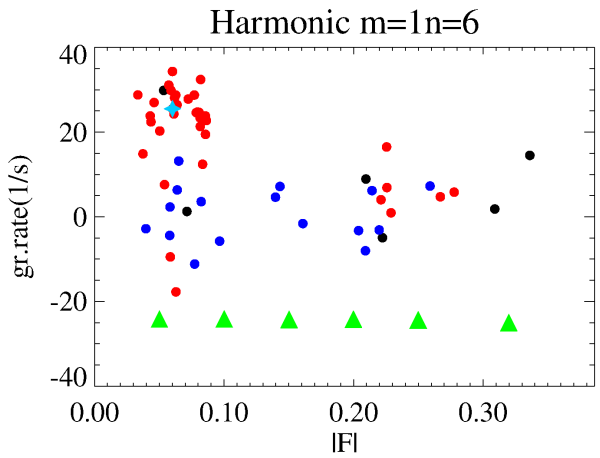

Figure 7.9: *RWMs experimental growth rates as a function of $|F|$ for m=1,n=+6 RWM (circles). Cylindrical growth rate calculations are over-plotted (triangles).*

with cylindrical theory predictions (see Figures 7.4,7.5,7.6), apart from a cloud of data points with a larger growth rates spread observed for $(m = 1, n = -5, -4)$ mode in the small $|F|$ range. More attention to this feature will be given in Chapter 8.

7.2.3 External RWM

These are the RWMs that are characterized by having the same helicity direction as magnetic field lines outside the toroidal field reversal surface, and by convention are identified by positive n number. In RFX-mod case these modes are mainly (m=1, n=4,5,6) (see Figures 7.7,7.8,7.9).
As far as the dependency on plasma parameters is concerned, external RWMs behave as internal RWMs, with the difference that the growth rate dependence on $|F|$ value is opposite. There is an exception to this general trend which is the $(1, 6)$

mode, for which we see that the growth rates for $|F| < 0.1$ are composed by a a positive spot with the same value of $(1, -6)$ growth rates, plus a negative trend. This difference has been studied both on the single pulse and statistically, and a consistent explanation for it has been found as will be shown in Section 8.
For the external RWM branch the comparison with cylindrical code predictions is worse than for the internal branch, indeed a good agreement can be seen in the $(1, 4)$ mode case, while for $(1, 5)$ and $(1, 6)$ harmonics the code foresees a much stronger stability than what observed in the experiment. It should be pointed out that for the negative growth rates cases the growth rate determination is less accurate than for the positive ones, because negative growth rates measurement would need a different experimental setup, and no ad-hoc experiments have been performed up to now.

CHAPTER 8

3D effects on RWM physics in RFX-mod

In this Chapter relations and couplings between different RWMs harmonics will be investigated. This important effect can have very different origins in fusion devices, from the geometrical coupling due to toroidicity and plasma shaping (higher for low aspect ratio, non circular tokamaks), to 3D effects due to eddy currents in non homogeneous conductors surrounding the plasma.
The original contribution I gave to this work was in all of the experimental analysis, including the design of dedicated experiments for the coupling demonstration, and in the interpretation of the experiment-model comparison.

8.1 Experimental characterization of 3D effects

The first aspect that has been studied is the poloidal structure of an unstable RWM in RFX-mod. To do this, a set of experiments where not only the most unstable RWM, but also its poloidal harmonics are included or excluded from the control loop have been realized. As in the previous studies the main plasma parameters are carefully kept constant.
In Figure 8.1 the results of such an experiment are presented: the black lines are related to a discharge where the full RWM spectrum ($m = 0, 1, -1, 2; n = 4, 5, 6$), including $(1, -6)$ poloidal harmonics are not controlled, while the blue ones describe the case of $(1, -6)$ controlled and the rest of RWM spectrum not controlled. From frames *a*,*b*,*c* and *d* it is clear that, when $(1, -6)$ is not controlled, also the $(0, -6)$, the $(1, -6)$ and $(2, -6)$ modes, which are normally stable for this equilibrium, grow exponentially as the main unstable RWM and with comparable growth rates (around 24 s^{-1} in this case). The growth rate calculation was performed in the time interval enclosed by vertical lines, and the output growth rates are reported with the same color code of experimental data. The measured growth rates are in good agreement with what observed statistically, the black case growth rate is reported as a cyan star in Figure 7.4, 7.5, 7.6, 7.7, 7.9, while the blue line growth rate is reported as an orange square in Figure 7.5, 7.6, 7.7. The example

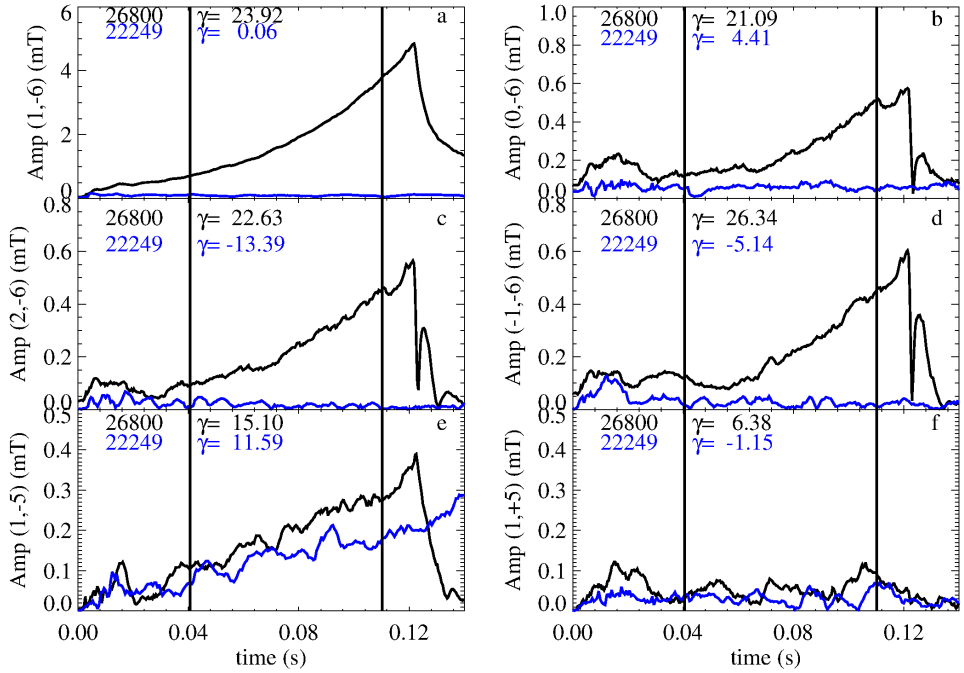

Figure 8.1: *Comparison between two experiments with different control of the harmonics of the most unstable RWM,* $(1,-6)$*. In the black case the full RWM spectrum* $(m = 0,1,-1,2; n = 4,5,6)$*, including* $(1,-6)$ *poloidal harmonics are not controlled. In the blue case the* $(1,-6)$ *mode is controlled but the rest of RWM spectrum is not controlled. Vertical lines delimit the growth rate calculation interval.*

growth rates are not reported in all of the statistical study figures, since the very low growth rate cases also have a large noise error on the g.r. calculation, and therefore are discarded.

To better understand the origin of $(0,-6)$, $(1,-6)$ and $(2,-6)$ harmonics in the spectrum of the unstable RWM, that we recall should be stable according to cylindrical calculations, a second set of experiments has been performed. Following a procedure already developed to study other aspects of RWM physics [44], on the same target plasma, the most unstable RWM is controlled with sub-critical gains (i.e. the growth rate is reduced by the action of the control system, but it is still positive), while its poloidal harmonics are not controlled at all. In figure 8.2 the time traces of relevant mode amplitudes as measured by the saddle sensor system are presented. We see that the $(0,-6)$, $(1,+6)$ and $(2,-6)$ amplitudes follow the time behaviour of the main unstable harmonic, confirming a close relation between the $(1,-6)$ growth and the growth of its poloidal harmonics. In this case the same growth rate calculation interval has been chosen for all of the pulses to have a more precise comparison of growth rates, and it is delimited by vertical lines in the plot. As it can be noticed the growth rates are not in perfect agreement for the three different harmonics, in particular when the sub-critical gains are larger and therefore the overall growth rate is near to zero. This is due to the fact that in these cases the signal to noise ratio becomes small, and therefore the growth

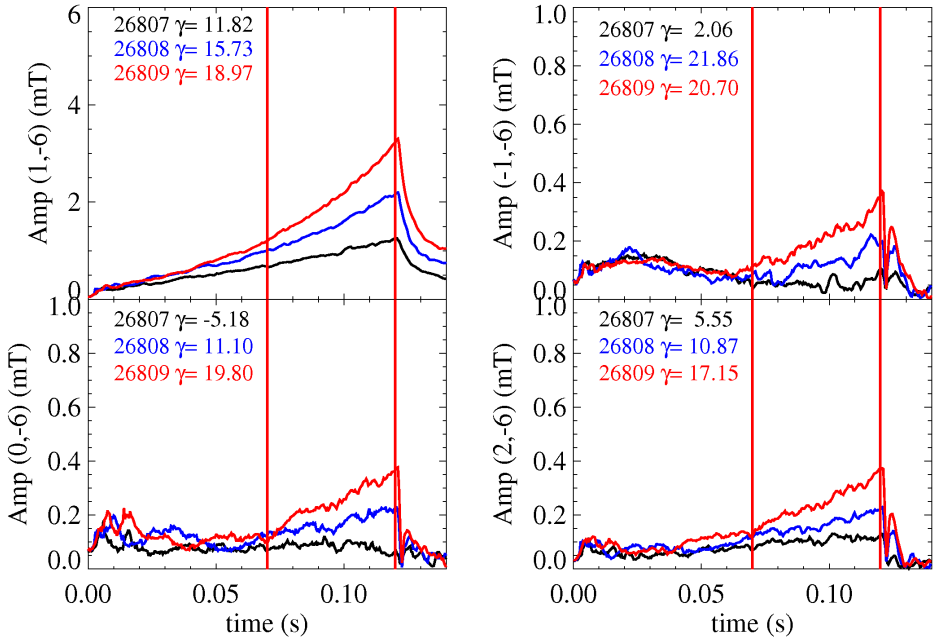

Figure 8.2: *Mode amplitudes for three different sub-critical proportional gain on the most unstable RWM, (1,-6) in the window 0-0.12s; the poloidal harmonics are instead not controlled during the same time interval.*

rate calculation is not accurate.
Looking carefully at relative amplitudes and phases of the different harmonics, the easiest explanation to the multiple instability of different poloidal harmonics, that would only invoke a geometrical toroidal coupling, does not seem to be sufficient to explain all the results. In fact, taking into account the fact that the aspect ratio of the RFX-mod device is $R/a = 2/0.459 \approx 4$, one would not expect the same amplitude for the $(0, 6)$, $(2, 6)$ and the $(1, 6)$ harmonics. While this effect is obvious when the interaction of a perturbation with the mean field is considered, due to its $1/R$ dependence, may not be so clear for perturbations alone. The analogy should be done with the theory of an helical field in a toroidal geometry, developed originally for stellarators (see for example [83]) using a perturbative approach in (a/R), to find the effect of the toroidal geometry on helical magnetic fields.

By following this approach the effect of the toroidal geometry on a given m, n mode can be expressed by the following convolutions:

$$C = b_r \sin(m\vartheta + n\phi)\left(1 - \frac{a}{R_o}\cos(\vartheta)\right) \tag{8.1}$$

where C is the tridimensional shape of the radial field produced by the mode, and b_r is the mode's radial field amplitude. By expanding the product it is easily seen that at first order in a/R:

$$C_1 = -0.5\frac{a}{R_o} b_r \left(\sin(n\phi + (m+1)\vartheta) + \sin(n\phi + (m-1)\vartheta)\right) \tag{8.2}$$

therefore at first order only the $m = 0$ and $m = 2$ modes are obtained, while the $m = -1$ mode is only obtained at second order from:

$$C_2 = \left(0.5\frac{a}{R_o}\right)^2 b_r \Big(\sin(n\phi + (m-2)\vartheta) + \\ + \sin(n\phi + (m+2)\vartheta) + 2\sin(n\phi + m\vartheta) \Big). \tag{8.3}$$

Therefore these results are the first experimental quantitative demonstration of the coupling effect between the main unstable RWM and its poloidal harmonics due to the toroidal gaps of the passive machine boundary, as already suggested by 3D computations [46].
Examining experimental results, also the uncertainties on harmonics amplitude calculated via FFT must be taken into account. In fact the determination of high order poloidal harmonics is rather difficult using RFX-mod realtime signals, because saddle-loops poloidal arrays are composed of only 4 probes, this means that it is not possible to resolve poloidal harmonics with $m > 2$, and the determination of $m = 2$ component is probably spoilt by the sidebands of the unseen components. RFX-mod off-line diagnostic set contains 4 poloidal arrays composed of 8 toroidal and poloidal field pick up coils each, but these arrays are non equally-spaced in toroidal direction. The low toroidal periodicity implies that these arrays can not be used to extract $n = 6$ component, and therefore do not allow to distinguish it from the background magnetic noise coming from high n tearing modes.
In the set of experiments performed also the coupling among different toroidal harmonics of the main unstable RWM has been studied. This phenomenon is visible again in Figure 8.1, frames e and f, where the growth of $(1, -5)$ and $(1, +5)$ modes is shown as well. The $(1, +5)$ mode is stable for this equilibrium and it is not affected by the $(1, -6)$ mode, while the $(1, -5)$ growth seems to be indeed modified by the $(1, -6)$ growth, in fact the mode amplitude is larger when also the $(1, -6)$ mode is growing, and the calculated growth rate is also larger of a 25% factor. The reason for this coupling might be the presence of poloidal gaps in the passive machine boundary, in a similar way it can work for the coupling between different poloidal harmonics of the same n component. Note that the detection and measure of this coupling is more difficult that the previous one, because the $(1, -5)$ harmonic is unstable itself also without $(1, -6)$ mode, therefore the assesment and measurement of the coupling is based on the difference between measured growth rates, which are often spoilt by noise in magnetic signals.

8.2 Codes predictions comparison

Following the experimental coupling demonstration, the comparison between RWMs growth rate predictions by three different codes will be shown, with the aim of understanding if the observed RWM coupling can be better explained by a model that includes the real 3D geometry of the external structures.
The simplest approach to numerical RWM stability is the cylindrical code ETAW, extensively used in the past on RFPs [82], it solves the linear cylindrical resistive

incompressible MHD equations, using a spectral formulation and a matrix shooting eigenvalue scheme. Thin shell boundary conditions are imposed to take into account of resistive wall, while the solution of the cylindrical Laplace equation in the vacuum region is analytically represented in terms of modified Bessel Functions.
MARS-F [84] is a toroidal stability code that solves single fluid MHD equations, including vacuum region, thin conducting shells, and feedback coils. (Other features of the code, such as sheared toroidal plasma rotation, sound wave or kinetic damping terms, are not used in this paper.) It can only treat conducting structures (walls or coils) that are axisymmetric along the major axis of the torus.
CarMa is a recently developed code [46], capable to analyze RWM stability taking rigorously into account the three-dimensional features of the conducting structures surrounding the plasma and able to self-consistently treat multi-modal plasma evolution. This code couples the instantaneous massless plasma response matrix to magnetic field perturbations over a surface S with a 3D volumetric integral formulation of the eddy currents problem, which describes the conducting structures by means of a three-dimensional finite elements mesh.
As mentioned, when toroidal coupling is taken into account, all m harmonics should be considered in the model. For this reason, using a toroidal code like MARS-F, for a given n value, we find two unstable modes corresponding to two different growth rates. These new growth rates are however close to γ_{+n} and γ_{-n}, since toroidal corrections are expected to be of the order of the device inverse aspect ratio $\epsilon^{-1} = a/R$, and hence small in the RFX-mod case ($\epsilon^{-1} \approx 0.25$). Each of these two modes involves theoretically all m values, but in practice they have

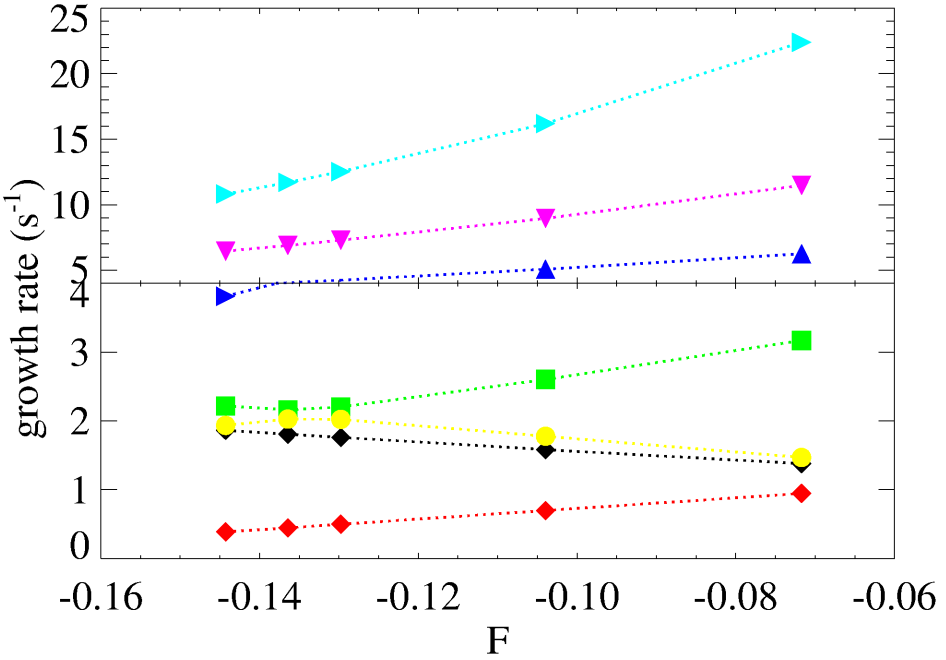

Figure 8.3: *Growth rates of multiple unstable RWMs due to toroidal coupling effects as predicted by MARS-F.*

a dominant $m = \pm 1$ component. Figure 8.3 shows the behaviour of the growth rates of such two different unstable modes for $n = 2$ (black triangles and red diamonds) and $n = 3$ (yellow circles and green squares), as computed by MARS-F for various RFX equilibria with $\Theta = 1.49$, as a function of F. In the same picture the $n = 4, 5, 6$ growth rates as a function of F are shown as well, the data is in good agreement with experimental data shown in figures 7.4, 7.5, 7.6.
With an axisymmetric wall, i.e. using MARS-F, each of the aforementioned unstable growth rates (e.g. γ_{+n}) correspond to two eigenmodes, which are identical apart from a rotation of $\pi/2n$ in the toroidal direction. When a three-dimensional conducting wall is considered in CarMa, like for instance a shell with a poloidal gap breaking toroidal symmetry, this degeneracy is removed and the two toroidally shifted unstable eigenmodes are characterized by two distinct unstable eigenvalues (e.g. γ'_{+n} and γ''_{+n}). Hence, including both toroidal and 3D effects, for each n value one can have four unstable eigenvalues: γ'_{+n}, γ''_{+n} , γ'_{-n}, γ''_{-n} [46].

Two different equilibria have been considered for the overall comparison: equilibrium A (F=-0.073, Θ=1.43) and equilibrium B (F=-0.136, Θ=1.49). Table 8.1 reports a comparison of the RWM growth rates, as predicted by the three codes, together with typical experimental values, measured in configurations with parameters F, Θ in the same range as simulations (no profile comparison has been carried out, given the fact that internal current profiles measurements are not present in RFX-mod). Clearly, three dimensional effects give rise to a sometimes significant increase of the growth rate, which is in better agreement with experimental data than axisymmetric or cylindrical calculation. Note that only the copper shell has been considered in these simulations; in preliminary results that include also the

Table 8.1: *Comparison of growth rates for two RFX-mod equilibria (all results in s^{-1}). Only unstable RWMs are considered*

	Equil A				Equil B			
Code	ETAW	MARSF	CarMa	Exp	ETAW	MARSF	CarMa	Exp
n=1	0.909	< 0	< 0	< 0	< 0	< 0	< 0	< 0
n=2	1.56	0.780	0.869	N.A.	< 0	0.434	0.448	N.A.
			0.931				0.462	
	1.82	1.29	1.67		2.45	1.81	2.33	
			1.81				2.36	
n=3	0.727	1.10	1.37	N.A.	1.82	2.08	2.61	N.A.
			1.40				2.64	
	3.09	2.71	3.69		1.90	2.16	3.13	
			3.78				3.26	
n=4	5.27	5.07	7.30	$\approx$6	4.09	4.04	5.63	$\approx$6
			7.48				5.78	
n=5	8.63	8.55	12.8	$\approx$12	6.81	6.89	9.91	$\approx$8
			13.1				10.2	
n=6	14.5	14.4	22.6	$\approx$22	11.8	11.7	17.6	$\approx$17
			23.4				18.2	

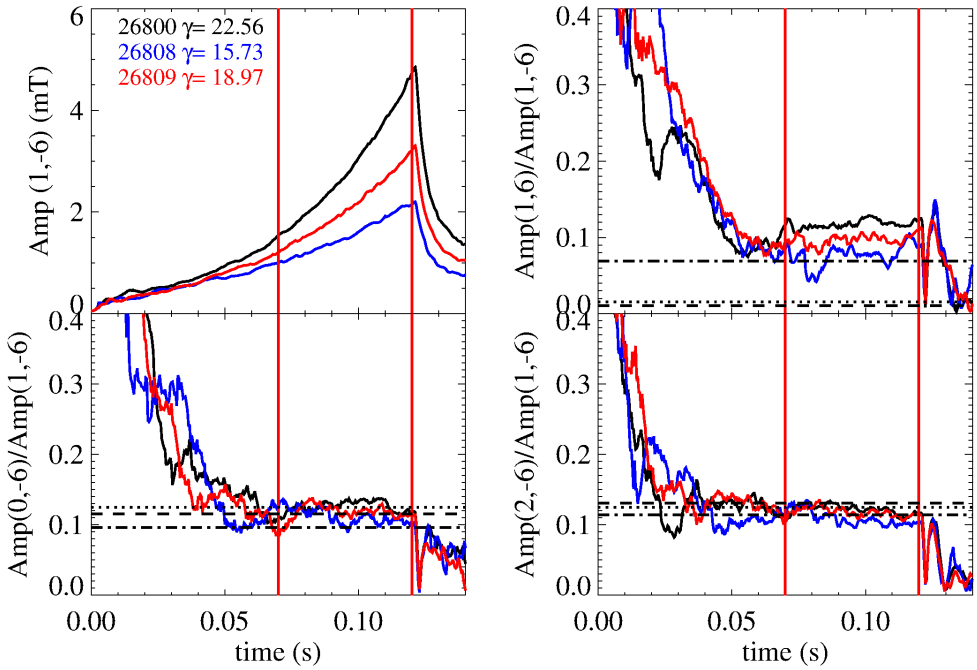

Figure 8.4: *In the top left plot the* $(1,-6)$ *amplitude as a function of time is shown in case of free growth (black), and control using sub-critical gains (red and blue). In the other plots the ratio of other* m *components over the* $(1,-6)$ *as a function of time are shown. Horizontal lines are predictions provided by the analytic calculation in toroidal geometry (dotted), by MARS-F (dashed), and by CarMa (dotted-dashed)*

other conducting structures (support structure), the simulated growth rates seem to decrease.

The benchmark of the three different codes is also useful to explain in detail the source of the coupling among different m harmonics of the same n component. The coupling can be observed in the growth rate modification of $m = -6$ components, as already pointed out, but can also be observed in the ratio of various m harmonics of $n = -6$ components with respect to the $(m = 1, n = -6)$ component. In figure 8.4 top left plot the growth of the $(m = 1, n = -6)$ components as a function of time is shown in case of free growth (black line), and $(m = 1, n = -6)$ alone controlled using sub-critical gains (red and blue). In the other plots the ratio between the other measured m components over the $(m = 1, n = -6)$ one as a function of time are shown, compared to the horizontal black lines, which are the predictions provided by the analytic calculation in toroidal geometry (dotted), by MARS-F (dashed), and by CarMa (dotted-dashed). For the three different pulses a constant ratio between the $n = -6$, different m harmonics over the $(m = 1, n = -6)$ is observed, and this ratio is also constant over time, suggesting that the phenomenon under observation is indeed linear, as the physics considered in the used codes. The three codes predictions are in good agreement among them and in agreement with experimental results for the $(m = 0, n = -6)$ and for the $(m = 2, n = -6)$ components, this means that the physics which drives the coupling for these harmonics

is common to the three predictions, and is indeed determined by the coupling due to toroidal geometry. In the case of $(m = 1, n = 6)$ the ratio over $(m = 1, n = -6)$ is systematically larger then the predictions of theory and MARS-F, while it is in good agreement with CarMa prediction, at least for the smaller growth rate cases. This means that the cause of the coupling for this harmonic is not linked exclusively to toroidal coupling anymore, but is indeed an effect that can be fully described only in a realistic 3D boundary, being predicted only by CarMa.
In figure 8.4 a spread between the different pulses is observed, and the larger growth rate cases seem to have also a larger ratio to the $(m = 1, n = -6)$ component. This can can have several causes, for instance a field component linked to the time derivative of the mode amplitude, or a paramagnetic effect of the wall response due to the copper shell intrinsic para-magnetism .

CHAPTER 9

RWM control dynamic flight simulator

Future devices design and scenario development highlight the need to predict plasma stability to MHD modes, taking into account the whole system composed by the plasma, the device structures and the optional control systems. For this reason a dynamical RWM control simulator has been developped in RFX-mod, which takes into account plasma stability, RFX-mod 3D structure and RFX-mod active control system. The three systems have been interlinked and simulated in high level detail, to be able to reproduce the effects that different control parameters have on the real experiment.
My original contribution to the work was the experimental benchmark of the simulator with RFX-mod data, including the development of dedicated experiments.

9.1 CarMa description

The CarMa code is used to model the interaction of the plasma with the surrounding conductors. The details are presented in [85] for what concerns the basic formulation and in [46] for what concerns the particularization to RFP's in general and RFX-mod in particular. Here we report only the main points. The plasma is supposed to experience small variations around a reference 2D equilibrium point, so that a linearized version of the MHD equations, with a given toroidal number n, is used to describe its evolution. The plasma mass is neglected, so that it has a static (i.e. inertia-free) response. A coupling surface S is chosen, in between the plasma and the conducting structures. The plasma response to a set of independent magnetic field perturbations over S is computed, in terms of an equivalent surface current over S producing exactly the same field as the plasma perturbation outside S. The toroidal MHD code MARS-F [84] is used to this purpose. Let V_c be the three-dimensional conducting domain circumventing the plasma, which is treated using an integral formulation of the eddy currents problem. Expressing the electric field in terms of the magnetic vector potential A and of the electric scalar potential V, and imposing Ohm's law on V_c in weak form, the following equation is obtained:

$$\int_{V_c} \eta \mathbf{J} \cdot \mathbf{w} dV + \frac{\partial}{\partial t} \int_{V_c} \mathbf{A} \cdot \mathbf{w} dV + \int_{V_c} \nabla V \cdot \mathbf{w} dV = 0 \tag{9.1}$$

where is the resistivity (which may be a tensor in anisotropic cases), J is the current density and w is a suitable weighting function. Expressing the magnetic vector potential in terms of J by the Biot-Savart integral, we obtain an integral equation in J. The electric vector potential is introduced to impose the solenoidality of J; the two-component gauge is used to recover its uniqueness. The conducting domain V_c is discretized via volumetric finite elements (no thin-shell approximation is made), and the edge elements basis functions N_k are introduced, so that:

$$\mathbf{J} = \sum_k I_k \nabla \times \mathbf{N}_k \tag{9.2}$$

the two-component gauge is conveniently imposed numerically with the so-called tree-cotree decomposition of the mesh and with a special automatic treatment for multiply connected domains [86]. Using the Galerkin method, 9.1 becomes:

$$\underline{\underline{R}}\underline{I} + \underline{\underline{L}}\frac{d\underline{I}}{dt} = -\frac{d\underline{U}}{dt} + \underline{\underline{F}}\underline{V} \tag{9.3}$$

where R, L, F are suitable matrices [85], I is the vector of degrees of freedom describing the three-dimensional current densities in conductors as in 9.2, V are the externally fed voltages and U is the interaction with the plasma, which depends linearly on the equivalent currents on S. Since such equivalent currents depend (through the linearized plasma response) on the magnetic field perturbation on S, which in turns depends linearly on the 3D currents I, in the end:

$$\underline{\underline{L}}^* \frac{d\underline{I}}{dt} + \underline{\underline{R}}\underline{I} = \underline{\underline{F}}\underline{V} \tag{9.4}$$

$$\underline{\underline{L}}^* = \underline{\underline{L}} + \underline{\underline{X}} \tag{9.5}$$

where X is a suitable matrix depending on the plasma response. It can be noticed that in 9.5 multiple toroidal mode numbers can be considered simultaneously, by simply adding different X terms, each corresponding to a different n number. This feature can be used in order to evaluate the multimodal coupling which occurs even in linear MHD due to three-dimensional conducting structures (see Section 8). In this case for simplicity only one toroidal mode number at a time will be considered. This implies no coupling between different toroidal harmonics, the assumption is valid since the studied mode is the most unstable RWM, which is not influenced in its growth by the other modes.
Conversely, due to the effect of toroidicity and the presence of gaps in the conducting structures, all the significant poloidal harmonics ($-5 < m < 5$) will be considered simultaneously. In other words, contrary to what happens in the cylindrical approximation, which is commonly used in RFP modelling, we will not consider a given (n,m) mode as evolving separately with respect to the others. For a given n number we will have a number of (eigen)modes of system 9.5, which will involve theoretically all poloidal m numbers - in practice, one or few m numbers will dominate the others. Further details can be found in the following sections.
A rather detailed description of the RFX-mod geometry is given with a suitable finite elements mesh (Fig. 9.1). In particular, the conducting shell is represented with its toroidal and poloidal gap, we call I_p the set of 2550 degrees of freedom 9.2 describing the 3D current density in the shell. All 192 independently fed active

coils are represented in the mesh, with their actual geometry, let Ia be the 192 currents in such active coils. Similarly, we represent in the mesh also the 192 saddle loops, providing the linked flux measurements m or, equivalently, the mean radial magnetic flux density over the saddle loop area, these flux loops are inside the shell, each corresponding to one active coil. Contrary to [87], neither the mechanical structure nor the vessel have been included in the mesh, in order to limit the number of discrete unknowns, hence avoiding prohibitively heavy computational loads. Indicating with the subscripts "p", "a", "m" the quantities related to the shell, the active coils and the flux loops, we have from 9.5:

$$\frac{d\underline{\Phi}_p}{dt} + \underline{\underline{R}}_{pp}(\underline{\underline{L}}^*_{pp})^{-1}(\underline{\Phi}_p - \underline{\underline{L}}^*_{pa}\underline{I}_a) \tag{9.6}$$

where:

$$\underline{\Phi}_p = \underline{\underline{L}}^*_{pp}\underline{I}_p + \underline{\underline{L}}^*_{pa}\underline{I}_a \tag{9.7}$$

$$\underline{\Phi}_m = \underline{\underline{L}}^*_{mp}\underline{I}_p + \underline{\underline{L}}^*_{ma}\underline{I}_a. \tag{9.8}$$

Assuming the 192 currents in the active coils Ia as inputs, the 192 fluxes m as outputs and the 2550 quantities p as states, with simple algebraic manipulations of 9.6 - 9.8 and obvious definitions of matrices A, B, C, D, we get the following MIMO state-space system:

$$\begin{aligned} \frac{d\underline{\Phi}_p}{dt} &= \underline{\underline{A}}\underline{\Phi}_p + \underline{\underline{B}}\underline{I}_a \\ \underline{\Phi}_m &= \underline{\underline{A}}\underline{\Phi}_p + \underline{\underline{D}}\underline{I}_a \end{aligned} \tag{9.9}$$

this model can be easily included in the block scheme of the overall control system of RFX-mod, described in details in the following section.

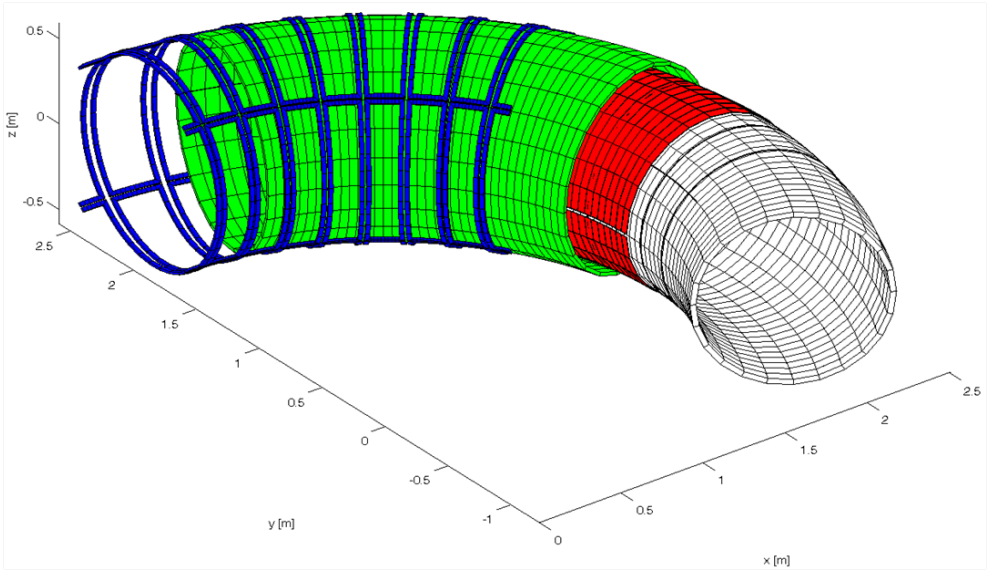

Figure 9.1: *Schematic of the 3D mesh uses in CarMa.*

9.2 Controller description

The highly flexible digital control system of RFX-mod allows to implement different control strategies of the plasma magnetic boundary. The two most important are: Virtual Shell (VS), which aims at cancelling the radial component of the magnetic field measured by the saddle probes after the removal of the $m = 1$ component corresponding to the vertical equilibrium field; and Mode Control (MC), the most used up to now, which consists in acting separately on each harmonic component of the Discrete Fourier Transform (DFT) of the same magnetic field radial component. In particular, the best experimental performances in terms of Tearing Mode Control have been achieved by implementing a slightly modified version of the latter, named Clean Mode Control (CMC) [88], which allowed the removal of the error in the measurement of the magnetic field harmonic components due to the high order poloidal and toroidal sidebands produced by the discrete grid of 4x48 saddle coils. Taking advantage of the available real time measurements of the toroidal component of the magnetic field, the cleaned harmonic components can be calculated at an inner radius, corresponding to an estimate of the actual plasma boundary. While the CMC procedure was necessary to achieve high current operation, it appeared less instrumental in the case of specific RWM control experiments.
A comprehensive block scheme is given in Figure 9.2. The plant (P) outputs are two signal arrays: the radial component of the magnetic field measured by the saddle probes (4x48) and the saddle coil currents (4x48). The raw harmonic components $B_{r,raw}{}^{mn}$, and I^{mn} are obtained by performing a 2D spatial DFT of these signals (F blocks in the scheme). The cleaned harmonic component $B_r{}^{mn}$ is then calculated as the algebraic sum of $B_{r,raw}{}^{mn}$ and the aliasing error correction term $B_r{}^{mn}$. As it was stated before, the discrete grid of active coils produces high order sidebands ($m + jM$, $n + kN$, with $M = 4$, $N = 48$, $j, k = 0, \pm1, \pm2, ..$ and $j = k \neq 0$) for each required (m, n) magnetic field harmonic. These undesired components are unavoidably included in the (m, n) harmonic calculated by DFT of the field measured by the saddle probes. On the other hand, being a copper shell interposed in between the sensors and the saddle coils, these same terms can be estimated by solving the linear diffusion equation written for each harmonic component of the magnetic field. The inputs and outputs of the corresponding linear block (C) are the coil current harmonics and the field harmonic corrections, respectively. Presently, the effect of 14 sidebands is taken into account for each harmonic ($m' = m + jM$, $n' = n + kN$, with $j = 0, \pm1, \pm2, k = 0, \acute{s}1$ excluding the case $j = k = 0$). In the block scheme of Figure 9.2, the magnetic field toroidal components which must be used to extrapolate the correction at an arbitrary inner radius are not included for simplicity.
The resulting error signal $B_{r,ref}{}^{mn} - B_r{}^{mn}$ is a complex quantity and it must be split into real and imaginary part before being processed by the actual controller (R). This is made up of 192 PID regulators, whose parameters can be independently set. In particular, as a further degree of freedom in the control action, the possibility of using complex proportional gains to introduce phase shift between input and output signal is also provided. The outputs of the two control blocks acting on the real and the imaginary part of the error signal are then recomposed

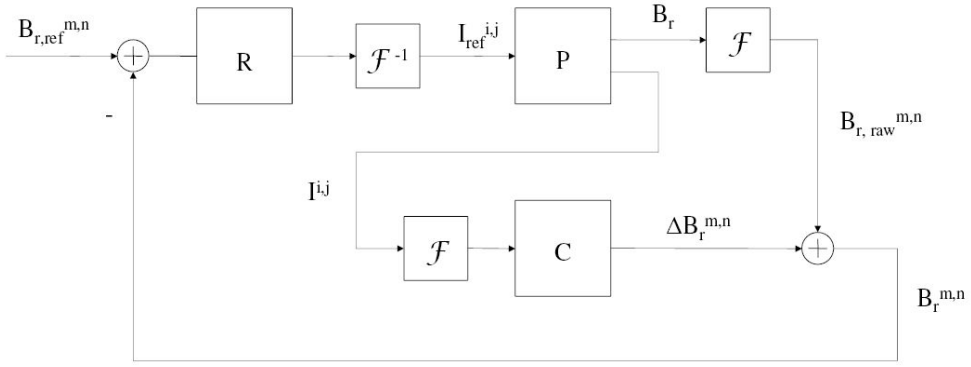

Figure 9.2: *Scheme of the control simulator with blocks representing the Plant (P), the Controller (R), the Mode Cleaner (C). Blocks performing DFT and inverse DFT are also shown.*

into a complex array, which is converted into 192 saddle coil current references by inverse DFT (F^{-1}).
Both the cleaning block and the controller block are modelled by linear dynamic systems, conveniently cast in the standard state space representation, using the parameters actually implemented in the experiment, with no tuning nor fitting parameters. The plant P is represented by the CarMa model, using the state space representation in equation 9.9 described in the previous section, again with no tuning nor fitting. A simple division by the area of the saddle loops is performed to pass from the fluxes in equation 9.9 to the average radial component of the magnetic flux density used by the controller. The dynamics of the current control loop nested inside the plant is taken into account by a single pole diagonal system with a time constant $\tau = 2ms$ in series with the CarMa model.
Eigenvalues analysis is a suitable tool to investigate the effect of different sets of controller gains on the resulting closed loop system, preliminary to more demanding simulation in time domain. On the other hand, both the control block to be series connected to the plant and the parallel connected cleaning block must be real variable linear systems. Thus some algebraic manipulation work was carried out to embed the blocks performing the direct and inverse DFT into the controller and the cleaning blocks.
Moreover, to account for the possibility of either controlling or cleaning subsets of harmonics, proper selection and filling matrices must be inserted to maintain invariant the input/output connection to the same CarMa model. Finally, considering that the DFT of an array involves the creation of complex conjugate couples, minimum dimension realization systems have been created by including the actual number of degree of freedoms of the systems. As for the cleaning block, since each sideband is represented by a state, the resulting total number of states is 14 times the number of cleaned harmonics. As for the controller, it depends on both the number of controlled harmonics and the characteristics of the regulator (full PID or simpler cases).

9.3 Model-Experiment comparison

Before exposing the results of the analyses and the comparisons, it is worth while pointing out the meaning we attribute to the terms "harmonic component" and "eigenvector/mode". We use the terms eigenvector and mode in the meaning of the linear system theory. An eigenvector v is an element of a basis which allows to express the general free evolution of a diagonalizable linear system; its associated mode is the time exponential function $e^{\lambda t}$, where λ is the corresponding eigenvalue of the state matrix (in case of complex conjugate eigenvalues $\sigma \pm i\omega$ the couple of real time functions $e^{\sigma t}cos(\omega t)$, $e^{\sigma t}sin(\omega t)$ are obtained). When a spatial interpretation of either the eigenvectors or the system outputs is possible, each mode provides the time evolution of the spatial pattern associated to the eigenvector itself or its output image. In this context λ corresponds to the λ used in Section 2.1, but multiplied by i.

In this context there is a biunique correspondence between the words mode and eigenvector, which can be considered interchangeable. The system growth rates are then obtained directly from the real part of the eigenvalue of the open/closed loop system state matrix. In our model one of the system outputs is the array of the magnetic field radial components, and the corresponding (m, n) harmonic components are obtained by calculating its 2D spatial FFT. If we consider the output image of a single eigenvector and observe its spatial pattern, it is possible to have a rough but intuitive view of its dominant harmonic content.
In a cylindrical axi-symmetric geometry a one-to one mapping can be assumed between the system eigenvectors, to which the growth rates are associated, and the harmonic components of the outputs. In a toroidal and, furthermore, non-axisymmetric geometry, this property is not true any longer and, in general, we can just highlight the dominant harmonic content of either each eigenvector or, what is more interesting, its output image. In Figure 9.3 the output arrays corresponding to the real and imaginary part of a couple of complex conjugate eigenvectors are shown. While a dominant m=1, n=-6 pattern associated to the plasma

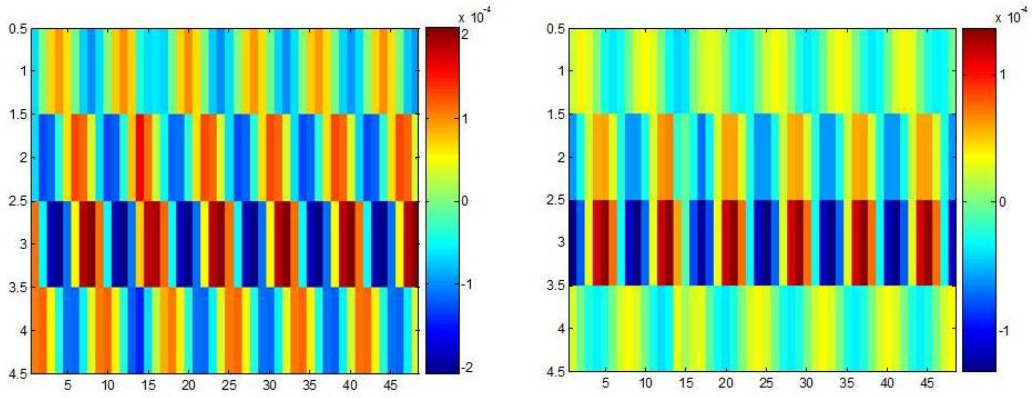

Figure 9.3: *Spatial patterns of the output arrays associated to real and imaginary part of a couple of complex conjugate eigenvectors, characterized by a dominant m=1, n=-6 armonic component. The effect of the shell toroidal cut is recognizable on the right side. Color scale is in the same arbitrary units.*

mode can be recognized on the left, the breaking of the poloidal symmetry due to the presence of the shell toroidal cut can be noticed on the right. A quantitative evaluation of this effect can be obtained by comparing the amplitude of the (m=0, 1, 2, n=-6) poloidal harmonic components, which are presented in Figures 9.4, 9.5. In conclusion, when a growth rate or an oscillating frequency, in the case of complex conjugate eigenvalues, is referred to a harmonic component of the system output, we are actually considering the growth rate of the eigenvector, whose output image is characterized by the maximum relative content in the selected harmonic.
The results from the simulator outputs were then compared with growth rates and oscillating frequencies calculated by curve fitting on the DFT of the measured experimental radial field components.

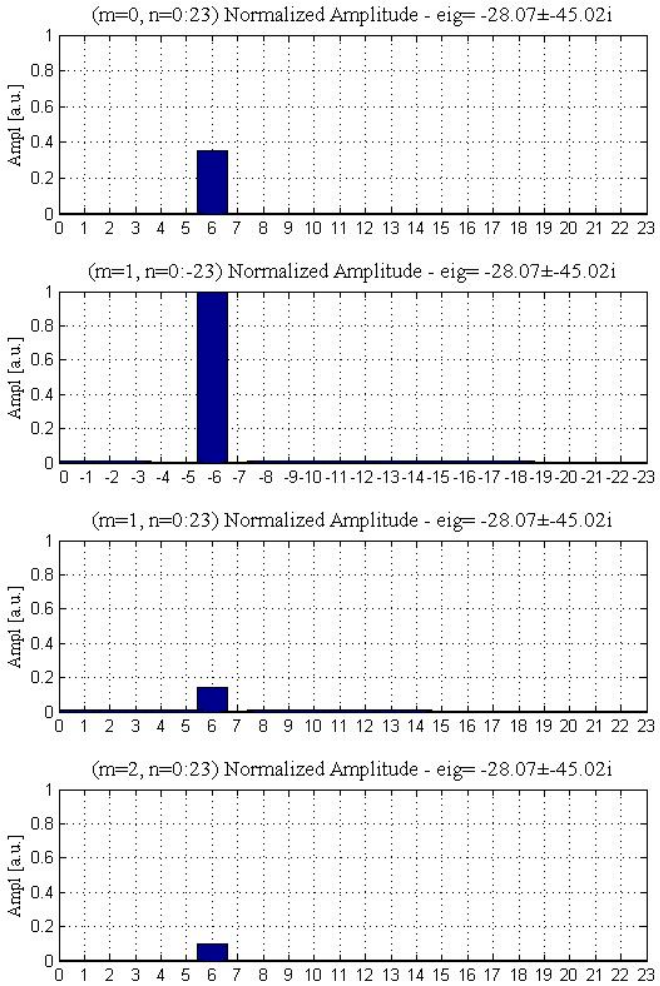

Figure 9.4: *Harmonic components of the output arrays associated to real part of the complex conjugate eigenvectors.*

To guarantee a good benchmark of the control simulator against experimental results, a refined growth rate measurement was implemented, taking into account also a possible oscillatory behaviour of the closed loop system, which linked to the imaginary part of system eigenvalues. Such an oscillation can be reconstructed from the mode DFT amplitude, which is positive by definition (black solid line in Figure 9.6), if we reverse the sign of the signal where the amplitude itself goes to zero and the phase has a π jump. After the reconstruction of the full oscillation (black dashed line) the mode signal was fitted with a nonlinear χ^2 minimization method, using a fitting function of the form:

$$B(t) = Be^{\sigma t}cos(\omega t + \phi) \tag{9.10}$$

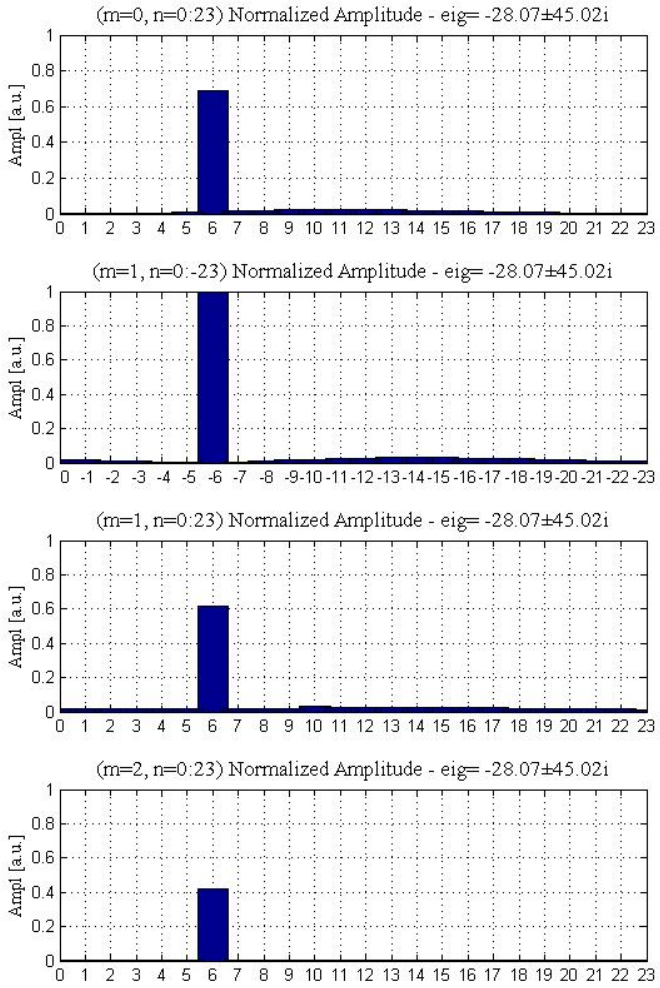

Figure 9.5: *Harmonic components of the output arrays associated to imaginary part of the complex conjugate eigenvectors.*

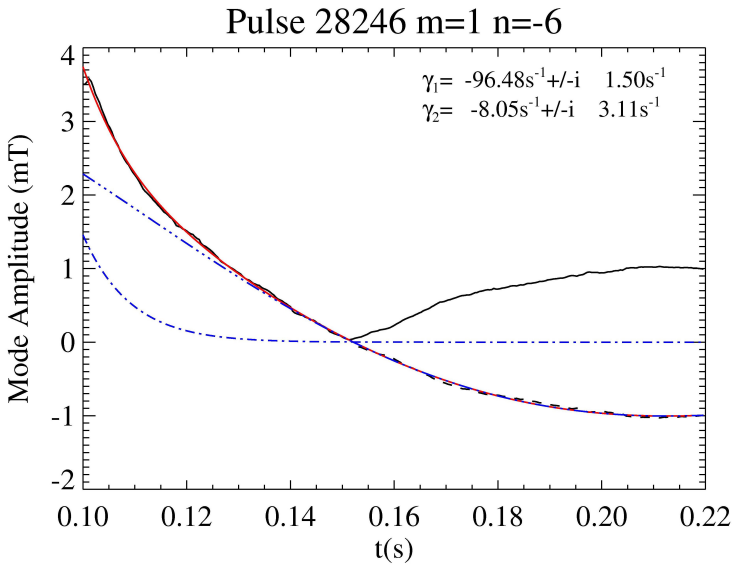

Figure 9.6: *Curve fitting on experimental data to calculate growth rate and oscillation frequency. Fast and slow modes can be detected.*

where B is an initial magnetic field value, σ is the mode growth rate, ω is the mode oscillation frequency, and ϕ is the initial oscillation phase. All of these parameters were used as free fitting parameters for the χ^2 minimization.
This function has proven to be too simple for an accurate description of closed loop system's behaviour, particularly in the first tens of milliseconds after the controller action is turned on. Indeed the evolution of a single harmonic component evidences the effect of different modes characterized by different evolution timescales.
For this reason a more refined fitting function was implemented, which is the sum of two different modes free to have different evolution timescales. The used function is:

$$B(t) = B_1 e^{\sigma_1 t} cos(\omega_1 t + \phi_1) + B_2 e^{\sigma_2 t} cos(\omega_2 t + \phi_2) \tag{9.11}$$

where the subscripts 1 and 2 refer to the two different modes.
This modified fitting function has proven to give very good accuracy in fitting experimental data, and therefore has been used as standard tool for the experimental growth rates measure. The full output of the method is shown in Figure 9.6, where the red solid line is the total fitted magnetic amplitude, while the blue dashed-single dotted and dashed-double-dotted are respectively the fitted value of fast and slow modes. In the top right corner of the plot the two complex growth rates for the two modes are reported.
For the general model-experiment comparison the slow mode values have been used in case of oscillation decay, while the fast mode values in case of oscillation growth, to capture the component which had the leading role in determining the general system behaviour.

The analyses were focused on the most important RWM in RFX-mod, which is related to m=1, n=-6 harmonic component. After validating the open loop model

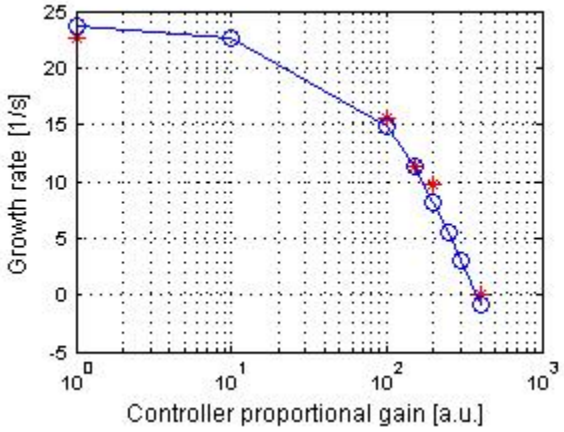

Figure 9.7: *Comparison of experimental and model growth rates with proportional controller.*

(only CarMa model), the control loop was closed by a purely proportional regulator. Eigenvalue analyses of the closed-loop system were carried out, and the results were compared with the experimentally determined growth rates. In the case of pure proportional controller, real eigevalues were found, corresponding to a purely exponential experimental time behavior. First encouraging results were presented in [89]; an increased accuracy was found refining the plasma equilibrium around which the linearization procedure was performed as shown in figure 9.7 ([90]). This figure shows the model eigenvalues (blue circles) compared to the experimentally determined exponential growth rates (red stars), as a function of the proportional controller gain. The agreement is evidently very good.

In order to verify the accuracy of the CarMa model, closed loop tests have been carried out in vacuum trying to identify the critical gain (positive feedback) with a purely proportional controller. The results have been compared with those

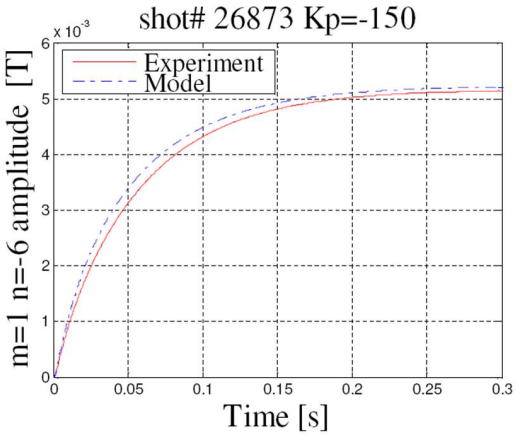

Figure 9.8: *m=1 n=-6 radial field amplitude (T) as a function of time: closed loop with* $K_p = -150$.

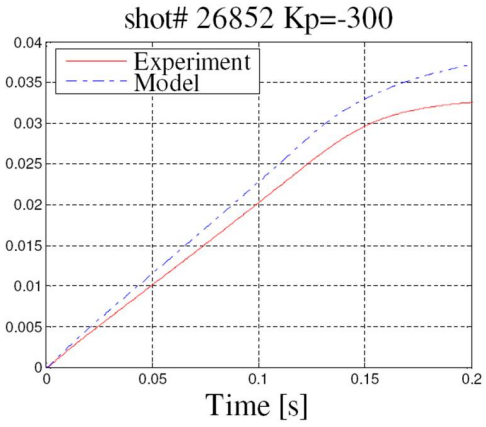

Figure 9.9: *m=1 n=-6 radial field amplitude (T) as a function of time: closed loop with* $K_p = -300$.

of the corresponding time domain simulation, as shown if Figures 9.8, 9.9, 9.10. The critical gain condition should be identified in the closed loop step response as a linear behaviour in time of the magnetic field associated to the mode. This is found clearly in Figure 9.9, where both the experiment and the model exhibit a linear behaviour, followed by a non-linear saturation phase.
The agreement between the step response of model and experiment is satisfactory in the linear regime. An increasing difference is noticed in the case of critical and overcritical gain during the saturation of the power-supplies ($t > 110ms$ for $K_p = -300$; $t > 65ms$ for $K_p = -350$).

The first time domain simulations including the plasma response were run in the case of a proportional controller. Since the evolution depends on the initial condition, before being compared, the amplitudes were normalized with respect to their maximum value and the corresponding instant was assumed as $t^* = 0$

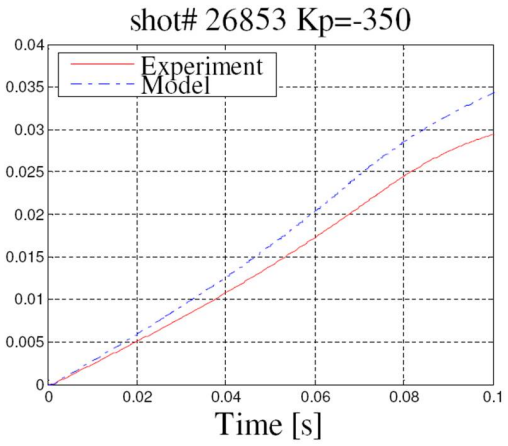

Figure 9.10: *m=1 n=-6 radial field amplitude (T) as a function of time: closed loop with* $K_p = -350$.

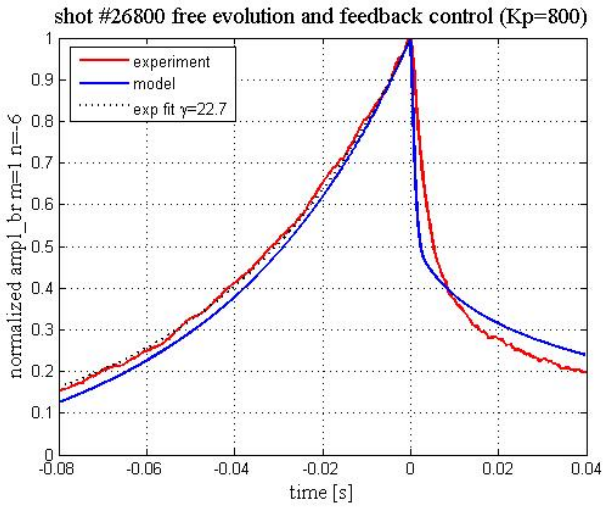

Figure 9.11: *Validation of CarMa model with plasma, m=1 n=-6 free evolution at first and then control with* $K_p = 800$.

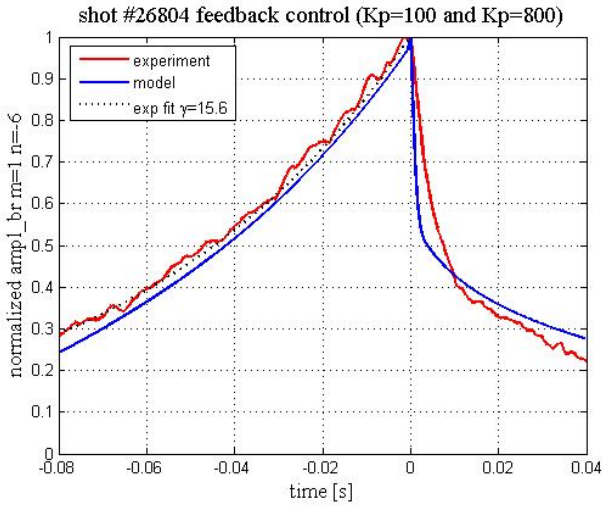

Figure 9.12: *Validation of CarMa model with plasma: m=1 n=-6 controlled with* $K_p = 100$ *at first, and then control with* $K_p = 800$.

($t^* = t - 0.12s$).
In Figure 9.11 and Figure 9.12 two examples where the proportional gain was changed during the pulse are presented. In shot 26800 the m=1, n=-6 harmonic component was let to evolve free ($K_p = 0$) and then the control loop was closed with $K_p = 800$; in shot 26804 a subcritical gain ($K_p = 100$) was first applied and then the system was stabilized with $K_p = 800$. A very good agreement is observed in the first part of the evolution, characterized by a single time constant. In the second part, the presence of two different time constants can be noticed and it is also fairly well reproduced by the model.

In order to test the model in the presence of a dynamic control system, a PI regulator of the m=1, n=-6 harmonic component was implemented. Again, eigenvalue

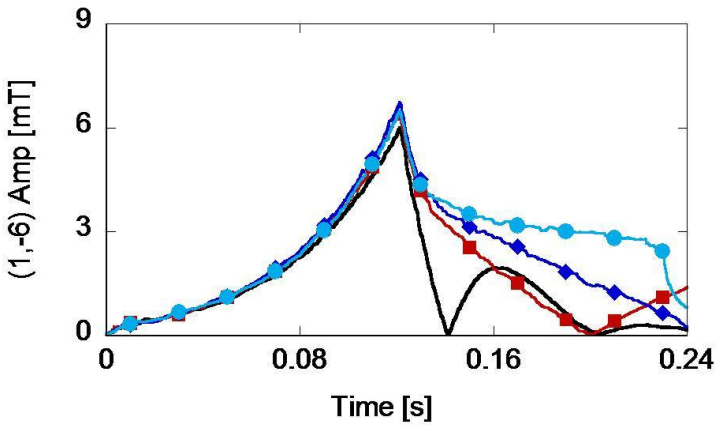

Figure 9.13: *K_i scan at constant K_p=400. K_i=40000 (black), 5000 (red), 2000 (blue), 1000 (cyan).*

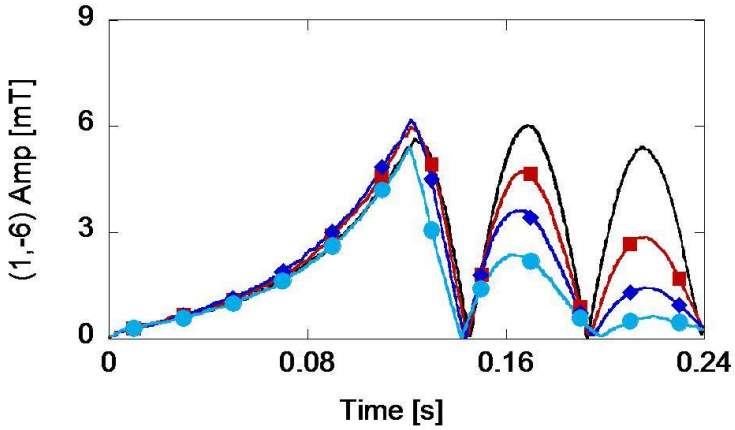

Figure 9.14: *K_p scan at constant K_i=40000. K_p=0 (black), 100 (red), 200 (blue), 400 (cyan).*

analyses of the closed-loop system were accomplished by performing an extensive scan in the proportional-integral gains K_p-K_i plane and deriving predictions on the onset of oscillatory behaviour of the m=1, n=-6 harmonic component. A significant subset of (K_p-K_i) gains was tested in a series of dedicated pulses, in particular, aimed at investigating the stability boundary curve predicted by the theoretical model.
Separate scans in K_p and K_i allowed to ascertain how the former is more effective in changing the system behaviour with a smooth transition from a purely exponential growth/decay in case of pure proportional control ($K_i = 0$), to a growing/decaying oscillation in case of large K_i. An example of this is shown in Figure 9.13, where the onset of an oscillation in the mode DFT amplitude is detected when a K_i larger than 1000 is used, and a larger K_i has the effect of increasing the oscillation frequency.
On the other hand the latter has the predominant effect of changing the growth rate (at least at a K_i value where the system is already robustly oscillating) de-

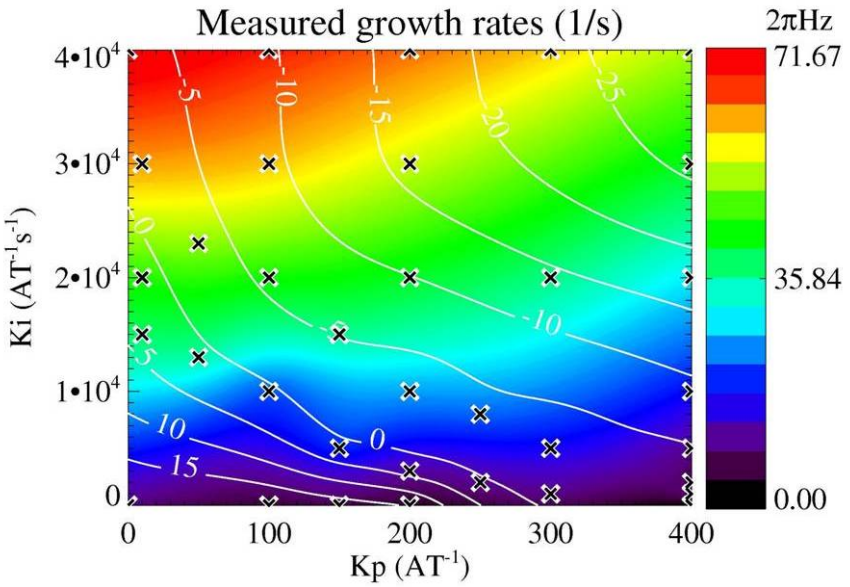

Figure 9.15: *Measured growth rates and oscillation angular frequencies in the presence of PI regulator of m=1, n=-6 harmonic component. Crosses are the K_p-K_i position of experimental data-points.*

termining the stability of the system. This can be seen in Figure 9.14, where a K_p scan has been carried out keeping a fairly large K_i. In this case the effect of a larger K_p is simply to reduce the instability growth rate (making it more negative), while keeping constant the oscillation frequency.

It is important to stress that observed oscillation frequency in the DFT amplitude

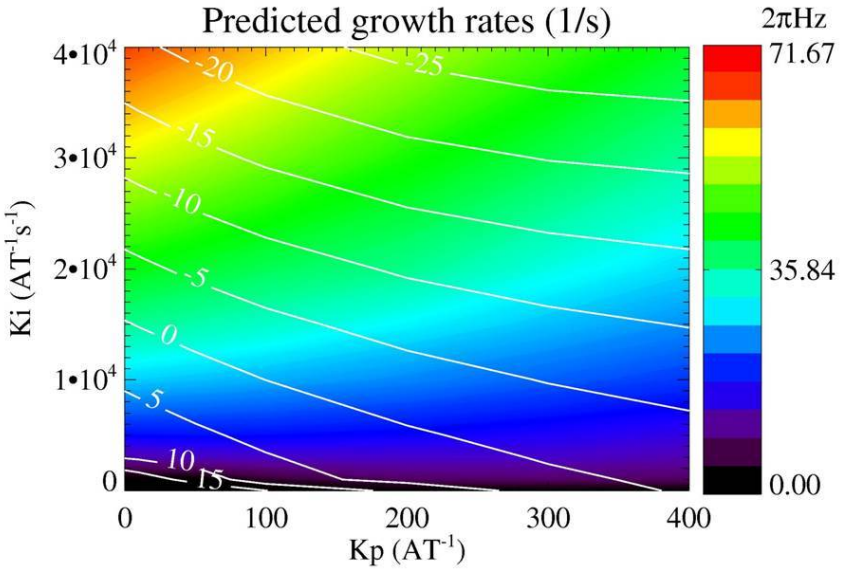

Figure 9.16: *Predicted growth rates and oscillation angular frequencies in the presence of PI regulator of m=1, n=-6 harmonic component.*

are not due to mode rotation. The argument behind this is that the DFT phase is indeed stationary all along the discharge, experiencing a π jump only when the DFT amplitude crosses zero. This means that the mode is growing wall locked, and the phase jump can be interpreted as due to an overshoot of the control action introduced by large K_i.
The results are summarized in Figures 9.15, 9.16, where growth rates are represented by contour lines and oscillation angular frequencies are represented by colour shading. A fairly good agreement is observed for $K_p > 50$ and $K_i < 30000$, while further investigations are on going for larger K_i and lower K_p. In particular, the stability boundary, dividing the stable and unstable experiments, is correctly predicted by the model in the above mentioned range of parameters.

CHAPTER 10

RWM control with reduced control hardware

In this Chapter the results of RWM control experiments using a smaller set of active coils will be exposed. My original contribution to the work was in the design and realization of the experiment, and in the data analysis as well.
Several MHD control strategies in present and future experiments rely on active coils as actuators of open loop or feedback schemes. However, in any real device active coils are finite in dimension and number, and often cover only partially the outer surface of the plasma. Under such conditions the field produced contains unwanted sideband harmonics that can be amplified by the plasma and seriously compromise the stabilization effect of the active system. In this case it can be stated that the mode produced by the control system does not coincide with the plasma mode, meaning that their descriptions in terms of Fourier 2D harmonics do not coincide. On the other hand, if the unstable modes behave as non-rigid objects, insufficient coil number or extension could make the control effort fruitless.
The mode rigidity issue is an emerging topic in RWM control, and it is tightly linked to the effect of control on the mode. The mode is non rigid if it reacts to the control action producing several further m and n unstable harmonics, which usually can not be addressed by the controller. On the other hand if the control on a single (m,n) harmonic is sufficient to stabilize the mode completely, than it is said to be rigid [74].
Given obvious limitations on changing active coil hardware on the same machine, many of existing studies can only compare the effect of different coil configurations on different machines.
For this reason some experimental sessions on RFX-mod were dedicated in the last years to the issue of downgrading the active control system, to get to a proper limit in the coil configuration, under which the control was impossible.
The first attempts to downgrade the systems were focused on reducing the number of coils while still keeping the full coverage of the torus surface. The downgrade was carried out in the coil space, i.e. averaging the control current references of neighboring coils after the control cycle, to mimic the action of larger coils covering the surface of 2 or more actual coils.

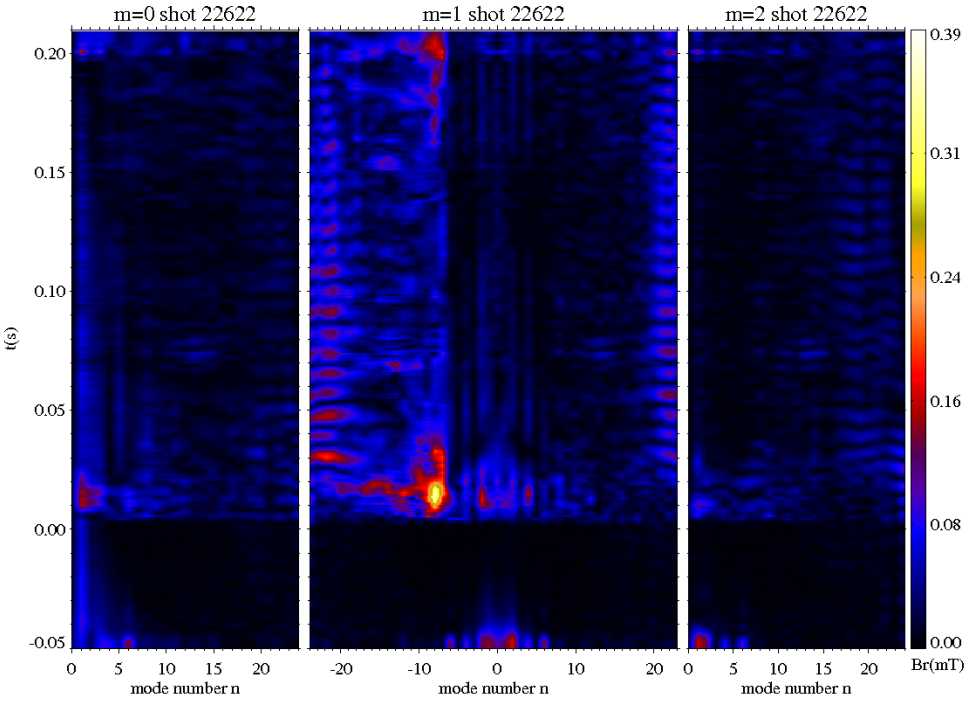

Figure 10.1: *Temporal evolution of all of the controlled components of radial magnetic field in a case of normal control.*

In Figure 10.1 the time evolution of all of the controlled radial magnetic field components is shown for a discharge controlled with the usual control settings. As it can be seen quite clearly, the largest radial field component is the m=1 n=-7, which on RFX-mode is linked to the most internal (radially) saturated tearing mode. This mode grows fast in the plasma ramp up phase, but it is controlled easily 40ms after the beginning of the discharge. No mode evidence is seen in the positive n of the m=1 spectrum.

On the other hand when the 48(toroidally)×2(poloidally) downgraded system is used, the effect on the magnetic boundary is catastrophic: the m=1 n=-7 mode grows in time until 0.08s, when the discharge terminates abruptly because of the large plasma-wall interaction produced by the mode. Furthermore with only two coils in poloidal direction, the ability to produce different field components with positive and negative m is lost. This can be seen in the right positive n part of the m=1 spectrum, where a symmetric pattern with respect to the negative n spectrum is present, with a small delay of 5-10ms. In fact the magnetic field measured in the positive n spectrum is simply an error field produced by the control system in response to the control of negative n spectrum, with the 5-10ms delay typical of the control system.

During these experiments the tearing modes in RFX-mod seemed impossible to control with a reduced coils set, and this always led to an early termination of the discharge. For this reason a novel approach to the study of control with active coils was recently developed in RFX-mod, and the results will form the main part in this section: the 192 active coil system described in section 7.1 can be flexibly

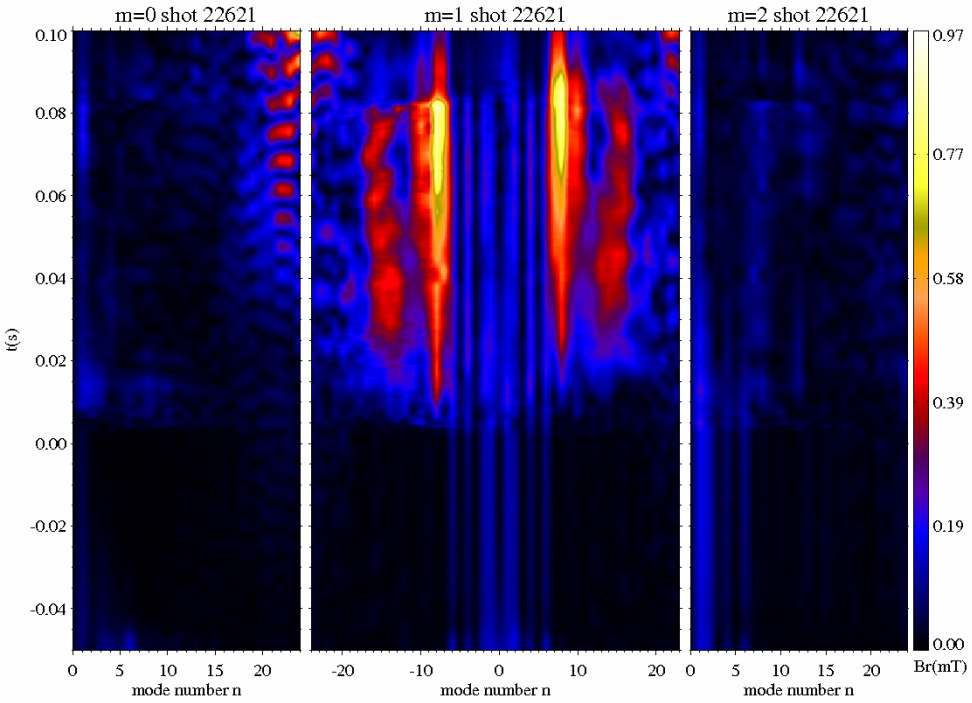

Figure 10.2: *Temporal evolution of all of the controlled components of radial magnetic field in a case of 48x2 coils (top-bottom, in-out averaged).*

downgraded by the software control in number or space resolution. In this way it is possible for the first time to easily compare the action of many different coil configurations on the same machine and on the same plasma. What is even more important, the real time software can act only on a subset of selected modes with the reduced set of coils, while all the remaining field errors and MHD instabilities are controlled with full system capabilities. This is done in order to work with optimized background plasma and to decouple the problem of discharge optimization and tearing mode control from the one of specific active MHD control, as sketched in Figure 10.3.
In RFX-mod the actuators are controlled by a full PID digital controller. The controller elaborates the actuator waveforms according to the control scheme decided by the operator. As shown in Figure 10.4 the control elaboration is normally done in the Fourier space (mode control) and then the final current references for the 192 power amplifiers are calculated via an inverse Fourier transform.
The new control capability is implemented by adding to each control cycle a further loop that separates in the Fourier space the harmonics that undergo a standard control from the ones that will be controlled by a reconfigured system. The second set of modal current references is converted in 192 real space current references and in this way it is very easy for example to zero some references before the final inverse Fourier transform, in order to mimic a control system with a smaller number of actuators.

The last step of the new control software is to sum back in the real space the standard and the reconfigured references and send the sum to each power supply.

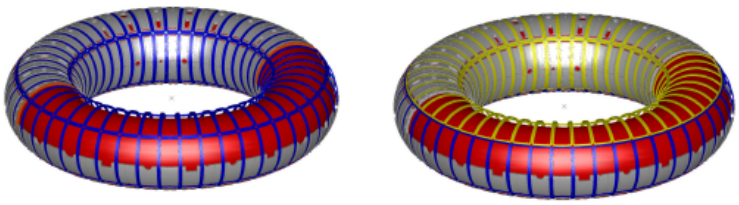

Figure 10.3: *Full control system (left) acts on the background plasma while, on the same discharge, a reduced set of coils (right) controls a selected harmonics. Blue represent active coils (standard control part), while yellow represents coils non active in the downgraded control part.*

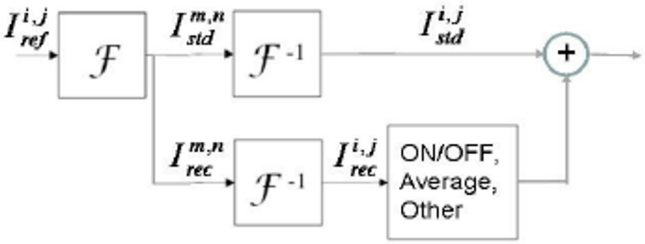

Figure 10.4: *Architecture of the software block for reconfiguration experiments.*

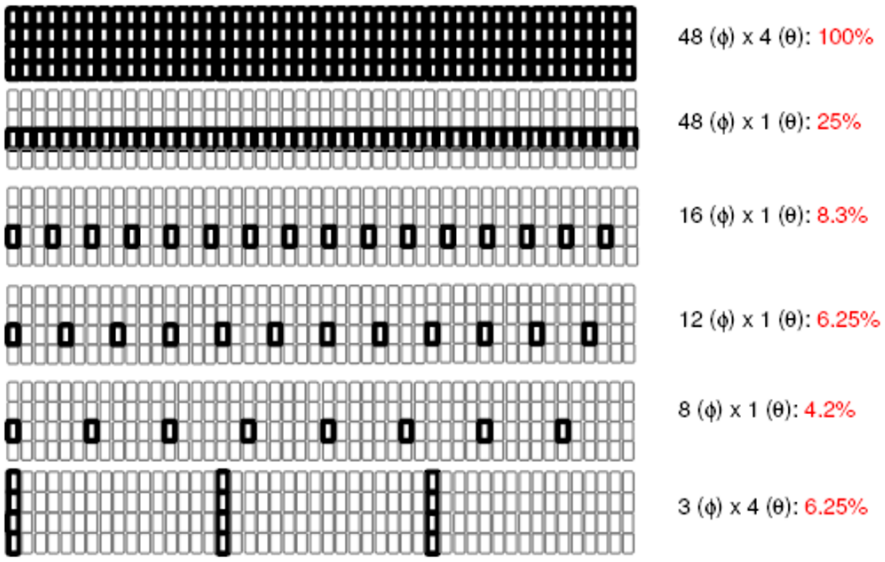

Figure 10.5: *Some of the new control configurations made possible by the software algorithm. On the right hand side the number of toroidal times poloidal coils active is summarized together with the surface covered by active coils. The representation is rectified: the vertical direction stands for the poloidal one, while the horizontal direction stands for the toroidal one.*

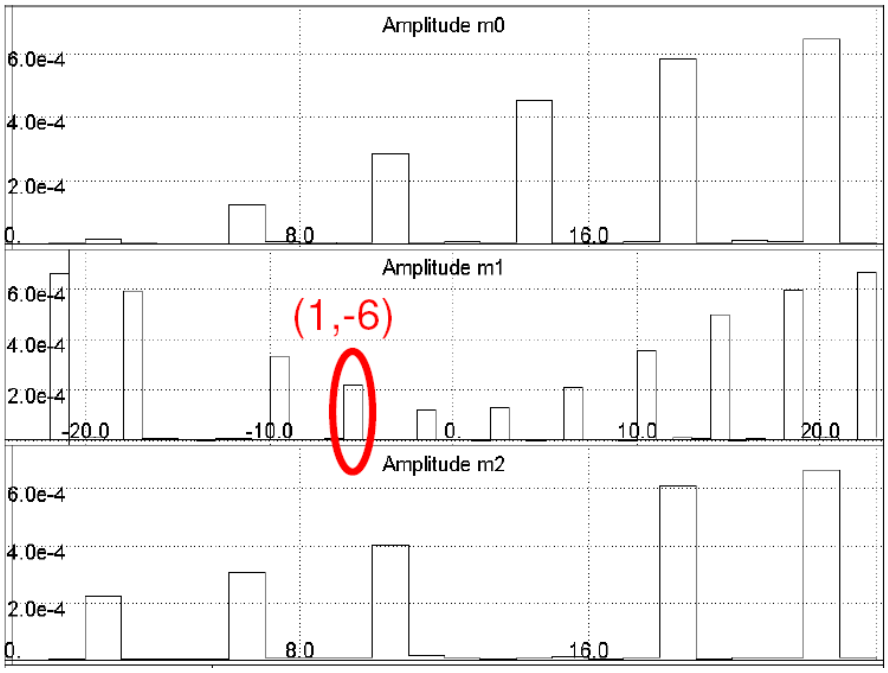

Figure 10.6: *Measured B_r harmonics produced for a pure static $(1, -6)$ harmonic request in the 8x1 configuration (vacuum experiment).*

It is important to notice that, thanks to the high optimization of the FFT and FFT^{-1} algorithms in the control software, the new loop did not affect the overall duty cycle time that remains below 0.5 ms. Figure 10.4 illustrates this procedure, while in Figure 10.5 some examples of realized reconfigurations are shown together with the total surface covered by each configuration.
The first set of experiments was carried out in vacuum to compare the harmonic content of different coil configurations trying to follow the same control request (in both open and closed loop).
As expected, when the number of active coils is decreased, the Fourier spectrum of the system action is becoming less and less pure. Measurements are always performed by the full system of 48x4 saddle coil sensors located between the vacuum vessel and the shell.
In figure 10.6 the measured field produced by a 8x1 configuration is shown; note that the requested waveform was a single, constant $(1, -6)$ harmonic, while all the remaining measured components are due to the finite size of the coils and to the aliasing in space of the external field. These results can be compared to the ones routinely obtained with the full system where the high precision of the externally produced field is clear [91].

To test reconfigured control in plasma experiments under reproducible conditions, it was decided to apply the reconfiguration algorithm to the control of one or more unstable Resistive Wall Mode harmonics. First of all the effect of the reconfiguration on a plasma discharge can be seen in Figure 10.7, where the FFT phase and amplitude in toroidal direction of the control coils currents are shown, grouped in the 4 different toroidal arrays which all have a different poloidal angle

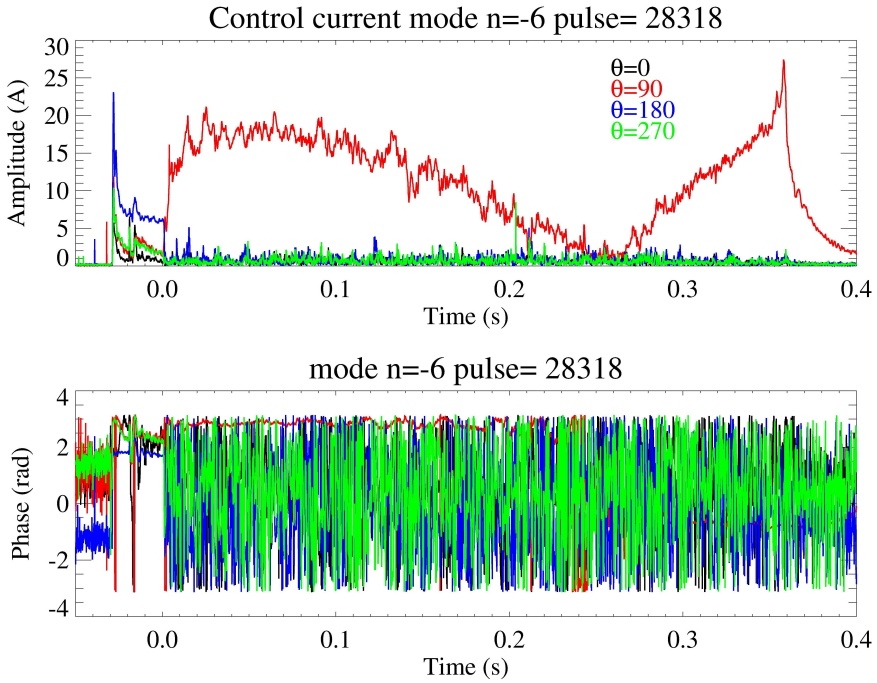

Figure 10.7: *$n = -6$ control coils currents in the 8x1 configuration, grouped in toroidal arrays.*

ϑ (top, bottom, internal, external). Only the top toroidal array is active, as expected. Non zero currents can be seen in all of the arrays between -0.3s and 0s, these currents are due to the coupling between the poloidal field winding and the saddle coils, and are induced during the charge of the poloidal field winding.
Tests of single and multiple unstable RWM feedback control with reduced active coil coverage as shown in Figure 10.5 were executed, giving encouraging results. The effectiveness of the control resulted to be conserved even in the most reduced configuration, at the price of using feedback gains one order of magnitude larger, and therefore risking current saturation in the control coils. The enhancement of gains led also to larger dynamic effects during the transients when control was switched on, and control of finite amplitude modes was requested.
This effect was studied in the 8x1 configuration (the fifth from top in Figure 10.5), performing a timing scan in the control switch on: the m=1 n=-6 (1,-6) RWM was let free of control from the beginning of the discharge, then after some time the control was turned on and the control effect was documented. As a matter of fact the timing scan can be translated into a mode amplitude scan, since the mode was unstable and growing in a very reproducible way.
The experiment result is shown in 10.8, where in the upper box the plasma current is shown, in the mid box the (1,-6) harmonic amplitude is plotted as function of time, and in the lower box the (1,22) harmonic is plotted as a function of time, which is the largest unwanted control sideband for this configuration, as seen in Figure 10.6. The colours refer to a different control timing, as highlighted in the upper box and confirmed by the mid box amplitudes. In the central plot the effect of the control on the (1,-6) harmonic is shown, in all the presented cases the mag-

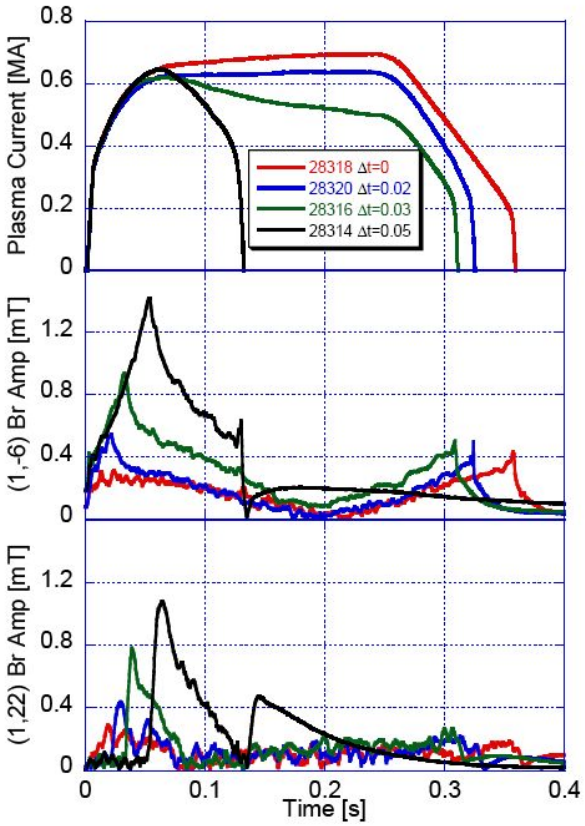

Figure 10.8: *Control switch on timing scan in 8x1 configuration. In the top plot the current evolution is shown, in the mid plot the (1,-6) evolution is shown, in the bottom plot the (1,22) is shown.*

netic amplitude was controlled effectively, even if the tendency to an oscillating behaviour can be guessed since the amplitude goes to zero at about 0.2s, and then grows again.

Nevertheless the overall effect on the discharge is very different in the four cases: the later the control switch on was, and therefore the larger the mode amplitude at that time, the worse the effect on the discharge, as can be noticed in the plasma current evolution in the upper plot. The explanation is contained in the bottom plot where the amplitude of the (1,22) harmonic is shown, which is usually a robustly stable harmonic in all of the possible plasma configurations in RFX-mod. This field harmonic stayed close to zero until no control on (1,-6) harmonic was exerted, and at the switch on time a very fast transient growth was observed in all of the four cases. The maximum amplitude of this transient scaled with the controlled mode amplitude, and in the worst case it led to a fast plasma termination (black line).

The origin of this large error field, that in some cases can become larger than the controller mode itself, is the presence of sideband harmonics, which are introduced by the fact that the used coils are very few and also very localized spatially (see Figure 10.6, where the same coils configuration is used in a vacuum test pulse).

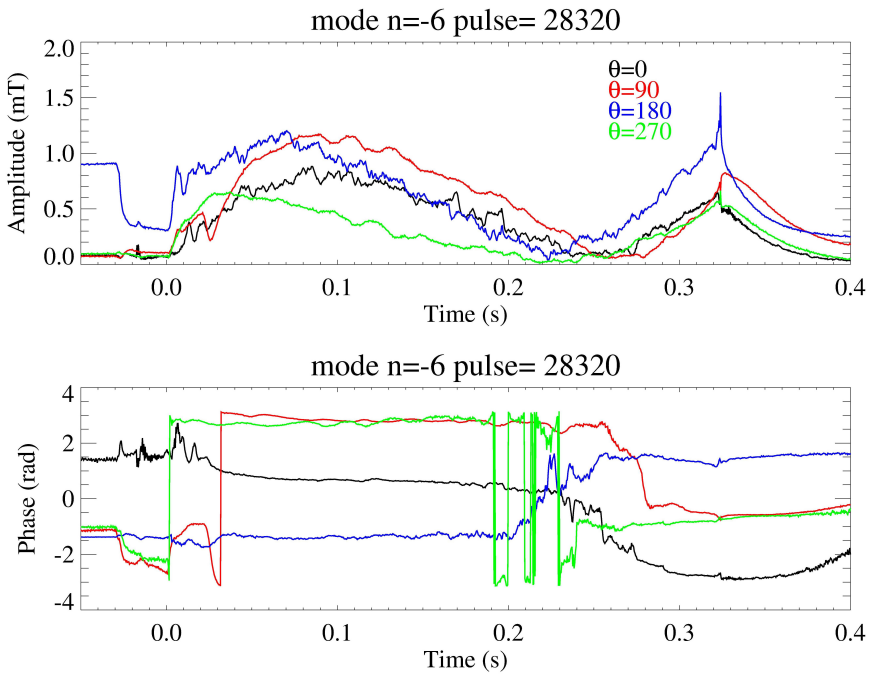

Figure 10.9: *n=-6 radial field in the 8x1 configuration, grouped in toroidal arrays.*

In this case one of these sidebands has been shown, but also several others are present, depending on coils number and shape and on the m and n numbers of the controlled mode. Most of the control action is therefore dispersed in the unwanted production of these error fields.
The same analysis shown in Figure 10.7 can be carried out for radial fields sensors, as shown in Figure 10.9. First of all it can be noticed that the field in the upper array (red) is considerably larger than the one in the bottom array (green), as it could be expected since the bottom array is in opposite poloidal position with respect to the only coils array active. The surprise is that the two fields are in phase for the major part of the discharge, this means that large even m harmonics are produced, which are not present in the normal control configuration.

The other interesting information is that the time response of the different arrays is not the same at all, the field evolution seems to be slightly ahead in the two equatorial arrays (blue and black), then comes the bottom array and the last is the top one. This means that even though the top array (red) is the only one active, the field it produces penetrates faster in the equatorial arrays, which both face a cut in the stabilizing shell (blue) and in the support structure (black). Therefore the cuts and holes in the conducting structures near the plasma and near the coils might be of large importance if a very fast feedback response is needed.
In Figure 10.10 an example is shown for the 12x1 configuration where, due to the specific mode periodicities, evenly spaced coils were not able to stabilize the mode: in fact during the control the (1,-6) mode changed its phase in order to place amplitude nodes over the active control position (blue lines), this implied that the mode could grow undisturbed in the space between the active coils, which were

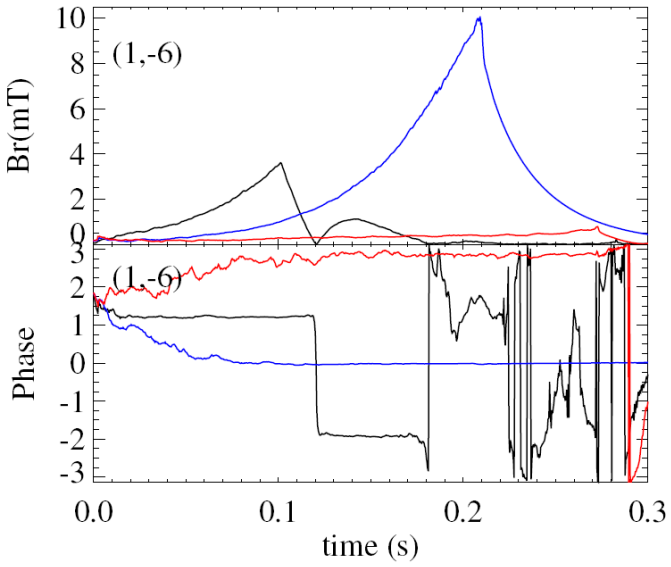

Figure 10.10: *control experiments with full system (black, control on from 0.1s), and downgraded 12x1 (blue for evenly spaced coils and red for unevenly spaced ones).*

producing a null radial field, since in front of them the plasma displacement was zero. This picture is sketched in Figure 10.11.
Effective control could be recovered without increasing the number of active coils, but simply by using an uneven coil distribution (red lines), in fact removing the toroidal symmetry no simple harmonic could find a toroidal position where it could grow between active coils, as sketched in Figure 10.12 . In this case the mode behaved as a rigid object: the first movement was simply a rigid movement maintaining the 3D mode structure, if the coils are rearranged unevenly this movement is not sufficient to escape the control action, and the control in few localized zones can reduce mode amplitude rigidly everywhere.
After the successful control of a single RWM with the reconfigured set of coils, the simultaneous control of multiple RWM harmonics with 8x1 configuration was tried on the following harmonics m=1,n=-4,-5,-6. The result of the experiment is shown in Figure 10.13, where the mode phase and amplitude against time are plotted for the mentioned harmonics. The control proved to be partially effective, in fact modes m=1,n=-5,-6 were stabilized completely, while the m=1,n=-4 was

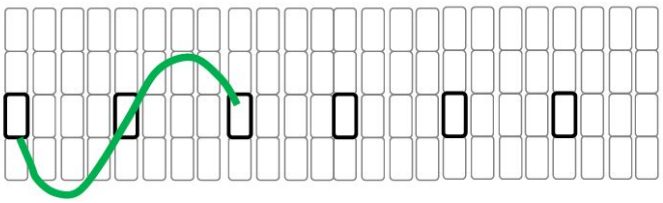

Figure 10.11: *Sketch of m=1 n=-6 mode controlled with 12x1 even configuration. Half of the torus is plotted.*

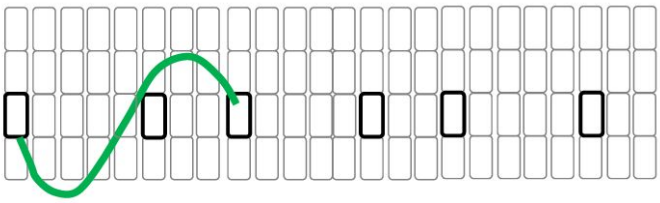

Figure 10.12: *Sketch of m=1 n=-6 mode controlled with 12x1 uneven configuration. Half of the torus is plotted.*

growing as if not controlled at all. Again for this mode a mechanism as the one described in the previous paragraph was recognized: a mode with 4 periods cannot be controlled by a set of 8 equally spaced control coils, without the mode moving toroidally and grow in the gaps between the coils.

Another interesting phenomenon which was observed during reduced control study was the Resonant Field Amplification of error fields produced by the control sidebands. The experimental observation of this effect happened when also many other field harmonics were not controlled, to avoid that the full control on all harmonics but (1,-6) could in turn control the sidebands produced by the reconfiguration on (1,-6) harmonic. The effect is shown in Figure 10.14, where the time evolution of the amplitude of several controlled RWM harmonics are shown in the left plot, while the evolution of normally stable harmonics is shown in the right plot. In this case the control was performed using the 8x1 configuration on the (m=1,n=-4,-5,-6) RWMs, and the control was switched on after 30ms of free

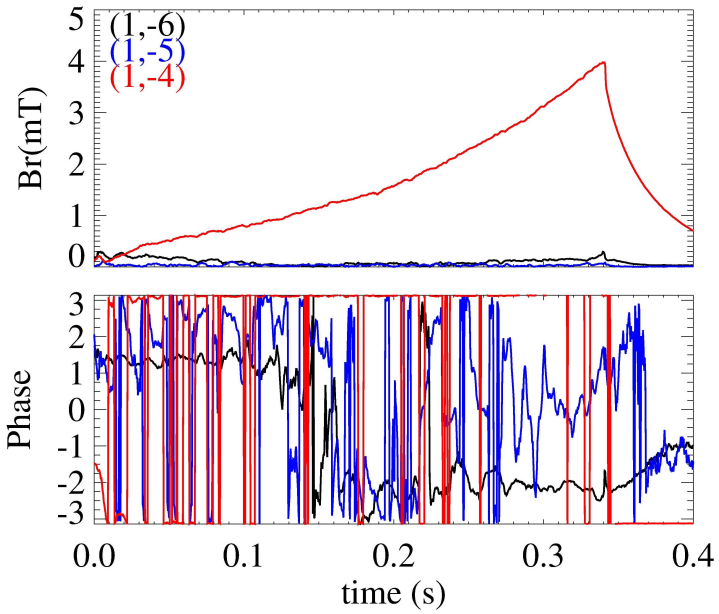

Figure 10.13: *Active control of multiple unstable RWM components in the 8x1 configuration. In the top plot FFT amplitudes are shown, in the bottom plot FFT phases are shown.*

growth.
As it can be seen all of these modes are well controlled, but after the control is switched on the (m=1, n=3) harmonic grows to an amplitude larger than the main (1,-6) mode. The difference with respect to what observed in Figure 10.8 is that the mode growth is not directly linked to a control transient, it is instead continuously growing until the end of the discharge.

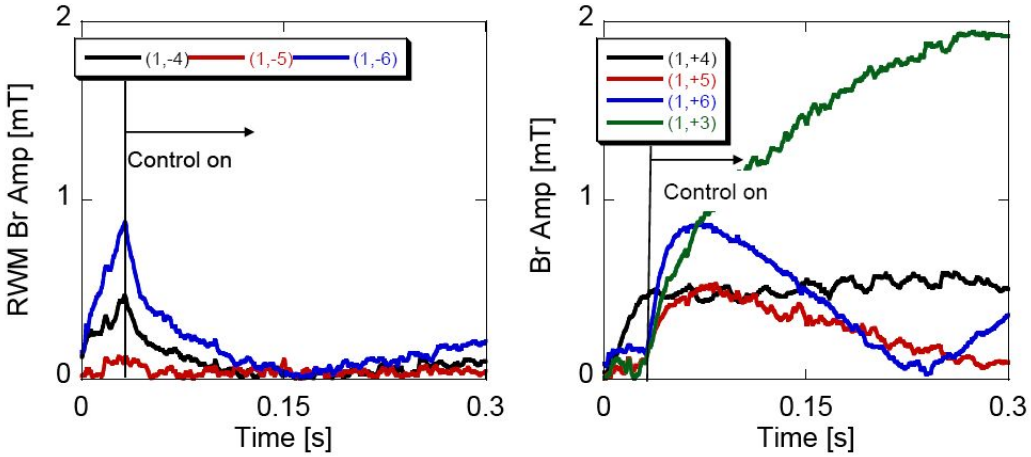

Figure 10.14: *On the left plot the time evolution of controlled RWM harmonics is shown, while on the right plot non controlled RWM harmonics are shown.*

CHAPTER 11

Conclusions

In this thesis a general class of issues has been addressed. These issues are related to the link between the physics of macroscopic MHD instabilities, and their impact on the performance of fusion devices, including possible ways of controlling them. For this reason the thesis work was carried out on two different devices, having different magnetic configurations. Also different approaches were followed for the studied instabilities.
Despite this diversity, the work is unified by a particular focus on the three-dimensional detail of mode structure. This aspect has been studied both on NTMs at JET and RWMs at RFX-mod. In the NTM case the presence of a secondary kink harmonic with an m+1 component has been highlighted. The radial and poloidal structure of the mode, and the effect of this double m structure on plasma flow rotation has been documented in Chapter 4.
In the RFX-mod case the presence of a RWM spectrum composed of several m components has been demonstrated in Chapter 8. This effect is due to a coupling between different m components of the magnetic spectrum introduced by the 3D pattern of eddy currents in the conductive structures around the plasma. The coupling was demonstrated using a careful comparison between 1D, 2D and 3D codes, the last being the only one capable of predicting the effect completely.
The approach to problems has been in many cases as complete as possible, including the inspection of single cases and studies carried out on statistical bases. For example, this has been carried out in JET with the creation of a database for the comparison of NTM localization techniques and current profile measurements (Chapter 3), and in RFX-mod, where a RWM growth rate database as a function a plasma parameters has been built (Chapter 7). Also comparison of experimental results with modelling has been carried out where possible, from the simple ad-hoc modelling of the electron temperature oscillations introduced by NTMs (Chapter 4), and the RWM growth rate benchmark with complex stability codes (Chapter 8).
Emphasis has been put on what effect the NTM modes studied had on the plasma discharge. For JET plasmas the impact of the mode on confinement has been quantified as a function of mode radial localization, as shown in Chapter 5, and for q=2 fishbones in Chapter 6, where the tendency to trigger disruptions and

continuous kink instabilities was shown.
The active control system present in RFX-mod has been used to design experiments aimed at understanding the mode physics, as implemented for the determination of RWM 3D spectrum in Chapter 8, and also to characterize the controlled system closed loop response in Chapter 9, which was used for the development and benchmark of the first RWM control dynamic flight simulator.
The control flexibility has also been used for the first time to characterize the control action dependence on the number of active coils, on the torus surface covered, or on the coils position, as shown in Chapter 10. The full unreduced measurement system permitted an optimization of coil reduction, to reach the most effective configuration in the stabilization of selected modes.
Original contributions have been brought in to all of the presented topics, but only the work in Section 3.2, Chapter 4 and Chapter 7 has been carried out completely by myself. Most of the analyses shown are the result of effective team effort, in which my skills were integrated and kept available to a large analysis team. All of the analyses shown contributed to the mainstream background of their scientific field, in fact all of them have or will lead to journal publications.
The scientific topics touched in this thesis still leave room for additional work to be completed and to expand the current picture. In the JET case a statistical analysis of the impact of the secondary m component of NTMs on plasma rotation could be the way to assess the effect of the multi m structure found in such plasma discharges.
Some more work could be carried out in the q=2 fishbone topic as well. The missing piece of information is the condition that discriminates between benign simple events, which grow and decay afterwards, and more troublesome events that trigger large ELMs. These events are always dangerous for the discharge, as they can cause major modification of thermal profiles, and also disruptions. The calculation of no-wall β limit using thermal and magnetic profiles in the time frame previous to the event could give important information for the understanding of the ELM triggering mechanism.
Other experiments could be carried out on RFX-mod as well, which could combine work on RWMs carried out in parallel on tokamak and RFP devices. In fact RFX-mod has the unique possibility of operating both in RFP and tokamak configurations, though at low plasma current (150KA). This could give the opportunity to study RWM physics in two different configurations, but with the same magnetic boundary, which is very important to characterize the wall stabilization effect.
In particular the active control downgrading study shown in Chapter 10 could be exploited on experiments in tokamak configuration, because they would extend the results obtained in the RFP configuration to the most used magnetic configuration in present fusion devices, which could never reach the large torus surface coverage and flexibility of RFX-mod control system for space reasons. These experiments have already been proposed for the 2010 RFX-mod campaign.
In general I believe that advances in understanding MHD limiting instabilities and improvements in techniques for their active control will greatly contribute to bring closer the day when fusion energy will be a reality for mankind.

Bibliography

[1] Baruzzo M et al. *Plasma Phys. contr. Fusion*, 52:075001, 2010.

[2] Baruzzo M et al. *Submitted to Nucl. Fusion*, 2011.

[3] Freidberg J. P. *Ideal Magnetohydrodynamics*. Plenum press, 1987.

[4] Wesson J. *Tokamaks*. Oxford Science Pubblication, 1987.

[5] Troyon F et al. *Plasma Phys. contr. Fusion*, 26:209, 1984.

[6] Chu M S and Okabayashi M. *Plasma Phys. contr. Fusion*, 52:123001, 2010.

[7] Freidberg J. P. *Plasma Physics and Fusion Energy*. Cambridge University press, 2007.

[8] Wagner F et al. *Phys. Rev. Lett.*, 49:1408, 1982.

[9] Taylor R J et al. *Phys. Rev. Lett.*, 63:21, 1989.

[10] Itoh K Itoh S. *Phys. Rev. Lett.*, 60:2276, 1988.

[11] Kardaun O. *Plasma Phys. contr. Fusion*, 41:429, 1999.

[12] Greenfield C M et al. *Plasma Phys. contr. Fusion*, 46:B213–B233, 2004.

[13] Joffrin E. *Plasma Phys. contr. Fusion*, 49:B626–B649, 2007.

[14] Chang Z et al. *Phys. Rev. Lett.*, 74:4663, 1995.

[15] La Haye R J et al. *Phys. Plasmas*, 10:3644, 2003.

[16] La Haye R J. *Phys. Plasmas*, 13:055501, 2006.

[17] Sauter O et al. *Plasma Phys. contr. Fusion*, 44:1999, 2002.

[18] Buttery R et al. *Nucl. Fusion*, 43:69, 2003.

[19] R. Fitzpatrick. *Phys. Plasmas*, 9:34:59, 2002.

[20] La Haye R J et al. *Phys. Plasmas*, 7:3349, 2000.

[21] Fitzpatrick R and Waelbroeck F L. *Phys. Plasmas*, 15:012502, 2008.

[22] Lazzaro E. *Phys. Plasmas*, 16:092504, 2009.

[23] Graves J P et al. *Phys. Rev. Lett.*, 102:065005, 2009.

[24] Gunter S et al. *Nucl. Fusion*, 44:524, 2004.

[25] Maraschek M et al. *Phys. Rev. Lett.*, 98:025005, 2007.

[26] Gimblett C. G. et al. *Nucl. Fusion*, 26:617, 1989.

[27] Hender T. C. et al. *Nucl. Fusion*, 29:1279, 1989.

[28] Freidberg J. P. Guo S. C. and Nachtrieb R. *Phys. Plasmas*, 6:3868, 1999.

[29] Strait E. J. et al. *Phys. Rev. Lett.*, 74:2483, 1995.

[30] Garofalo A. M. et al. *Phys. Rev. Lett.*, 82:3811, 1999.

[31] In Y et al. *Nucl. Fusion*, 50:042001, 2010.

[32] Alper B. *Phys. Fluids B*, 2:1338, 1990.

[33] Z.R. Wang et al. *Phys. Plasmas*, 17:052501, 2010.

[34] Garofalo A. M. et al. *Nucl. Fusion*, 38:1029, 1998.

[35] Bondeson A. and Ward D.J. *Phys. Rev. Lett.*, 72:2709, 1994.

[36] Takechi M et al. *Phys. Rev. Lett.*, 98:055001, 2007.

[37] Reimerdes H et al. *Phys. Rev. Lett.*, 98:055002, 2007.

[38] Berkery J W et al. *Phys. Rev. Lett.*, 104:035003, 2010.

[39] Liu Y et al. *Phys. Plasmas*, 15:112505, 2008.

[40] Chapman I et al. *Plasma Phys. contr. Fusion*, 51:055015, 2009.

[41] Sabbagh S. A. et al. *Phys. Rev. Lett.*, 97:045004, 2006.

[42] Brunsell P. R. et al. *Plasma Phys. contr. Fusion*, 47:B25, 2005.

[43] Boozer A. H. *Phys. Rev. Lett.*, 86:5059, 2001.

[44] T. Bolzonella et al. *Phys. Rev. Lett.*, 101:165003, 2008.

[45] V Igochine et al. *Plasma Phys. contr. Fusion*, 51:055008, 2009.

[46] F. Villone et al. *Phys. Rev. Lett.*, 100:255005, 2008.

[47] Bialek J., Navratil G., Katsuro-Hopkins O., and Mauel M. In *APS Meeting Abstracts*, page 1138P, 2004.

[48] Merkel P. et a. In *21st IAEA Fusion Energy Conference*, pages TH/P3–8, 2006.

[49] Gregoratto D et al. *Phys. Plasmas*, 12:092510, 2005.

[50] Reimerdes H et al. *Phys. Rev. Lett.*, 93:135002, 2004.

[51] Chen F. F. *Introduction to Plasma Physics and Controlled Fusion.* Plenum press, 1983.

[52] Coppi B and Porcelli F. *Phys. Rev. Lett.*, 57:2272, 1985.

[53] Mc Guire K et al. *Phys. Rev. Lett.*, 50:891, 1983.

[54] Brix M et al. *Rev. Sci. Instrum.*, 79:10F325, 2008.

[55] De Angelis R et al. In *36th EPS Conf. on Plasma Physics, Sofia*, 2009.

[56] Hutchinson I H. *Principles of Plasma Diagnostics.* Cambridge University press, 1987.

[57] Welch P. *IEEE transaction*, 15:70, 1967.

[58] Fitzpatrick R. *Nucl. Fusion*, 33:10, 1993.

[59] Barrera L et al. *Plasma Phys. contr. Fusion*, 52:085010, 2010.

[60] Lazzaro E and Zanca P. *Phys. Plasmas*, 10:2399, 2003.

[61] Mailloux J et al. In *36th EPS Conf. on Plasma Physics, Sofia*, page P5.164, 2009.

[62] Fitzpatrick R. *Phys. Plasmas*, 2:3, 1995.

[63] Buratti P et al. In *35th EPS Conf. on Plasma Physics, Hersonissos*, page P1.069, 2008.

[64] Hugon H et al. *Nucl. Fusion*, 32:33, 1992.

[65] Smeulders P et al. *Plasma Phys. contr. Fusion*, 41:1303, 1999.

[66] Nave M F F et al. *Rev. Sci. Instrum.*, 75:4274, 2004.

[67] Maget P et al. *Nucl. Fusion*, 50:045004, 2010.

[68] Buratti P et al. In *36th EPS Conf. on Plasma Physics, Sofia*, page P5.169, 2009.

[69] Challis C D et al. In *36th EPS Conf. on Plasma Physics, Sofia*, page P5.172, 2009.

[70] Buratti P et al. In *Proceedings of 23rd IAEA FEC*, pages EXS/P5–02, 2010.

[71] Hobirk J et al. In *36th EPS Conf. on Plasma Physics, Sofia*, page O5.057, 2009.

[72] Chang Z et al. *Nucl. Fusion*, 30:219, 1990.

[73] Matsunaga G et al. *Phys. Rev. Lett.*, 103:045001, 2009.

[74] Okabayashi M et al. *Nucl. Fusion*, 49:125003, 2009.

[75] Huysmans G et al. *Nucl. Fusion*, 39:1489, 1999.

[76] P. Sonato et al. *Fusion Eng. Design*, 66-68:161–168, 2003.

[77] Marchiori G et al. *Fusion Eng. Des.*, 66:691, 2003.

[78] M. Cavinato et al. *IEEE Trans. Nuclear Sci.*, 53:1015–1021, 2006.

[79] O. Barana et al. *Fusion Eng. Design*, 71:35–40, 2004.

[80] Piron L et al. *Submitted to Nucl. Fusion*, 2011.

[81] Ortolani S. and Schnack D.D. *Magnetohydrodinamics of plasma relaxation.* World Scientific, Singapore, 1993.

[82] R. Paccagnella. *Nucl. Fusion*, 38:1067, 1998.

[83] L.S. Solovev A.I. Morozov. volume 2. Consultans Bureau Press, New York, 1966.

[84] Liu Y Q. *Phys. Plasmas*, 7:3681, 2000.

[85] Portone A et al. *Plasma Phys. contr. Fusion*, 50:085004, 2008.

[86] Rubinacci G et al. *IEEE Trans. Mag.*, 38:582, 2002.

[87] A. Soppelsa et al. *Fusion Eng. Design*, 84:1784–1788, 2009.

[88] Zanca P et al. *Nucl. Fusion*, 47:1425, 2007.

[89] Marchiori G et al. In *36th EPS Conf. on Plasma Physics, Sofia*, page P2.183, 2009.

[90] Liu Y. Q. *Plasma Phys. contr. Fusion*, 52:104002, 2010.

[91] Bolzonella T et al. *Fusion Eng. Des.*, 82:1064, 2007.

Acknowledgments

It is hard to describe how, at this point of a thesis, after having written hundreds of pages without (almost) any problem, words become evanescent and a white page stretches in front of you. It is hard to sum up in few lines all of the people who constituted the living environment where my life took place during the last three years, but anyway let's try it.
First of all I would like to thank Tommaso Bolzonella for being my guide, helping me to develop as a scientist, and being a good example to grow as a person. His trust and encouragement continuously pushed me towards new things to learn and new goals, and helped me in bringing myself into play.
I will be eternally grateful to everybody who helped me building up my skills, educated me and worked with me; among all Barry Alper, Paolo Buratti, Clive Challis, Elena de la Luna, Peter de Vries, Paolo Innocente, Emmanuel Joffrin, Rudi Koslowski, Peter De Vries, Marco Valisa, Roberto Paccagnella, Mireille Schneider, Frederic Imbeaux and Gerardo Giruzzi.
Special thanks go to everybody who red this thesis and helped me debugging it: Barry Alper, Tommaso Bolzonella, Paolo Buratti, Leonardo Giudicotti, Marco Veranda and Roberto Paccagnella. My gratitude comes to Adriano Altichieri and Alessandro Scaggion as well, who helped me out of a pain of 150 latex errors.
I would like to thank my office mates Alessandro, Emanuele, Michela, Silvia ,Junior, Claudio, Zhirui, Barbara, Stefano for supporting me and bearing me, especially during this period of hard nervous work.
A big thank to all of my friends, who did not forget me even though I have been always in my office for the last two months: don't worry, I will be back soon. I am not going to list all of you, because I would end in forgetting some of you, but you were all important!
I also would like to thank my Dad Arrigo, my Mum Annamaria, my sister Michela and all of my family for the trust and encouragement in the challenges I had to face during these three years, and since I was born.
I would like to dedicate these thesis to Lidia, my partner who supports me and takes care of me: during the long time I have spent abroad and alone You made me feel fine just thinking of You, You are my home.

Padova, January 31st 2010 *Matteo Baruzzo*